



**UNIVERSITÄT ZU LÜBECK**  
GRADUATE SCHOOL FOR COMPUTING  
IN MEDICINE AND LIFE SCIENCES

**MINIMALLY INVASIVE NAVIGATED LIVER**

**INTERVENTION**

**Ultrasound-Guided Surgery and Ablation Validation**

Osama Shahin

Dissertation

University of Lübeck

Institute for Robotics and Cognitive Systems

Graduate School for Computing in Medicine and Life Sciences



Aus dem Institut für Robotik und Kognitive Systeme  
der Universität zu Lübeck

Direktor:  
Prof. Dr.-Ing. Achim Schweikard

**MINIMALLY INVASIVE NAVIGATED LIVER  
INTERVENTION**

**Ultrasound-Guided Surgery and Ablation Validation**

Inauguraldissertation  
zur  
Erlangung der Doktorwürde  
der Universität zu Lübeck

Aus der Sektion Informatik/Technik

vorgelegt von  
Osama Shahin  
aus Kairo, Ägypten

Lübeck  
September, 2013

1. Berichtstatter: Prof. Dr.-Ing. Alexander Schlaefer

2. Berichtstatter: Prof. Dr.-Ing. Erhardt Barth

Tag der mündlichen Prüfung: 31.03.2014

Zum Druck genehmigt. Lübeck, den 01.04.2014

# Abstract

Navigated surgery is becoming widely used in applications such as neurosurgery and orthopedics, however it is still in the research phase for soft organs such as the liver. This is mainly because of the organ's deformability which leads to substantial intraoperative anatomical changes. Particularly in minimally invasive interventions, where the surgeon has no direct access to the organ, image guided navigation can play a crucial role to guide the surgical instrument to the target tumor. In case of radiofrequency ablation, accurately targeting the tumor is not enough: the lack of quantitative feedback during the procedure is another problem which may lead to inefficient treatment.

To maintain high navigation accuracy during minimally invasive liver interventions, we propose two new approaches based on tracked 2D ultrasound and focused on the tumor region. The aim is to compensate for intraoperative tumor shift, which can happen due to surgical manipulation or repositioning of the patient. The developed techniques combine segmentation and registration algorithms to estimate the actual tumor position during the surgical procedure. We tested the approaches in a needle navigation experiment on ex-vivo porcine liver. The results indicate that the methods can quickly and accurately compensate for changes in the tumor position, providing a mean needle insertion error of  $1.4 \pm 0.8$  mm using the first approach and  $2.1 \pm 0.8$  mm using the second. The developed techniques have the advantages of being radiation-free, based on the widely available 2D ultrasound, and repeatable throughout the surgery. So they present a practical solution to maintain high tumor targeting accuracy in navigated laparoscopic and radiofrequency ablation procedures.

The second point we investigated is the ablation feedback. To enable quantitative assessment of ablated lesions based on monitoring images, we developed techniques to correlate ablation outcomes on different images (MRI and ultrasound) to actual necroses. Two approaches were developed: one is based on a geometrical phantom and was applied ex-vivo, the other is based on electromagnetic tracking and was tested in-vivo. Results of the experiments showed that the feedback given to the surgeon, upon which the extent of the ablation is determined, varies depending on the imaging modality. This emphasizes the importance of such validation schemes and the need to apply them systematically to obtain a larger dataset. The ultimate goal is to standardize the ablation monitoring procedure and eventually improve the radiofrequency ablation recurrence rate.



# Acknowledgments

This work was conducted at the Institute for Robotics and Cognitive Systems, University of Lübeck, and at the Medical Ultrasound Imaging and Intervention Collaboration (MUSiiC) research lab, Johns Hopkins University. I'm grateful to many people who supported me to accomplish this work. First, I would like to thank Prof. Alexander Schlaefter and Prof. Achim Schweikard for giving me the opportunity to do research in the interesting field of computer-aided surgery. Also my special thanks are extended to Prof. Emad Boctor for having me as a member of his research team for six months. My grateful thanks are also to Dr. Markus Kleemann, who gave me the chance to attend several liver operations and learn about the surgical workflow. I am particularly grateful to Volker Martens and Armin Beširević for introducing me to the research project. Last but not least, I would like to thank Georgios Karagkounis and Daniel Carnegie, with whom I enjoyed working.

# Dedication

*To my parents and my wife.*

# Contents

<b>Abstract</b>	<b>iii</b>
<b>Acknowledgments</b>	<b>v</b>
<b>List of Tables</b>	<b>xiv</b>
<b>List of Figures</b>	<b>xv</b>
<b>Abbreviations</b>	<b>xix</b>
<b>1 Introduction</b>	<b>1</b>
1.1 Motivation . . . . .	1
1.2 Liver Anatomy . . . . .	2
1.3 Liver Functions . . . . .	4
1.4 Cancer and Liver Metastases . . . . .	4
1.4.1 Cancer Spread . . . . .	5

1.5	Liver Cancer Treatment . . . . .	5
1.5.1	Surgery . . . . .	6
1.5.2	Ablation . . . . .	6
1.5.3	Embolization . . . . .	6
1.5.4	Radiation Therapy . . . . .	7
1.5.5	Chemotherapy . . . . .	7
1.6	Minimally Invasive Intervention . . . . .	8
1.6.1	Laparoscopic Surgery . . . . .	8
	Advantages . . . . .	9
	Limitations . . . . .	10
1.6.2	Radiofrequency Ablation . . . . .	10
1.7	Thesis Outline . . . . .	11
<b>2</b>	<b>Image Guided Interventions</b>	<b>15</b>
2.1	Introduction . . . . .	15
2.2	Tracking Systems . . . . .	16
2.2.1	Optical Tracking Systems . . . . .	17
2.2.2	Electromagnetic Tracking Systems . . . . .	17
2.2.3	Instruments Calibration . . . . .	19
2.3	Intraoperative Imaging . . . . .	19
2.3.1	Computed Tomography . . . . .	19
2.3.2	Magnetic Resonance Imaging . . . . .	21

	ix
2.3.3	Ultrasound . . . . . 22
2.4	Visualization . . . . . 25
2.5	Registration . . . . . 25
2.5.1	Feature-Based Registration . . . . . 26
2.5.2	Image-Based Registration . . . . . 27
2.6	Image Guided Liver Interventions . . . . . 28
2.6.1	Open Surgery . . . . . 29
2.6.2	Minimally Invasive Interventions . . . . . 30
2.7	Objective . . . . . 33
<b>I</b>	<b>Ultrasound-Guided Navigation 35</b>
<b>3</b>	<b>3D Freehand Ultrasound 37</b>
3.1	Introduction . . . . . 37
3.2	Ultrasound Calibration . . . . . 37
3.2.1	Spatial Calibration . . . . . 38
3.2.2	Temporal Calibration . . . . . 40
3.3	Volume Reconstruction . . . . . 41
3.4	Conclusion . . . . . 44
<b>4</b>	<b>Tumor Segmentation 45</b>
4.1	Introduction . . . . . 45

4.2	Level Set Segmentation . . . . .	45
4.2.1	Mathematical Background . . . . .	46
4.2.2	Segmentation using Level Set . . . . .	49
	Surface Curvature (3D) . . . . .	50
	Final Evolution Model . . . . .	51
4.2.3	Segmentation Steps . . . . .	53
4.3	Graph Cut Segmentation . . . . .	58
4.3.1	Segmentation Cost Function . . . . .	59
4.3.2	Segmentation Steps . . . . .	62
4.4	Segmentation Cases . . . . .	64
4.5	Conclusion . . . . .	64
<b>5</b>	<b>Local Registration</b>	<b>67</b>
5.1	Introduction . . . . .	67
5.2	Methods . . . . .	68
5.2.1	Local Surface Registration . . . . .	70
5.2.2	Tumor-based Registration . . . . .	71
	Mutual Information Metric . . . . .	72
5.3	Experiments and Results . . . . .	72
5.3.1	Pseudo Tumors Preparation . . . . .	73
5.3.2	Experiment 1: Position Monitoring Validation . . . . .	73
5.3.3	Experiment 2: Needle Navigation . . . . .	75

	xi
5.4 Discussion . . . . .	78
5.5 Conclusion . . . . .	80
<b>6 Sparse Segmentation</b>	<b>81</b>
6.1 Introduction . . . . .	81
6.2 Methods . . . . .	81
6.2.1 Frame Selection . . . . .	82
6.2.2 Tumor Detection . . . . .	83
6.2.3 Tumor Segmentation . . . . .	83
6.2.4 Position Estimation . . . . .	84
6.3 Results . . . . .	85
6.4 Discussion . . . . .	87
6.5 Conclusion . . . . .	89
<b>7 Discussion and Outlook</b>	<b>91</b>
7.1 Navigation Accuracy . . . . .	92
7.2 Speed . . . . .	94
7.3 Visualization . . . . .	95
<b>II Ablation Assessment</b>	<b>97</b>
<b>8 Image-Guided Tumor Ablation</b>	<b>99</b>
8.1 Introduction . . . . .	99

8.2	Ablation Monitoring . . . . .	101
8.2.1	Elastography . . . . .	102
8.3	Ablation Correlation . . . . .	104
8.4	Conclusion . . . . .	105
<b>9</b>	<b>Ex-Vivo Ablation Correlation</b>	<b>107</b>
9.1	Introduction . . . . .	107
9.2	Methods . . . . .	108
9.2.1	Phantom Construction . . . . .	108
9.2.2	Phantom Imaging . . . . .	112
9.2.3	Pose Registration . . . . .	112
9.3	Results . . . . .	114
9.4	Discussion . . . . .	116
9.5	Conclusion . . . . .	118
<b>10</b>	<b>In-Vivo Ablation Correlation</b>	<b>119</b>
10.1	Introduction . . . . .	119
10.2	Methods . . . . .	120
10.2.1	Local Rigidity . . . . .	120
10.2.2	US Volume Mapping . . . . .	121
10.2.3	Plane Mapping . . . . .	122
10.2.4	Validation Test . . . . .	124

10.3 Animal Experiment . . . . .	125
10.4 Results . . . . .	126
10.5 Discussion . . . . .	128
10.6 Conclusion . . . . .	129
<b>11 Summary</b>	<b>131</b>
<b>Bibliography</b>	<b>135</b>

# List of Tables

4.1	Weights of all types of edges in the graph. . . . .	61
5.1	Results of the local surface registration using ICP: translation, rotation, time required to update the tumor position, and distance between the transformed tumor position and the actual tumor position. . . . .	77
5.2	Results of the tumor-based registration using MI: translation, time required to update the tumor position, distance the tumor was shifted, and the residual navigation error after updating the tumor position. . . . .	78
5.3	Overall tumor shift recovered by the registration, total time required to update tumor position, error after ICP, and residual navigation error after the tumor-based registration. . . . .	79
6.1	Results of the sparse segmentation algorithm using the <i>graph cut</i> segmentation: average segmentation time per image, registration time using ICP, total time from frame selection till position estimation, and the error calculated as the distance between the estimated tumor centroid and the actual tumor centroid. . . . .	87
6.2	Results of the sparse segmentation algorithm using the <i>level set</i> segmentation: average level set segmentation time per image, registration time using ICP, total time from frame selection till position estimation, and the error calculated as the distance between the estimated tumor centroid and the actual tumor centroid. . . . .	88

# List of Figures

1.1	Illustration of the segmental liver anatomy <sup>1</sup> . . . . .	3
1.2	Laparoscopic vs. open surgery showing how laparoscopic intervention is performed using instruments inserted into the abdomen through small incisions <sup>2</sup> . . . . .	9
1.3	Radiofrequency ablation for the treatment of liver cancer <sup>3</sup> . . . . .	11
2.1	Optical tracking components: infrared camera, active and passive trackers (Polaris, NDI, Ontario, Canada), RMS tracking accuracy for this model is 0.35 mm. . . . .	18
2.2	EM tracking field generator and a 6 DOF sensor (Aurora, NDI, Ontario, Canada), RMS tracking accuracy for this model is 0.70 mm. . . . .	18
2.3	Axial CT image showing a liver with tumors. . . . .	20
2.4	MRI machine (www.healthcare.siemens.com). . . . .	22
2.5	Illustration of the reflection and transmission of ultrasound waves due to acoustic impedance mismatch at the boundary between different regions. . . . .	23
2.6	Configurations of different laparoscopic ultrasound probes (Solberg et al. [1]). . . . .	24
2.7	Liver model generated from preoperative data (Lange et al. [2]). The model shows the resection plan (darker region), tumor (yellow), and vessels to be resected (green). . . . .	26
3.1	Ultrasound plane (dashed line) intersecting an <i>N-fiducial</i> at the points E, K, and Z. . . . .	38

3.2	Calibration of the LUS probe using two EM sensors, one attached to the probe and the other to the calibration phantom. The US image with the six dots shows the intersection of the image plane with the $N$ -fiducials in the phantom. . . . .	40
3.3	Ultrasound calibration using an $N$ -fiducial phantom. . . . .	41
3.4	Interpolation of tracking data to match the corresponding US frames. . . . .	41
3.5	Sketch illustrating the volume reconstruction transformations. . . . .	43
3.6	Reconstructed US volume. . . . .	43
4.1	Curve propagation with speed $F$ in the normal direction. . . . .	46
4.2	Level sets and front motion (a) The curve $\Gamma$ and the surface $\phi(x, y)$ at $t = 0$ . (b) The curve $\Gamma$ and the surface $\phi(x, y)$ at time $t$ . . . . .	48
4.3	Curvature forces act in the direction of the unit normal vector. . . . .	50
4.4	Principal curvature directions. . . . .	51
4.5	Image of a disc (boundary) and a through-cut at one point. . . . .	53
4.6	The smoothed 1D image and its $\mathbf{g}_I$ , arrows show $\nabla \mathbf{g}_I$ direction. . . . .	53
4.7	Effect of median filter on an US image of metastatic liver tumor. . . . .	54
4.8	Geometric interpretation of the distance function. (a) 1D distance function. (b) 2D distance function. . . . .	55
4.9	The significance of $\alpha$ & $\beta$ in equation (4.21). The $\alpha$ parameter defines the width of the intensity window. The $\beta$ parameter defines the center of the intensity window <sup>4</sup> . . . . .	55
4.10	Tumor image after applying sigmoid filter, most of the pixel intensities inside the tumor are mapped to a maximum value and most of those outside are mapped to a minimum value. The tumor borders are not completely defined by the sigmoid filter, however edges making parts of the tumor contour contribute significantly to the energy terms. . . . .	57
4.11	Initial contour evolves according to the governing level set function to eventually take the shape of the tumor. . . . .	57
4.12	Illustration of a graph cut on $3 \times 3$ image, thickness of the directed edges represent their weights. Two types of links: n-links between the neighboring pixels (yellow), t-links between the pixels and the source (red), and t-links between the pixels and the sink (blue). From Boykov et al. [3]. . . . .	59
4.13	Initialization of the graph cut algorithm by selecting two sets of pixels: object (tumor) and background. . . . .	62
4.14	Segmentation result without limiting the segmentation algorithm to the area around the tumor. The segmented image shows that not only the tumor was segmented, but also some other irrelevant parts of the image. . . . .	63

4.15	(a) Segmentation when the area considered in the segmentation was limited to the <i>narrowband</i> around the tumor. (b) Final segmentation after applying erosion and dilation morphological filters. . . . .	64
4.16	Segmentation results of real liver tumors using level set and graph cut algorithms. . . . .	65
5.1	Steps involved in the approach. First step resembles the US calibration procedure (section 3.2), where an US image intersects the wires (white dots) inside the calibration phantom. Second, an US volume is reconstructed. Third, tumor is segmented and its position is determined. Those three steps are performed initially; afterwards, automatic monitoring of the tumor position is performed with each newly acquired US volume using the segmented tumor and its previous position as priori knowledge. . . . .	69
5.2	Illustration of the ICP registration algorithm between two sets of points. For each US frame acquisition, three points on the liver surface are collected. By completing the scan, these points form a set of points. . .	70
5.3	Ultrasound image showing one of the pseudo-tumors embedded in porcine liver tissue. . . . .	73
5.4	(a) Target tumor was moved inside a water tank on a known trajectory using a robot. (b) One of the US images acquired while scanning the target in the water tank. . . . .	74
5.5	Snapshot of the navigation software showing rendered US volume and segmented tumor. It gives the option to show/hide or change the transparencies of the volume/tumor. Also it provides the distances from the needle tip to the tumor centroid and from the needle trajectory (path) to the tumor centroid. . . . .	75
5.6	Photo taken during the experiment: tracked LUS probe scanning piece of porcine liver to acquire an US volume. Meanwhile, tracked needle was navigated towards an embedded pseudo-tumor. . . . .	76
6.1	Tumor contours segmented using <i>graph cut</i> on three of the selected US frames. . . . .	86
6.2	Tumor contours segmented using <i>level set</i> on three of the selected US frames. . . . .	86
6.3	Tumor surface points (green) mapped to the segmented contours (red). . . . .	86
8.1	Radiofrequency tumor ablation causes vaporization in the tissue. . . .	102
8.2	Displacement and strain caused by a constant pressure applied to a tissue with different stiffness layers. . . . .	103
8.3	Displacement and strain images of a phantom containing a sphere made of stiffer material to mimic a tumor (Rivaz et al. [4]). . . . .	104

9.1	3D model of the acrylic glass mold which was used to create a fiducial footprint in the gelatin mixture. . . . .	109
9.2	Dimensions of the acrylic glass model used to create the fiducials in the gelatin phantom. . . . .	109
9.3	From the similar triangles (ABC) and (BCE), the coordinates of the point F can be determined by equation (9.1), given the ratio $EF/EG$ and the exact geometry of the phantom. . . . .	110
9.4	Cross section through the phantom showing the tissue and the fiducials. The segments EG and EF were measured for each fiducial to determine the ratio $EF/EG$ at each phantom side. . . . .	111
9.5	The phantom ready to be scanned with the robotized US probe. . . . .	113
9.6	Gross pathology slices registered to corresponding MRI and US images using the “ <i>Z-Shape</i> ” correlation phantom. . . . .	115
9.7	Mean error on the MRI slice calculated by measuring the fiducial lengths on the images and comparing them to the actual lengths on the gross pathology. . . . .	116
9.8	Gross pathology slices and the corresponding strain images. . . . .	117
10.1	EM sensor glued to a biopsy needle with a hooked end. First the needle was used to insert the EM sensor into the tissue, and then the anchor was deployed to keep the sensor in place. . . . .	121
10.2	Sketch of the approach setup while using US to image the ablation: step 1 symbolizes a liver section having a lesion inside and a 6D EM sensor (S) anchored next to the lesion; step 2 is after cutting through the lesion, where a tracked pointer was used to collect points on the cutting surface. Transformations between frames were either obtained directly from the tracking systems or via calibration. . . . .	123
10.3	Drawing illustrates one side of the phantom: the transparent gelatin was removed after the US acquisition, then points were collected on the speckle layer. . . . .	124
10.4	Tracked pointer while registering the MRI fiducials during the animal experiment. Overlaid picture explains how the anchored sensor was deployed inside the tissue. . . . .	125
10.5	Example of the validation results demonstrates that the <i>speckle layer</i> was mapped correctly to the US volume; i.e. the end-to-end plane mapping error was within 2 mm. . . . .	126
10.6	Cross section in the MRI volume showing three of the lesions and one of the mapped planes intersecting the corresponding lesion. . . . .	127
10.7	Set of results (MRI, US, gross and histopathology slices) shows the ablated lesion and allows for multimodal ablation correlation. . . . .	128
10.8	Chart plotting areas of the lesions measured on correlated histopathology (ground truth), gross pathology, MRI, and US images. . . . .	128

## Abbreviations

<i>HCC</i>	Hepatocellular Carcinoma
<i>CCD</i>	Charged-Coupled Device
<i>CT</i>	Computed Tomography
<i>DNA</i>	Deoxyribonucleic Acid
<i>DOF</i>	Degrees of Freedom
<i>EM</i>	Electromagnetic
<i>ENT</i>	Ear, Nose, and Throat
<i>FLR</i>	Future Liver Remnant
<i>GP</i>	Gross Pathology
<i>HIFU</i>	High-Intensity Focused Ultrasound
<i>HP</i>	Histopathology
<i>ICP</i>	Iterative Closest Point
<i>IGI</i>	Image Guided Intervention
<i>IR</i>	Infrared
<i>LED</i>	Light Emitting Diode
<i>LITT</i>	Laser-Induced Interstitial Thermotherapy
<i>LUS</i>	Laparoscopic Ultrasound
<i>MI</i>	Mutual Information
<i>MRI</i>	Magnetic Resonance Imaging
<i>MSD</i>	Mean Square Distance

<i>NCC</i>	Normalized Cross Correlation
<i>PDE</i>	Partial Differential Equation
<i>RFA</i>	Radio-Frequency Ablation
<i>RF</i>	Radio Frequency
<i>RMS</i>	Root Mean Square
<i>ROI</i>	Region of Interest
<i>SDK</i>	Software Development Kit
<i>SD</i>	Standard Deviation
<i>TGC</i>	Time Gain Compensation
<i>TPS</i>	Thin Plate Spline
<i>TRE</i>	Target Registration Error
<i>US</i>	Ultrasound

# Chapter 1

## Introduction

### 1.1 Motivation

Cancer is a leading cause of death worldwide, causing 7.6 million deaths (around 13% of all deaths) in 2008 [5]. The liver is highly susceptible to both primary and metastatic cancer [6]. Usually, surgical intervention is necessary to remove or ablate the tumor [7]. Minimally invasive interventions, when applicable, are advantageous for the patient over the conventional open surgery. However, it presents a challenge for the surgeon to accurately control surgical instruments without having direct access to the organ. Therefore, image guided navigation is required to provide the surgeon with additional information during the surgery, by tracking the instruments and imaging the internal anatomy.

Liver interventions require deep understanding of the complex anatomy of the organ and its vascular structures. The introduction of surgical planning based on 3D imaging data from computed tomography (CT) or magnetic resonance imaging (MRI) enables preoperative anatomy visualization, quantitative assessment of risk factors, and determination of surgical strategies. However, accurate realization of the surgical plan is not a trivial task in a highly deformable organ such as the liver. In minimally

invasive liver interventions, the tumor can be subject to considerable shift caused by pneumoperitoneum [8], respiration [9], heartbeat [10], patient movement, and liver manipulation by surgical instruments. While periodic motions can be modeled and recovered [11, 12], irregular motions need to be quickly reflected in the navigation system to maintain an accurate navigation throughout the surgical procedure.

When developing a navigation system for deformable organs, there is always a trade-off. Mapping every deformation to the navigation screen requires complicated and time-consuming algorithms, which is typically impractical for the surgical workflow. On the other hand, assuming rigidity of the organ may lead to inaccurate navigation at the region of interest containing the target tumor. The compromise we chose while developing our methods is based on the fact that the surgical workflow is local by default; the surgeon focuses on only one tumor at a time. Hence, we focused on the key information in the navigation procedure, the target tumor, and assumed rigidity in the local neighborhood.

Tumor treatment using radiofrequency ablation (RFA) is a common minimally invasive procedure [13]. While a navigation system can assist the surgeon targeting the tumor, feedback during the procedure is equally important for a successful treatment. Quantitative evaluation of the feedback given by imaging modalities used in ablation monitoring such as ultrasound (US) is still missing [14]. This was our motivation to develop methods to correlate ablated lesions on intraoperative images to actual necroses.

## 1.2 Liver Anatomy

The liver is the largest internal organ in the body. It lies just below the diaphragm beneath the right lung and weighs approximately 2% to 3% of the total body weight of an adult. It has a triangular shape and divided into two main lobes (right and left), these lobes are further divided into segments [15]. Figure 1.1 shows the segmental hepatic anatomy and main vessels.

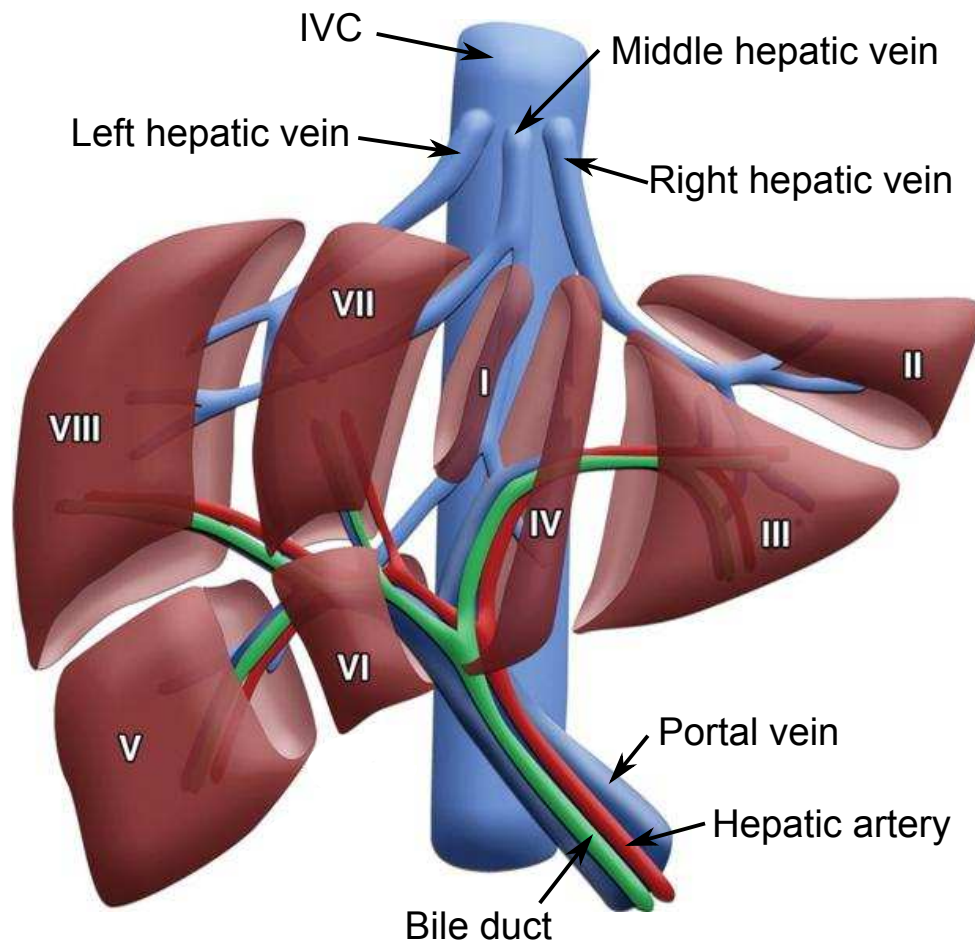


Figure 1.1: Illustration of the segmental liver anatomy<sup>1</sup>.

Two sources supply the liver with blood: blood rich in oxygen from the heart through the hepatic artery, and nutrient-rich blood from the intestines through the portal vein. The parenchyma of the liver is made up of cells called hepatocytes, other cell types also exist such as cells lining the blood vessels and bile ducts. The liver regulates most chemical levels in the blood and excretes a product called bile into the hepatic duct, this duct transports the bile to the gallbladder and intestines. All the blood leaving the stomach and intestines passes through the liver. The liver processes this blood and breaks down the nutrients and drugs into forms that are easier to use for the rest of the body.

<sup>1</sup>Source: Singh et al. [16]

### 1.3 Liver Functions

Several essential functions are carried out by the liver, including the following:

- It regulates chemical levels in the blood and filters out toxic wastes.
- It breaks down (metabolizes) and stores many of the nutrients absorbed from the intestine to be used by the rest of the body for energy or to build and repair body tissues.
- It produces most of the clotting factors that prevent too much bleeding in case of injury.
- It secretes bile into the intestines, which helps break down fats in the small intestine and carry away waste during digestion.
- It converts excess glucose into glycogen for storage, which can later be converted back to glucose for energy.

### 1.4 Cancer and Liver Metastases

Cancer is an abnormal cell growth out of control. There are more than one hundred diseases in which cells in a certain body organ may grow out of control. Untreated cancer can cause serious illness and may lead to death. Growth, division, and death is a normal body cells life cycle. Normal body cells divide more quickly during the early years of a person's life. When the person becomes an adult, cells in most parts of the body divide only to replace exhausted or dying cells and to repair injuries. In contrary to normal cells, cancer cells continue to grow and form abnormal cells. DNA (Deoxyribonucleic Acid) exists in every cell and has the role of directing its activities. Cancer cells are developed because of damage to DNA. Normally, either the cell dies or repairs the DNA. In cancer cells, the damaged DNA stays not repaired and the cell doesn't die. Moreover, this cell goes out of control, making new cells with the same damaged DNA. Damaged DNA can be inherited, but mostly it is caused by other reasons such as chemicals, viruses, too much sun light or tobacco smoke [17].

### 1.4.1 Cancer Spread

Cancer cells often travel through the bloodstream or through the lymph system to other parts of the body, where they begin to grow and form new tumors that replace normal tissue. This spreading process is called metastasis. No matter where a cancer may spread, the metastasis is named for the place of the body where it is originated. For example, breast cancer may spread into the liver and cause breast cancer metastases. Most of the cancer found in the liver is not originated there, but it is metastasized from somewhere else in the body [15].

Several types of cancer can start in the liver including hepatocellular carcinoma (HCC), intrahepatic cholangiocarcinoma (bile duct cancer), and cancers that begin in cells lining the blood vessels of the liver. More than 700,000 people are diagnosed with liver cancer each year throughout the world [18]. It is also a leading cause of cancer mortality worldwide.

## 1.5 Liver Cancer Treatment

After liver cancer is diagnosed, the stage of the cancer describes the extent or severity of the case. According to the stage of disease and the overall health of the liver, the doctor plans an appropriate treatment. Depending on many factors such as the extent of the case and the overall health of the patient, the treatment may include one or more of the following:

- Surgery
- Ablation or embolization
- Radiation therapy
- Targeted therapy
- Chemotherapy

### 1.5.1 Surgery

The aim of liver surgery is to completely remove the tumor and render the patient free of metastatic diseases. The first open liver resection was reported by Ichio Honjo in 1949, Kyoto University. The description of the segmental liver anatomy by Couinaud in 1957 marked a breakthrough in liver surgery. After that more centers started performing these complex operations [19]. With the advance of the surgical techniques, resectability of tumors is not any more limited to the size, number, or location. Metastases are resectable as long as an adequate functional future liver remnant (FLR) remains. Moreover, downsizing of lesions which were considered unresectable due to size or location is now possible via chemotherapy [20].

### 1.5.2 Ablation

Ablation techniques treat tumors by destroying the cancer cells without removing them. It is often used to treat patients with no more than a few small tumors or when surgery is not a good option because of poor patient's health or reduced liver function [15]. Several techniques are used to destroy tumors in ablation procedures, such as thermal ablation, ultrasound ablation, and cryotherapy. Thermal ablation methods, including radiofrequency, microwave, and laser approaches, generate heat which turns cancer tissue into dead tissue. Also high frequency focused ultrasound (HIFU) is used to apply high intensity focused ultrasound energy to locally heat and destroy the tumor [21]. On the contrary, cryotherapy techniques destroy the tumor by freezing it.

### 1.5.3 Embolization

Embolization is the injection of substances (emboli) into a blood vessel to stop or occlude the blood flow to cancer cells in the liver. It is a nonsurgical minimally invasive procedure which can be an option for patients with tumors that cannot

be removed surgically. Also it can be used to kill off tumors that are too large to be treated with ablation. This technique exploits that the liver has two blood supplies [15]. For example, blocking a branch of the hepatic artery feeding a tumor helps to treat the tumor, while other healthy liver cells stay unharmed because their blood supply comes from the portal vein.

### **1.5.4 Radiation Therapy**

Radiotherapy uses high-energy ionizing radiation to kill cancer cells by damaging their DNA. Cancer cells are more sensitive to ionizing radiation than normal cells. It is not often used to treat liver cancer as radiation can damage healthy parts of the liver. Radiotherapy may be used to treat bile duct cancer, but is less likely used for hepatocellular liver cancers [7].

### **1.5.5 Chemotherapy**

Chemotherapy is cancer treatment with anti-cancer drugs, these drugs are injected into a vein or given by mouth. These drugs circulate in the bloodstream and reach all areas of the body. Thus, chemotherapy can kill cancer cells that have metastasized or spread to parts of the body far from the original tumor. It kills the cell by damaging the part inside the cell responsible for the cell division process. This explains why it also affects healthy tissue where the cells are rapidly growing and splitting such as hair follicles, bone marrow, and lining of the digestive system. Liver cancer resists most chemotherapy drugs [15], but it can help in combination with other types of treatment. For example, it can be used before surgery to down size the tumor or after surgery to help lower the risk of the cancer coming back.

## 1.6 Minimally Invasive Intervention

Currently, surgery is the only option which gives reasonable chance to cure liver cancer [7]. When applicable, a minimally invasive intervention provides a less invasive alternative to the open surgery. Typically, it is carried out through the skin or anatomical opening or a body cavity, and involves observation of the surgical field on a screen using an endoscope. Many medical procedures are called minimally invasive, such as percutaneous surgery, endoscopy, ablation procedures, stereotactic surgery, laparoscopic surgery, and others. We focus in this work on two important minimally invasive techniques for liver interventions, namely *laparoscopic surgery* and *radiofrequency ablation*.

### 1.6.1 Laparoscopic Surgery

Although minimally invasive surgery has significant benefits for the patient, the adaption of laparoscopic liver surgery progressed slowly mainly because of the complexity of the liver operations. The first laparoscopic liver resection was reported by Gagner et al in 1992. Since then, over 3000 liver resections have been performed mainly in specialized liver centers [22]. The surgeon uses long thin instruments through small incisions to perform the operation. Figure 1.2 illustrates the concept of laparoscopic liver surgery in comparison to the open approach.

Laparoscopic liver resection requires expertise in both advanced laparoscopic techniques and precise knowledge of liver anatomy [23]. It was initially performed for low-risk cases like the resection of benign lesions. Recently, laparoscopic techniques have gradually become incorporated in the practice of most of the liver centers. The most common indications of laparoscopic liver resections are for peripheral tumors, 5 cm or less [19]. Although most types of liver resection can be performed laparoscopically, including major liver resections (i.e. right or left hepatectomies), these should be reserved to experienced surgeons [24]. Due to the recent technological advance

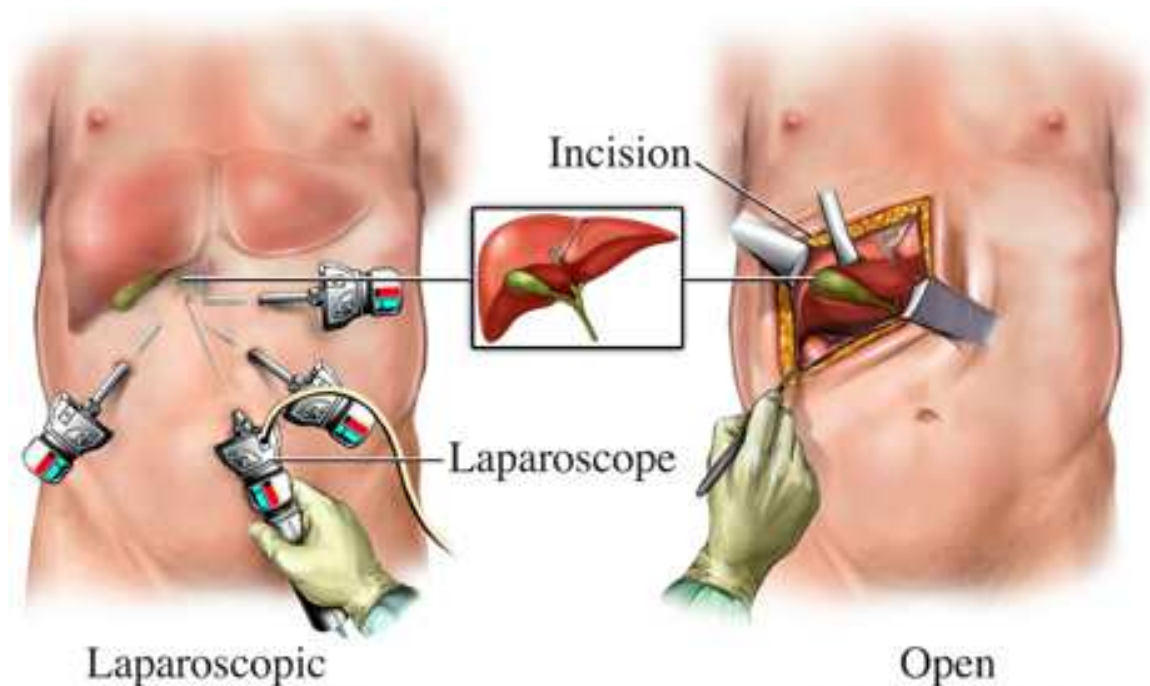


Figure 1.2: Laparoscopic vs. open surgery showing how laparoscopic intervention is performed using instruments inserted into the abdomen through small incisions<sup>2</sup>.

in laparoscopic surgery, laparoscopic hepatic resection became more common and surgeons are gaining more experience and expanding its indications.

### Advantages

Laparoscopic liver resection has significant benefits for patients, such as decreased operative time, less blood loss, less analgesic requirements, faster recovery, shorter hospital stay, and better cosmetic outcome. Besides, there are no economical disadvantages regarding the laparoscopic approach [25]. Furthermore, the oncological outcomes of the laparoscopic resection show no difference in comparison to the open approach [23, 26]. Also, in a study conducted by Rao et al. [19], it is reported that laparoscopic liver resection showed a reduced overall morbidity rate when compared with the open group.

---

<sup>2</sup>Source: <http://www.toolabi.com/en/service/biliary-surgery>

### **Limitations**

While laparoscopic surgery is clearly advantageous for patients, surgeons must use tools to interact with the tissue rather than manipulate it directly with their hands in open surgery. Hence, the procedure brings several challenges for the surgeon such as indirect vision through an endoscopic camera, limited freedom in manipulating the instruments, reduced haptics, and poor depth perception [27]. Also the instruments endpoints move in the opposite direction relative to the surgeon's hands due to the pivot point, making laparoscopic surgery a non-intuitive motor skill that is difficult to learn. All these factors increase the risk, for example hemorrhage is more difficult to control laparoscopically.

Systematic training for laparoscopic liver surgery is necessary. A non-experienced surgeon cannot perform laparoscopic surgeries. Approximately 60 operations have to be performed in order to overcome the learning curve effect. Not only the number of operations but the regular practice and standardization of the laparoscopic procedures are key factors in proper development of laparoscopic liver surgery program [28]. Surgeons performing laparoscopic liver surgery require expertise in two areas: advanced laparoscopic technical skills and precise knowledge of liver anatomy and liver surgery [23].

### **1.6.2 Radiofrequency Ablation**

For nonresectable liver tumors, RFA is the most viable minimally invasive therapeutic procedure [13]. In 1943, King et al. reported the occurrence of liver tissue damage with whole body hyperthermia, however, the technology was adapted in 1990 to allow minimally invasive treatment of malignant hepatic tumors [29,30]. The procedure uses high frequency alternating current to destroy tumors and surrounding tissue. The frequency range for RFA is about 200 KHz - 20 MHz, this high frequency alternating current doesn't cause muscle stimulation or life-threatening arrhythmias [7].

A needle-like probe, usually with deployable tines at the tip, is used by the surgeon to target the tumor under realtime image guidance, Figure 1.3. Heat generated by the alternating current turns the cancer tissue into dead tissue. RFA may be performed either percutaneously or during laparoscopic surgery. Intraoperative imaging, such as US and CT, is used to guide the ablation probe and monitor the procedure. The treated tissue undergoes coagulative necrosis, which is gradually replaced by fibrosis and scar tissue.

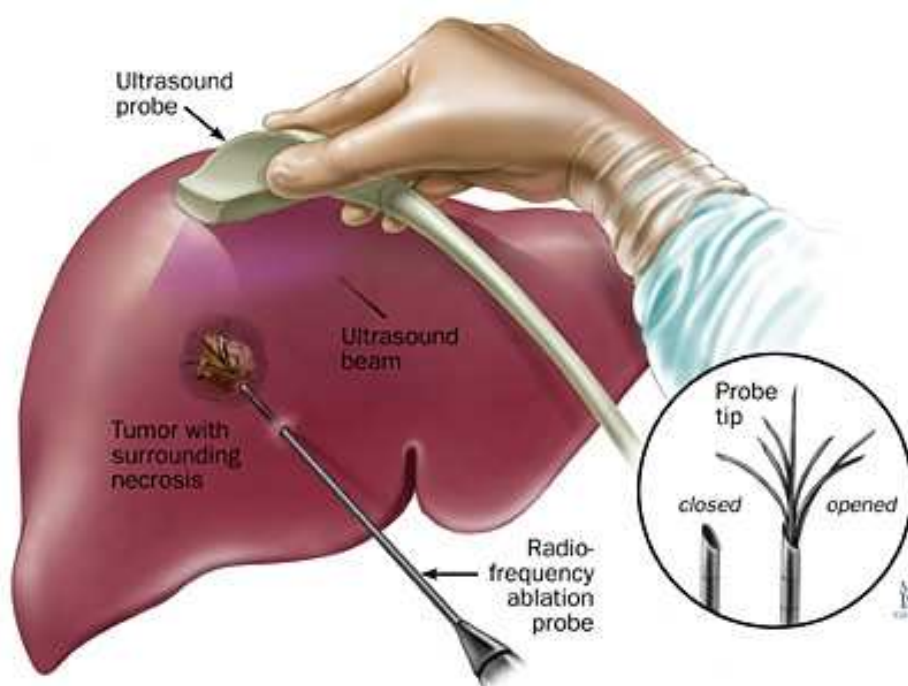


Figure 1.3: Radiofrequency ablation for the treatment of liver cancer<sup>3</sup>.

## 1.7 Thesis Outline

Minimally invasive intervention has many advantages, especially for the patient. However, it can hinder surgeon's capabilities during the surgery. Therefore, additional information obtained via imaging and navigation techniques can be of a great help

<sup>3</sup>Source: [http://www.hopkinsmedicine.org/liver\\_tumor\\_center/treatments/ablative\\_techniques](http://www.hopkinsmedicine.org/liver_tumor_center/treatments/ablative_techniques)

to the surgeon. Image guided interventions have proven its feasibility and become routinely performed on rigid anatomy, such as orthopedics, and ear, nose, and throat (ENT) surgery. However, navigation in soft tissue interventions requires more sophisticated techniques to deal with tissue deformation, organ shift, and tracking of flexible tools.

Recent preliminary practice of image guided liver intervention raised two major technical challenges. First, how to compensate for intraoperative organ changes and make the navigation system reflect the actual target position during the surgery. Second, several imaging techniques are used to monitor RFA procedures, but there is no standard way to evaluate the ablation outcome based on the feedback given to the surgeon. These are the two problems addressed in this work.

The thesis is structured as follows:

### **Chapter 2: Image Guided Interventions**

This chapter gives an overview of different components used in image guided surgical techniques. Then we present the state of the art in open and minimally invasive navigated liver interventions.

### **Part I: Ultrasound-Guided Navigation**

#### **Chapter 3: Three-Dimensional Freehand Ultrasound**

As our navigation approach is based on freehand 3D ultrasound, we demonstrate in this chapter how to reconstruct a 3D ultrasound volume from tracked 2D laparoscopic frames.

#### **Chapter 4: Tumor Segmentation**

This chapter covers two different methods to segment tumors on ultrasound images: level set and graph cut segmentation algorithms. The theory and how the algorithms were adapted to solve the segmentation problem are explained.

**Chapter 5: Local Registration**

Here we present our first approach to maintain high navigation accuracy to the target tumor throughout the surgical procedure. The tumor is segmented once, then fast registration is applied repeatedly to localize the tumor in 3D reconstructed ultrasound volumes.

**Chapter 6: Sparse Segmentation**

In this chapter, we present our second approach to automatically detect and localize tumors during the surgery. This technique is mainly based on image segmentation and uses a few automatically selected ultrasound images to quickly estimate the current tumor position.

**Chapter 7: Discussion and Outlook**

Here we discuss the proposed techniques in the context of the state of the art in related work with respect to three important aspects in navigated liver procedures: accuracy, speed, and visualization.

**Part II: Ablation Assessment****Chapter 8: Image-Guided Tumor Ablation**

This chapter introduces current ablation monitoring techniques which are used to give feedback to the surgeon during ablation procedures.

**Chapter 9: Ex-Vivo Ablation Correlation**

Here we present our phantom-based platform to enable systematic correlation of ablation images obtained from different monitoring modalities and compare them to gross-pathology images.

**Chapter 10: In-Vivo Ablation Correlation**

In this chapter we propose an in-vivo ablation correlation technique based on electromagnetic tracking and present an animal experiment.



# Chapter 2

## Image Guided Interventions

### 2.1 Introduction

The future of minimally invasive interventions relies heavily on the availability and accuracy of image guided techniques. Generally, an image guided intervention IGI involves the following steps:

- Plan the surgery based on preoperative data, typically tomographic images
- Localize and track the position of the surgical instrument or therapeutic device
- Register preoperative data to the actual situation of the organ of interest
- Visualize the position of the tracked instrument relative to the registered image
- Update the guiding images throughout the operation based on the intraoperative situation

Although modern image guided interventions have been correlated with the recent advance in imaging and tracking techniques, the IGI concept has been around for over a hundred years. First stereotactic neurosurgical device was developed by Horsley and Clark in 1908. Almost 40 years later, first human stereotactic frame was designed by Spiegel and Wycis in 1947. Stereotaxis concept is based on fixing a three-dimensional

Cartesian coordinate system (stereotactic frame) to the skull before image acquisition, thus allowing for establishment of a spatial relationship between the medical image space and the stereotactic frame space. As the position of the subcortical anatomy relative to the stereotactic frame remains approximately constant, the target in the brain can be located in terms of the frame-based coordinate system, and tools can be guided to deep brain structures.

The invention of CT in 1973 by Hounsfield enabled three-dimensional imaging of internal structure. This allowed for three-dimensional stereotactic localization in 1979 [31]. Also the advance in computer systems and the release of personal computers in 1980s significantly changed the field of image guided procedures. In the early nineties, optical and electromagnetic (EM) tracking systems became commercially available. These systems enable continuous tracking of surgical instruments using small sensors attached to them. By using such a system, a mechanical connection between the surgical instrument and the patient's anatomy is no longer required.

## 2.2 Tracking Systems

Tracking devices are used to localize surgical tools relative to the patient anatomy. A tracking device is an essential component of any image-guided surgical system. First versions of tracking devices were actually robotized mechanical digitizers, which allowed for frameless stereotaxy in the 1980s. Optical tracking systems were then developed and proved to be the most accurate tracking solution [32]. However, the use of an optical tracking system requires uninterrupted line-of-sight between the optical markers and the tracker camera. EM tracking system is an alternative that avoid line-of-sight limitations and enable tracking of flexible instruments inside the body. The choice of the tracking system depends on the application and the desired accuracy.

### 2.2.1 Optical Tracking Systems

There are optical tracking based on pattern recognition in video image sequences, laser sensation, and infrared (IR) detection. The latter is widely used in clinical applications. In the IR-based tracking systems, wavelengths of ambient light are eliminated by an optical band-pass filter, hence the system can reliably identify optical markers emitting or reflecting IR wavelengths.

- **Active optical trackers:** LEDs emitting waves in the near-IR range are used as markers. The camera module tracking the markers consists of either two planar or three linear charge-coupled device (CCD) units. The LEDs are fired sequentially and signals are captured by each CCD sensor. At least three non-collinear LEDs for each marker are required to determine six degrees-of-freedom (DOF) pose information. Based on the known geometric configuration and firing sequence of each LED and the known distance between the CCD sensors, a triangulation method is used to solve for the pose. Typically active markers are wired to a central unit to get powered.
- **Passive optical trackers:** instead of active LEDs, retroreflective spheres are used as markers. The camera illuminates those spheres in the near-IR spectrum. Each tracking probe (set of reflective markers) must have a unique pattern, so that the reflected IR can be assigned to a particular probe. The system has 2D CCD cameras which identify reflective markers. Similar to the active approach, the six DOF pose is estimated via triangulation. However, no wires are necessary between the central unit and the tracked probes. Figure 2.1 shows an optical tracking camera, an active tracker, and a passive tracker.

### 2.2.2 Electromagnetic Tracking Systems

These systems localize small EM sensors in an EM field of known geometry. The sensors consist of small coils which measure the induced voltage, which is proportional to the flux of the magnetic field. Figure 2.2 shows an EM field generator and a sensor.

## 2.2. TRACKING SYSTEMS

---



Figure 2.1: Optical tracking components: infrared camera, active and passive trackers (Polaris, NDI, Ontario, Canada), RMS tracking accuracy for this model is 0.35 mm.

The main advantage of EM tracking is the lack of the line-of-sight limitation and the ability to track flexible instruments and catheters. On the other hand, the technology is sensitive to distortion from nearby metal objects, also the accuracy is slightly less compared to optical tracking [32]. However, the practical difference between EM tracking and optical tracking systems is less significant, since EM sensors are small in size and can be fixed closer to the point of interest. Thus, the error doesn't extrapolate further to a larger number. Generally, EM tracking systems are used when the objects tracked cannot be seen by the tracking camera (interrupted line-of-sight), e.g. tracking of surgical instruments inside the patient in laparoscopic procedures.



Figure 2.2: EM tracking field generator and a 6 DOF sensor (Aurora, NDI, Ontario, Canada), RMS tracking accuracy for this model is 0.70 mm.

### 2.2.3 Instruments Calibration

By using tracking systems, we can determine the six DOF pose of the sensor/probe attached to the surgical tool, however what matters is the position of the end effector approaching the target, for instance the needle tip in case of an ablation procedure. Therefore, instrument calibration is necessary to determine the position of the instrument tip, given the tracking information obtained via the sensor. Pivot calibration is usually performed to find the relation between the attached sensor and the tip of the instrument [33]. The procedure involves fixing the instrument tip in a divot and rotating the instrument back and forth while collecting tracking data. After collecting enough samples, the transformation from the tracked sensor to the needle tip is calculated using a least square method. Hence, the point at the needle tip is determined in the tracking system space.

## 2.3 Intraoperative Imaging

Especially in minimally invasive procedures, intraoperative imaging is crucial because the anatomical/pathological target cannot be observed directly by the surgeon. Several medical imaging modalities based on different methods are in use currently. Because the physical concept varies from one modality to another, image acquisition workflow and image characteristics are different. Hence, different modalities are used in a complementary fashion and there is no single ideal modality for image guided interventions. The modalities introduced next are the commonly used in liver interventions.

### 2.3.1 Computed Tomography

Computed tomography utilizes X-rays to generate images. X-rays are generated by accelerating electrons and directing them toward a metal target. Once the electrons

### 2.3. INTRAOPERATIVE IMAGING

---

encounter this target, they rapidly decelerate and dissipate their energy as heat and X-rays. When the X-ray photons reach the patient, they interact with the tissue through the photoelectric effect and Compton scattering. The net result of this process is that the detected X-rays are the photons traveled in a straight line from the source to the detector without being absorbed or scattered. Hence, X-ray images are often described as shadowgrams or projection images.

In CT, the X-ray generator and detector are mounted on a gantry that rotates around the patient. As the gantry rotates, projection images of the patient are acquired at fixed angular intervals. Once a sufficient number of samples are obtained, the projection images are then reconstructed into 3D axial slices through the patient. Although the reconstruction process requires a fast or parallel computing, analytical reconstruction using backprojection methods [34,35] can be performed in almost real time. However, the limit of the gantry speed is approximately 0.4 sec per revolution, this corresponds roughly to 2 images per sec.



Figure 2.3: Axial CT image showing a liver with tumors.

Due to the excellent image quality of CT images (Figure 2.3), they are typically used for preoperative imaging and treatment planning. In applications where they can be used for guidance during the intervention, the size and design of the gantry makes it a cumbersome procedure. An alternative is to use an “advance” and “check” approach, where the surgical instrument is moved with the scanner off a small distance, and then the patient is imaged again to determine magnitude and direction of the next move.

### 2.3.2 Magnetic Resonance Imaging

Magnetic resonance imaging is based on the phenomenon that certain atomic nuclei have a resonant frequency when they are placed in a magnetic field. This resonant frequency is proportional to the magnetic field strength. When these nuclei are subjected to radiofrequency waves at the resonant frequency, they absorb this energy and possess a higher energy state. As these excited nuclei return to their original state, they emit radiofrequency signals. A magnetic field gradient is applied to spatially encode the emitted signals. This causes frequencies at different locations to vary linearly with the gradient field, which allows spatial information to be recovered from the received signal using Fourier analysis.

Quality of MRI images are highly dependent on the acquisition parameters, but generally MRI has better soft tissue contrast than CT and less, yet good, spatial resolution. MRI-based image guide procedures faces many challenges. First, special cautions are necessary to work in the strong magnetic field created by the MRI magnet. Small ferromagnetic objects such as scalpels, scissors, probes can turn into life threatening bullets. Therefore, every object must be MRI compatible before it is allowed to be used in the MRI room. Second, the magnetic fields and radiofrequency waves can affect electronic devices. Third challenge is the limited work space, as the gantry is slightly wider than the patient, Figure 2.4. This leaves very little space for the surgeon’s hands or instruments.

## 2.3. INTRAOPERATIVE IMAGING

---



Figure 2.4: MRI machine ([www.healthcare.siemens.com](http://www.healthcare.siemens.com)).

### 2.3.3 Ultrasound

Ultrasound is defined as acoustic waves with frequencies above those which can be perceived by the ear, from about 20 kHz to several hundred MHz. The ultrasound spectrum used in medical devices ranges from 1 MHz to 10 MHz. This spectrum range meets the requirement of good resolution (small wavelength) and good penetrating ability (not too high frequency). The waves are produced by electrically driven acoustic transducers placed on the tissue surface. The transducers are made of piezoelectric materials, which have the property that electrical excitation is transformed into motion and pressure (acoustic waves). When the echo is reflected back to the transducer, the piezoelectric materials transform the reflected pressure field back into voltage, so it acts as an emitter and receiver as well [36].

Whenever a wave passes from a region of one value of acoustic impedance into a neighboring region of different impedance, a certain amount of the incident power is reflected at the boundary and the remainder continues as a transmitted wave, Figure 2.5. The reflected wave serves as an indicator of the boundary position and

shape, whereas the transmitted portion propagates deeper. The *reflection coefficient*  $R$  is defined as the ratio of the reflected pressure to the incident pressure. The value of  $R$  is proportional to the impedance mismatch between the two regions. As the difference between the two impedance values increases, the amount of reflection increases. The propagating wave encounters attenuation along its path due to several reasons. One is simply the reflection of part of the wave.

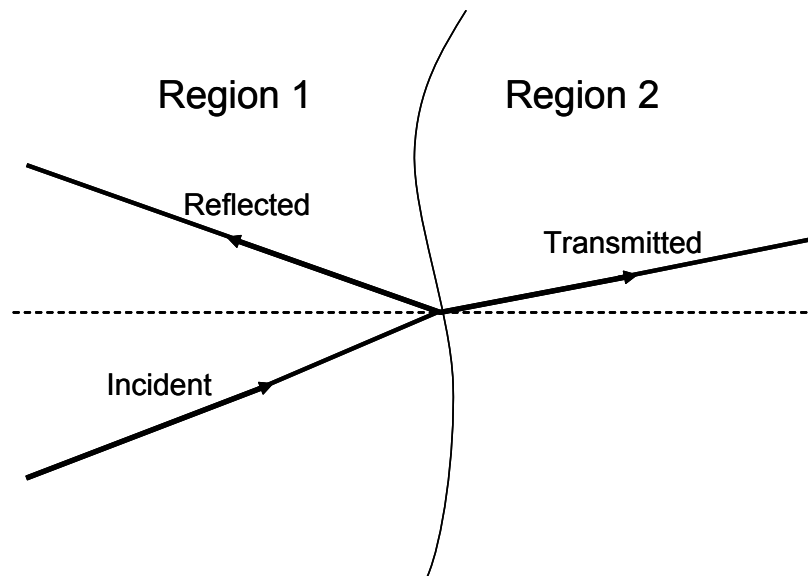


Figure 2.5: Illustration of the reflection and transmission of ultrasound waves due to acoustic impedance mismatch at the boundary between different regions.

Divergence of the wavefront and absorption of wave energy are other factors that cause attenuation. The exact attenuation encountered versus depth depends on tissue types, for soft tissue 1dB/cm is the typical attenuation rate [36]. Time gain compensation (TGC) amplifier compensates for the decreasing signal strength from deeper tissues due to the greater attenuation over longer paths. The gain of the amplifier varies according to the elapsed time since the transmission of the wave pulse.

The ultrasound transducer can take many forms (Figure 2.6), the most common is to have a linear array of acoustic elements which can acquire 2D images. Recently, 3D transducers have been developed, where a linear array of elements is oscillated across the field, or the transducer has a multi-row array of elements. The main drawback

### 2.3. INTRAOPERATIVE IMAGING

of ultrasound compared to CT or MRI is the limited field of view. Ultrasound is a regional imaging modality and typically cannot provide a complete cross sectional slices of the body. Also the signal-to-noise ratio is lower than CT and MRI, and the quality of the images may also be operator-dependent.

Nevertheless, ultrasound probes are relatively small and handheld, this makes ultrasound access to patient unsurpassed. This is particularly true for laparoscopy, since the probe must pass through a trocar to scan the organ. As for the limited field of view, the operator can easily and quickly adjust the field of view by repositioning the probe. Also by tracking the US probe as described in the next chapter, 3D image volumes with a larger field of view can be reconstructed.

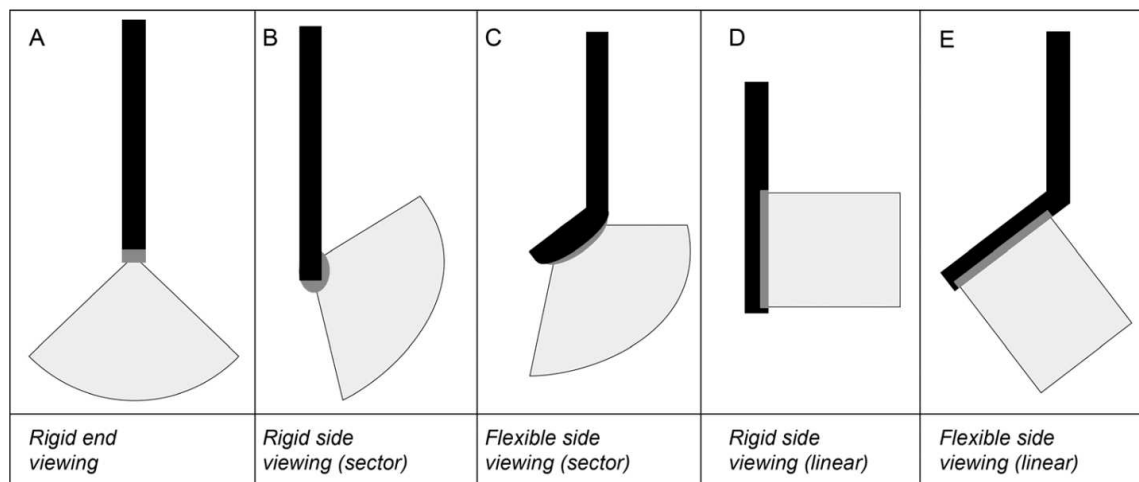


Figure 2.6: Configurations of different laparoscopic ultrasound probes (Solberg et al. [1]).

Intraoperative imaging may compromise spatial resolution in favor of improved temporal performance. Because ultrasound provides real-time radiation-free imaging capabilities, there is great benefit in using ultrasound in image guided interventions and also combining ultrasound with other imaging modalities. In addition, US scanners are compact, relatively inexpensive, and mobile. Specially in regions of the body susceptible to intraoperative motions and deformation of organs such as the abdomen, ultrasound can be used to update preoperative CT or MRI data using registration methods.

## 2.4 Visualization

Visualization in image guided interventions can be thought of as the interface between the surgeon and the patient. The role of visualization is to represent the organ and surgical environment in a clear and accurate way that helps guiding the surgeon to the treatment target. To this end, visualization should combine several signals, mainly tracking information and imaging data, into a common representative interface. Three-dimensional visualization is important to provide an intuitive representation to the surgeon. Multi-planar image representation typically uses orthogonal 2D images to give the viewer a sense of 3D. More complicated techniques are 3D volume and surface rendering, which require more computational overhead.

Before the surgery, visualization of preoperative data is essential to conduct surgery planning. The planning is crucial to understand the patient's anatomy and localize the disease, and then develop a treatment approach. Also based on the preoperative data, a patient specific model highlighting important structures and the target can be created, Figure 2.7. This model can provide basic guidance during the intervention. In deformable organs such as the liver, combining the preoperative model and intraoperative data to reflect the current surgical situation is necessary.

## 2.5 Registration

Registration is a key step in all image guided surgical procedures. Since different data streams, patient's images and tracked instruments, are collected relative to different reference frames, it is necessary to map the images in the tracking system coordinates. This applies to both preoperative and intraoperative images, however, in case of intraoperative ultrasound, probe calibration is the way to determine the spatial relation between the images and the tracking system (Chapter 3). To map preoperative data to the actual surgical scene, typically the whole anatomical structure is modeled as rigid bodies and rigid registration is performed. This initial registration

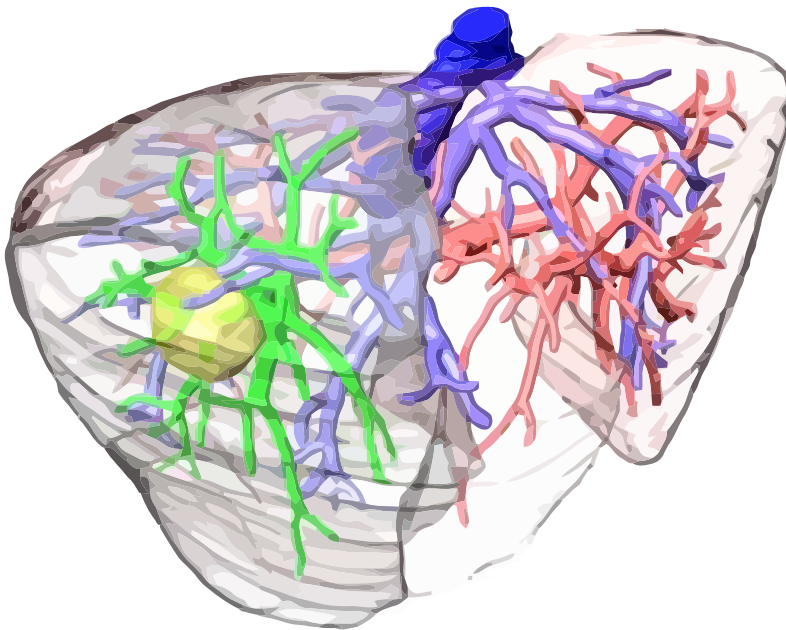


Figure 2.7: Liver model generated from preoperative data (Lange et al. [2]). The model shows the resection plan (darker region), tumor (yellow), and vessels to be resected (green).

is not sufficient when dealing with deformable organs, therefore, it is usually followed by further feature-based (landmark) or image-based registration.

### 2.5.1 Feature-Based Registration

Feature-based methods use homologous information extracted beforehand, like point sets or surfaces. Aligning those structures consequently aligns the objects as well. If a set of corresponding points is determined, using e.g. surface fiducials or manually selected anatomical landmarks, the rigid relation between the two point sets can be computed. The rationale for using feature-based methods is that it is independent of the characteristics of the registered objects. So one of the registration entities may arise from the actual physical patient, e.g. surface points, and the other from the image. Also feature-based registration behaves the same regardless of the registration being intermodal or intramodal.

The features can be either with known correspondence (paired-points) or without known correspondence, e.g. surface registration. In case of paired-points, the entries are two sets of corresponding 3D points obtained in two Cartesian coordinate systems. For a unique solution to exist, the data must include three or more noncollinear points. The advantage of the point-paired registration is that there are various least square closed form solutions [37, 38].

Unlike paired-points registration, there is no closed form solution to surface-based registration. Usually surface points are obtained by digitizing the surface and obtaining a point cloud. The iterative closest point (ICP) algorithm is one of the common surface registration algorithms. ICP is an iterative approach: the first step is to establish point correspondences, the second is to compute a transformation based on these matches. The incremental transformations compose the final registration result [39]. Given two non-corresponding point sets, an ICP framework consists of the following steps:

1. Find corresponding points, e.g. by matching the nearest neighbors.
2. Compute similarity between the matched sets, e.g. root mean square distance.
3. Compute incremental transformation by solving for the least squares solution using the current correspondences.
4. Apply the obtained transformation to one of the point sets.
5. Repeat the steps from 1 until either similarity is less than a certain threshold or the maximum number of iterations is reached.

### **2.5.2 Image-Based Registration**

Image-based (intensity-based) methods, on the contrary, use the images themselves rather than an indirect representation to compute the registration. Image-based registration is an optimization task with a cost function directly dependent on the image

intensity values and the transformation parameters. As this registration category doesn't necessarily need manual interaction, it is used often when automatic registration is required. Also as it uses more information compared to the feature-based registration, the overall registration accuracy is potentially better.

An image-based registration algorithm includes the following components:

1. Similarity measure (cost function)
2. Optimization algorithm
3. Interpolation method

The similarity measure is the most important component in the registration process, as it is the only component directly connected to the image data. Ideally, a similarity measure should have a unique global optimum for the correct transformation parameters. However, in reality the algorithm converges to the nearest local optimum. In general, similarity measures can be divided into two classes, functions that assume existence of a deterministic relationship between images (e.g. sum of squared differences) and functions that assume a stochastic relationship (e.g. mutual information). Several factors influence the choice of a cost function such as image characteristics (imaging modalities), computational complexity (time), and robustness. Therefore, there is no universal similarity measure that is optimal for all registration tasks.

## 2.6 Image Guided Liver Interventions

Surgical interventions on soft organs such as the liver is considered challenging in many aspects. The liver has a complex anatomical structure, it is deformable and subject to motion during the surgery. Surgical planning based on preoperative CT or MRI offers better 3D understanding of the organ's internal anatomy and helps to preserve adequate functional FLR after the treatment. Such planning is becoming a standard and is nowadays available from MeVis Distant Service AG (Bremen,

Germany), EDDA Technologies (Princeton, United States), and Intrasense (Montpellier, France). However, realization of the surgical plan in the actual surgery is not an easy task. One of the challenges is that the model does not reflect the actual situation of the liver during the surgery. Therefore, intraoperative computer-assisted navigation for liver interventions is of a great importance, especially for minimally invasive procedures.

### 2.6.1 Open Surgery

The development of liver navigation systems has been a topic of ongoing research since late 1990s. Herline et al. [40] at Vanderbilt University developed a navigation system for liver surgery and investigated the feasibility of adequate tracking accuracy. Their work was later on extended by applying a surface registration using a laser range scanner [41] and compensating for intraoperative soft-tissue deformations using a finite element model [42]. The system was then evaluated in a clinical trial on eight patients, where preoperative and intraoperative surface representations of the liver surface were registered using ICP. Currently, this system is commercially available as a product from the company Pathfinder Therapeutics (Nashville, Tennessee).

Another system for open liver surgery was developed at the Technical University of München. The proposed approach requires manual registration of preoperative CT data with intraoperative ultrasound images using a 6D mouse (space ball) [43]. A case report describing the system usage on a patient was presented by Oldhafer et al. [44]. An ultrasound-based navigation system was proposed by a group at Charité Hospital, Berlin. They optically tracked a 3D US probe to study the navigation feasibility based only on ultrasound images [45,46]. Recently, a group at the University of Bern, Switzerland, presented a navigation system which uses landmark-based registration to map preoperative data to the actual liver [47].

### 2.6.2 Minimally Invasive Interventions

While surgical navigation can be used in open liver surgery to provide better understanding of the anatomy, it is particularly useful and plays a major role in minimally invasive interventions. Unlike open surgery, the surgeon has no direct access to the liver in minimally invasive interventions, therefore, an image-guided navigation can be a necessity to precisely reach and treat the target tumor.

Similar to the open surgery approach, intraoperative images are acquired during the procedure to update the navigation system with the actual surgical situation. As explained in section 2.3, ultrasound is one of the best candidates for intraoperative imaging in laparoscopic procedures. However, due to probe size limitations, laparoscopic ultrasound (LUS) provides only 2D images. Although there is ongoing research to develop a 3D laparoscopic probe [48, 49], such a probe is not yet commercially available. Nevertheless, freehand 3D LUS can be obtained by tracking a 2D probe [50]. Several research groups have used this technique for navigation in laparoscopic surgery, Langø et al. [51] presented an overview of the current research work using tracked LUS.

One of the approaches to provide the surgeon with additional information beyond the live scene obtained via the laparoscope is to augment laparoscopic images with intraoperative 3D ultrasound/CT. Laparoscopic augmented reality was investigated by Konishi et al. [52] and Nakamoto et al. [53], they superimposed 3D LUS onto live laparoscopic images. They also described a calibration method for intraoperative correction of magnetic tracking distortion. Feuerstein et al. [54] registered both the laparoscope and the C-arm scanner in the same tracking coordinate system, thus allowing intraoperative CT volumes to be directly augmented on the live laparoscope video without further registration.

Langø et al. [55] (SINTEF Health Research, Trondheim, Norway) developed a navigation system for laparoscopic surgery and used fiducial-based registration. They also investigated the use of surface matching to register a surface model of the patient's

abdomen extracted from preoperative data to a corresponding surface generated in the operating room using a structured light technique. Similar surface digitization approach was developed by Billings et al. [56] using a time-of-flight camera. Martens et al. [57] (University of Lübeck) developed a laparoscopic liver surgery system, the navigation is done based on patient specific liver model generated from preoperative CT/MRI data. This model is registered to the actual organ in two steps:

1. Initial registration: model-to-patient registration is performed to approximately align the orientations of the liver model and the actual liver. This is done by automatically defining four points on the model, namely the end points of the the main two principal components axes. Then, the corresponding anatomical locations of the four points on the actual liver are touched roughly using a tracked calibrated pointer. This gives a very coarse initial registration.
2. Surface registration: accessible part of the liver surface is scanned to collect a point cloud. To facilitate the scanning process, a calibrated ultrasound probe is used as a pointer. After collecting the surface points, ICP is applied to register the points with the liver model.

These two laparoscopic systems, however, utilize only information on the surface of the liver, yet aim to solve the registration for the whole liver. Consequently, this technique cannot guarantee adequate navigation accuracy at the target tumor; nevertheless, it can serve as a starting point for further registration. Aiming for more accurate preoperative-intraoperative registration, several registration methods based on image information or features inside the liver have been proposed. As such registration is usually between ultrasound and CT/MRI, it is challenging to find an optimal similarity measure between different image types. Therefore, pre-processing of the data can be required to extract common features from the images. Penny et al. [58] first generated vessel probability images from MRI volumes and intraoperative tracked ultrasound images. Then, preoperative to intraoperative rigid registration was performed based on these probability images. Wein et al. [59,60] developed a method to simulate ultrasound-like images from CT images, then applied a modified normalized

cross correlation (NCC) similarity measure to align the simulated ultrasound (preoperative CT) to intraoperative ultrasound. After initial orientation alignment based on the tracking values, the similarity measure was applied in a brute-force fashion to determine large-scale translations. Then, 6D rigid and semi-affine registrations were applied to further improve the registration results.

As the liver is deformable, a non-rigid registration would ideally recover deformations intraoperatively. This is what motivated Lange et al. [2] to investigate the feasibility of an interactive non-rigid registration, however, for open surgery. They presented a combined landmark-intensity registration method based on vessels in preoperative CT and intraoperative 3D Doppler ultrasound. First, landmark-based rigid registration was applied after manually identifying eight landmarks (vessel bifurcations) on both CT and ultrasound images. Finally, non-rigid thin plate spline (TPS) registration was applied followed by the combined landmark-intensity method. Another elastic registration approach was proposed by Dagon et al. [61], first vessels were detected and segmented in tracked ultrasound frames to create 3D data points representing the skeleton of the vessels. Then, a non-rigid registration method was applied to deform the vascular structure of the preoperative 3D model according to the intraoperative structure. Recently, Olesch et al. [62] presented a non-rigid 2D/3D registration algorithm based on segmented vessels, they selected a number of intraoperative LUS frames, which have significant information such as a main vessel bifurcation, and then used them to map preoperative CT data.

Other navigation approaches are based directly on intraoperative images such as LUS. Harms et al. [63] compared 3D LUS with 3D transcutaneous ultrasound and CT, having CT as the gold standard. They reported that LUS-based navigation is feasible. Sjølie et al. [64] compared different US-based guiding techniques for RFA in the liver. They found that it was easier and more accurate to position the ablation needle based on 3D US images, however movement of the tumor during the procedure presented a challenge. Bao et al. [65] developed a prototype system for LUS-guided RFA, whereby ultrasound volumes can be acquired and reconstructed as necessary to present the most up-to-date image data before insertion of the RFA probe.

## 2.7 Objective

The aforementioned techniques present the state of the art in computer assisted minimally invasive intervention. The main problem investigated by different groups is how to keep the navigation system updated with the latest intraoperative situation. Solutions for this problem proposed either direct navigation based on intraoperative images or registration of preoperative data to the actual anatomy based on surface, landmark, or vessel information obtained during the procedure. The first part of this work demonstrates two new approaches for navigation in minimally invasive liver intervention. The approaches are based on segmentation and registration of tumors on intraoperative LUS images. The following criteria were considered to provide a practical solution that can be easily integrated into the surgical workflow:

- Fast and accurate intraoperative target update
- Automated process without landmark-based registration
- No major changes in the surgical workflow
- Repeatable when necessary during the procedure

In RFA procedures, accurately targeting the tumor is not sufficient for a successful treatment. However, feedback to the surgeon in such treatment is crucial. We demonstrate in the second part our trials to develop a method to correlate ablation feedback based on different monitoring modalities. Eventually, the aim is to standardize the interpretation of the ablation feedback, and consequently improve the efficiency of such important minimally invasive therapy.



## Part I

# Ultrasound-Guided Navigation



# Chapter 3

## 3D Freehand Ultrasound

### 3.1 Introduction

Intraoperative imaging is essential in image-guided interventions. Laparoscopic ultrasound is the commonly used modality to acquire intraoperative images of the liver, because it is a handy, safe and low cost modality (vs. CT or MRI). Thus, ultrasound is well integrated with the surgical environment. However, laparoscopic ultrasound doesn't support 3D imaging and provides a limited field-of-view that is typically not sufficient to cover the region of interest involved in a surgical procedure. Therefore, 3D volume reconstruction from freehand acquired 2D images can help to extend the field-of-view given by a laparoscopic probe. It also allows 3D segmentation and volume rendering of anatomical structures and tumors. Solberg et al. [50] presented a comprehensive review of freehand 3D US reconstruction algorithms.

### 3.2 Ultrasound Calibration

Three-dimensional tracking of 2D US images involves determination of the position and orientation of each 2D image with respect to a given 3D coordinate system. To

## 3.2. ULTRASOUND CALIBRATION

---

this end, a position sensor must be attached to the probe to determine the 6-DOF of every acquired frame. We used an US machine (Aloka SSD-3500, Japan) with a laparoscopic probe (Type 8666, Linear probe). Probe calibration was necessary to define the transformation between the acquired 2D images and the position sensor attached to the probe.

### 3.2.1 Spatial Calibration

The idea of the calibration is to find the spatial relationship between a group of features (homologous points) which can be identified in both the image space and also in a phantom space with known geometric properties. The calibration was performed by mounting a 6-DOF EM sensor (Aurora, Northern Digital Inc., Waterloo, Canada) on the LUS probe and scanning a *Double-N* phantom. The phantom consists of two horizontally shifted layers of *N-fiducials* parallel to the x-y plane of the phantom coordinate system [66, 67]. The *N-fiducials* intersection with the US image plane showed 6 dots in the image. The centers of those dots were automatically identified in the images using an adaptive thresholding algorithm [68]. Figure 3.1 illustrates the intersection of an US plane with a single *N-fiducial*.

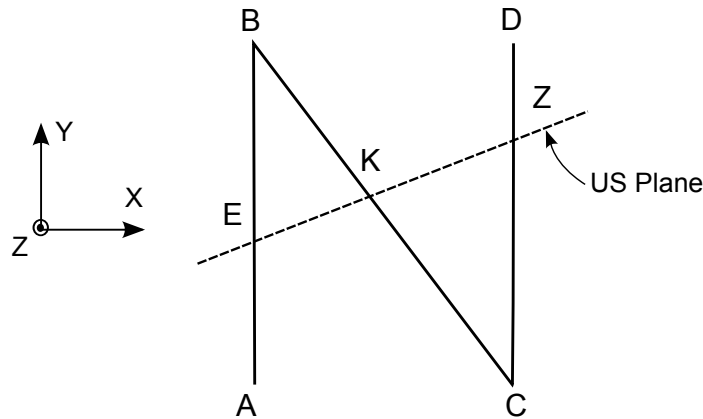


Figure 3.1: Ultrasound plane (dashed line) intersecting an *N-fiducial* at the points E, K, and Z.

On the dashed line, coordinates of the point  $(X_K, Y_K)$  in the phantom space can be determined based on the similar triangles BEK and KZC in Fig. 3.1.

$$\begin{aligned} X_K &= X_B + \frac{KE}{EZ}(X_C - X_B) \\ Y_K &= Y_B + \frac{KE}{EZ}(Y_C - Y_B) \end{aligned} \quad (3.1)$$

The ratio  $KE/EZ$  was measured from the locations of the three collinear dots in the US image; scale of the image was obtained previously from the US machine. The coordinates of the vertices in the phantom space  $(X_B, Y_B)$  and  $(X_C, Y_C)$  were known from the phantom geometry. Since each three dots are collinear, there is more than one solution for the coordinates of points E and Z in the phantom space, i.e. more than one solution for the fiducials-to-image transformation  ${}^F T_I$ . Figure 3.2 shows the calibration procedure and Figure 3.3 illustrates the calibration transformations.

The sensor-to-image transformation  ${}^S T_I$  is determined by the equation:

$${}^S T_I = {}^S T_W \cdot {}^W T_P \cdot {}^P T_F \cdot {}^F T_I \quad (3.2)$$

The sensor-to-world transformation  ${}^S T_W$  was measured by the tracking device. The origin of the world coordinate system is defined by the EM transmitter and must be fixed relative to the phantom. The sensor should be placed as close as possible to the imaging plane, to minimize angle effect errors. The world-to-phantom transformation  ${}^W T_P$  is determined using a second sensor fixed to the phantom body. The phantom-to-fiducials transformation  ${}^P T_F$  represents the relation between the fixed sensor and the fiducial geometry, this transformation is measured once per phantom using a tracked calibrated pointer. The sensor-to-image transformation  ${}^S T_I$  is calculated using every  ${}^F T_I$  solution.

The *N-fiducial* positions in the physical phantom space were calculated using every calibration result, and then compared to a ground truth – the known fiducial locations from the phantom geometry. The transformation that minimizes the error was accepted as the right calibration result. After obtaining the calibration matrix, it was possible to transform every pixel in the image space into the world space.

## 3.2. ULTRASOUND CALIBRATION

---



Figure 3.2: Calibration of the LUS probe using two EM sensors, one attached to the probe and the other to the calibration phantom. The US image with the six dots shows the intersection of the image plane with the  $N$ -fiducials in the phantom.

### 3.2.2 Temporal Calibration

The video output from the US machine was captured using a video-to-FireWire converter (The Imaging Source Europe GmbH, Bremen, Germany). As the video converter acquisition rate was slightly slower than the tracking frequency, a temporal calibration was required to synchronize each US image with an associated tracking transformation. This was accomplished by interpolating the tracking data stream between the B-scans using spherical linear interpolation (slerp) [69]. Figure 3.4 shows how the tracking data were interpolated, where  $p_{interp}$  is the tracking value interpolated between  $p_j$  and  $p_{j+1}$  given the time stamps  $t_{US}$  and  $t_{track}$  of the US and tracking data.

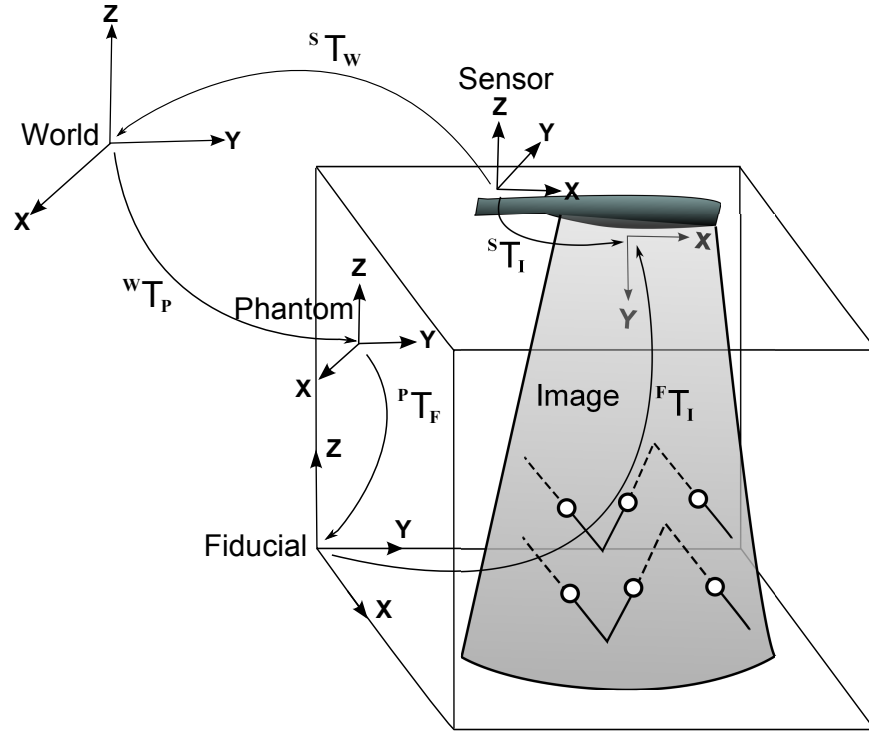
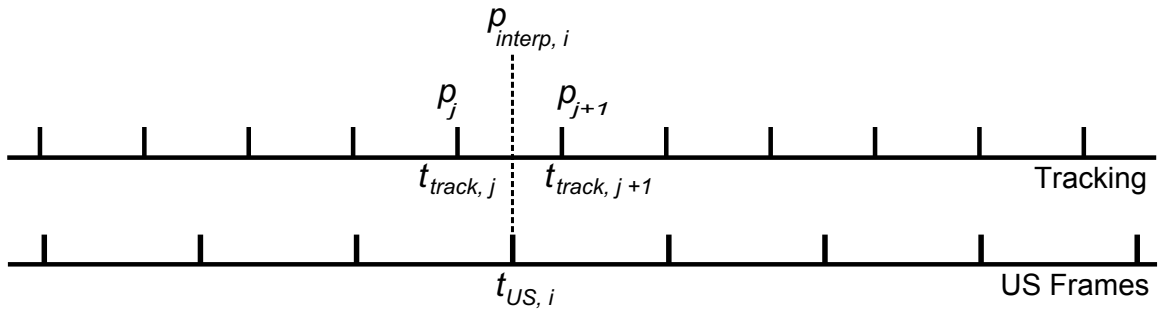

 Figure 3.3: Ultrasound calibration using an  $N$ -fiducial phantom.


Figure 3.4: Interpolation of tracking data to match the corresponding US frames.

### 3.3 Volume Reconstruction

While the probe acquired US images, the tracking system generated a series of transformation matrices representing the position and orientation of the US probe. Equation (3.3) converts a point in the  $n^{\text{th}}$  image into the world coordinate system and represents it in the reconstructed volume space:

### 3.3. VOLUME RECONSTRUCTION

---

$$\begin{pmatrix} x_n \\ y_n \\ z_n \\ 1 \end{pmatrix} = {}^W T_V \cdot {}^S T_W \cdot {}^I T_S \cdot \begin{pmatrix} s_x \cdot u_n \\ s_y \cdot v_n \\ 0 \\ 1 \end{pmatrix} \quad (3.3)$$

Figure 3.5 illustrates the transformations required to map a point from an image to the world space. For practical reasons, the origin of the image is often placed at the top center of the image. For a curved-array probe, this corresponds to the center of curvature. This point is preferred because its position does not vary when changing the depth setting.

In Figure 3.5, an arbitrary point at position  $(u, v)$  relative to the image origin was first scaled by  $s_x$  and  $s_y$ . Then it was mapped in the sensor space by the calibration transformation  ${}^I T_S$ , then into the world space by  ${}^S T_W$ , and finally in the volume space by  ${}^W T_V$ . Pixels in the acquired US images were traversed and each pixel value was assigned to one or several voxels in the output volume according to equation (3.3). Multiple contributions to the same voxel were averaged. Afterwards, small gaps in the output volume were filled by combining values from the local neighborhood using a  $(3 \times 3 \times 3)$  grid [70].

The 3D US reconstruction was done in two steps: data acquisition, and then volume reconstruction. Using a PC with a 3 GHz Core2 Duo CPU and 4 GB memory, the average time required to transform an US frame into the output volume was 0.04 sec, i.e. a reconstruction rate of ca. 25 Hz. Given that the acquisition rate of the US images is app. 16 Hz in our setup, the speed of the reconstruction algorithm is sufficient for a real time reconstruction. Dense scanning of the region of interest containing the tumor was necessary to avoid having a sparse volume due to big gaps between different frames. The region of interest was scanned back and forth for a period of 20 sec before reconstructing the volume. Filling small gaps in the local neighborhood around mapped gray values in the volume took in average 0.16 sec.

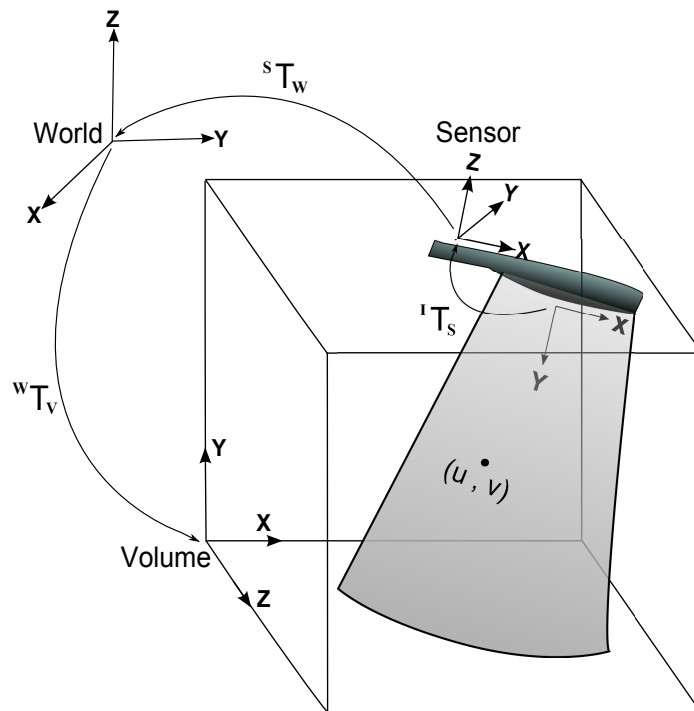


Figure 3.5: Sketch illustrating the volume reconstruction transformations.

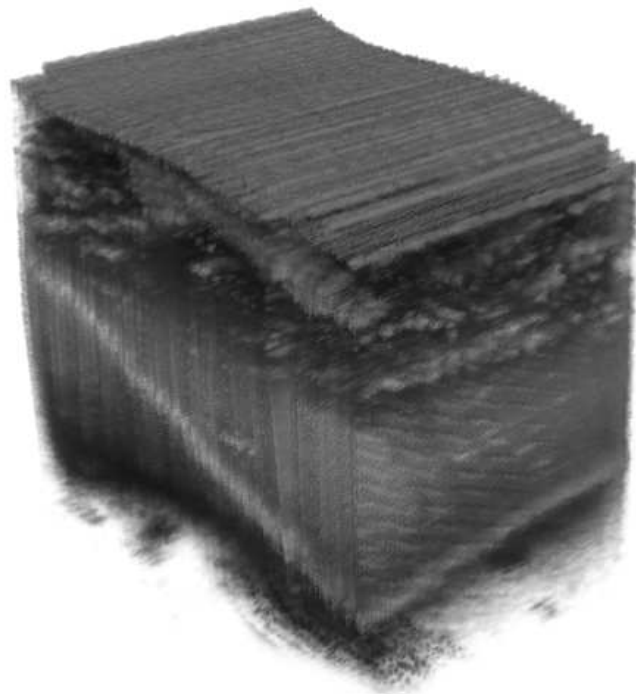


Figure 3.6: Reconstructed US volume.

The dimensions of the resulting volumes varied relative to the scanned area. In average the US volume size was ( $480 \times 240 \times 300$  voxels), which was equivalent to an actual volume of ( $7 \times 4 \times 4.5$  cm<sup>3</sup>) in the tissue. The time required to reconstruct such a volume was 18 sec. Figure 3.6 shows a reconstructed US volume.

## 3.4 Conclusion

We presented in this chapter the steps to reconstruct a volume from tracked freehand laparoscopic ultrasound. After attaching a position sensor to the ultrasound probe, calibration was required to determine the transformation between the acquired images and the sensor. Then, every image pixel was mapped into a volume in the tracking system (world) space. The explained volume reconstruction method is used in the following chapters to create 3D US images of the tumor region.

# Chapter 4

## Tumor Segmentation

### 4.1 Introduction

In this chapter we present two different segmentation algorithms to segment tumors in US images: level set and graph cut segmentation methods. In the following chapters, these methods are applied as part of tumor localization techniques. Tumor segmentation in US images is challenging due to characteristic artifacts such as speckles, attenuation, and shadows. While conventional segmentation methods such as region growing and threshold based algorithms have the advantage of being simple and fast, they are typically not sufficient to segment US images [71]. Therefore, more robust segmentation algorithms based on optimization of energy functions are adapted to segment tumors in US images.

### 4.2 Level Set Segmentation

The level set method is an implicit representation of a surface. The contour of this surface is embedded as the zero level set of a higher dimensional function called the level set function  $\phi(\mathbf{x}, t)$ . Level set methods rely on partial differential equations

(PDE) to model deforming isosurfaces [72]. Level sets can be used for segmentation by using image information in a PDE. Solving this PDE over the entire image domain yields the level sets of the image. The target segmentation solution is where the zero level set  $\{\mathbf{x} \mid \phi(\mathbf{x}, t) = 0\}$  coincide with the boundaries of the object we want to segment.

### 4.2.1 Mathematical Background

Consider a boundary, either a curve in two dimensions (or a surface in three dimensions), separating one region from another<sup>1</sup>. For instance, let  $\Gamma(t)|_{t=0}$  be a smooth initial contour in Euclidean plane  $\mathbb{R}^2$  (Figure 4.1), and let  $\Gamma(t)$  be the family of curves generated by moving  $\Gamma(t)|_{t=0}$  along its normal vector field with a speed  $F$ , and  $\mathbf{x}(s, t)$  is the position vector which parametrizes  $\Gamma(t)$  by  $s$ .

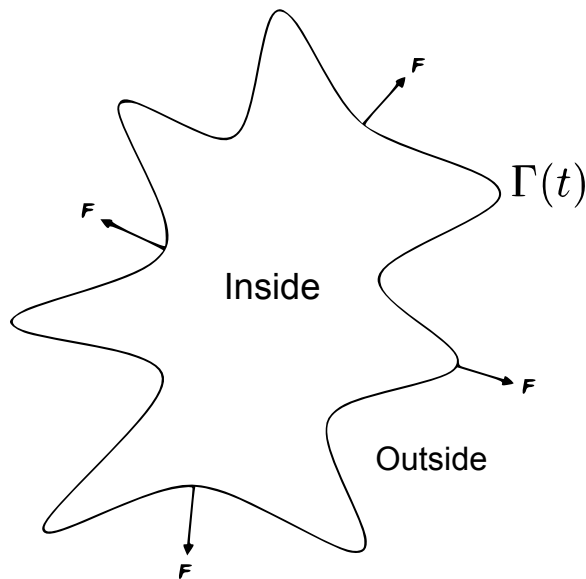


Figure 4.1: Curve propagation with speed  $F$  in the normal direction.

The central idea in the level set approach is to represent the front (evolving curve)  $\Gamma(t)$  as the zero level set  $\{\mathbf{x} \mid \phi(\mathbf{x}, t) = 0\}$  [73]. Let  $\phi(\mathbf{x}, t)|_{t=0}$  be defined by

---

<sup>1</sup>The derivation of the evolution equation is based on the derivation given by Malladi et al. [73].

$$\phi(\mathbf{x}, t)|_{t=0} = \pm d, \quad (4.1)$$

where  $\mathbf{x} \in \mathfrak{R}^N$ ,  $d$  is the distance from  $\mathbf{x}$  to  $\Gamma(t)|_{t=0}$ , and the plus (minus) sign indicates if the point is outside (inside) the initial surface  $\Gamma(t)|_{t=0}$ . Thus, we have

$$\Gamma(t)|_{t=0} = \{\mathbf{x} \mid \phi(\mathbf{x}, t)|_{t=0} = 0\}. \quad (4.2)$$

As an example of front propagation, suppose the initial front  $\Gamma$  at time  $t = 0$  is a circle in the  $\mathfrak{R}^2$ -plane. Also the initial front is the zero level set  $\{\mathbf{x} \mid \phi(\mathbf{x}, t) = 0\}$  of an initial surface  $z = \phi(x, y, t)|_{t=0}$  in  $\mathfrak{R}^3$  (Figure 4.2a). And the front at any time  $t$  is  $\Gamma(t) = \{\mathbf{x} \mid \phi(\mathbf{x}, t) = 0\}$  (Figure 4.2b). From this example we can see how the zero level set always represents the moving front at any time  $t$ .

To derive an equation for the evolving function  $\phi(\mathbf{x}, t)$  which embeds the front  $\Gamma(t)$  as the zero level set  $\{\mathbf{x} \mid \phi(\mathbf{x}, t) = 0\}$ , let  $\mathbf{x}(t)$  be the path of points along the propagating front,  $\dot{\mathbf{x}} = F(\mathbf{x}(t))$  with  $F$  indicating the speed in the normal direction, and the vector  $\dot{\mathbf{x}}$  is normal to the front at  $\mathbf{x}(t)$ . Since the evolving function  $\phi$  is always zero on the propagating front, we must have

$$\phi(\mathbf{x}(t), t) = 0. \quad (4.3)$$

Obtaining  $\partial\phi/\partial t$  is an implicit differentiation problem [74]. Let's assume a one-dimensional function  $\phi(x(t), t) = 0$ . The total derivative for this function is given by

$$d\phi = \frac{\partial\phi}{\partial x} dx + \frac{\partial\phi}{\partial t} dt, \quad (4.4)$$

and multiplication of the above equation by  $1/dt$  yields

$$\frac{d\phi}{dt} = \frac{\partial\phi}{\partial x} \frac{dx}{dt} + \frac{\partial\phi}{\partial t}. \quad (4.5)$$

Let's generalize equation (4.5) for higher dimensions

$$\frac{d\phi}{dt} = \nabla\phi(\mathbf{x}(t), t) \frac{d\mathbf{x}}{dt} + \frac{\partial\phi}{\partial t}. \quad (4.6)$$

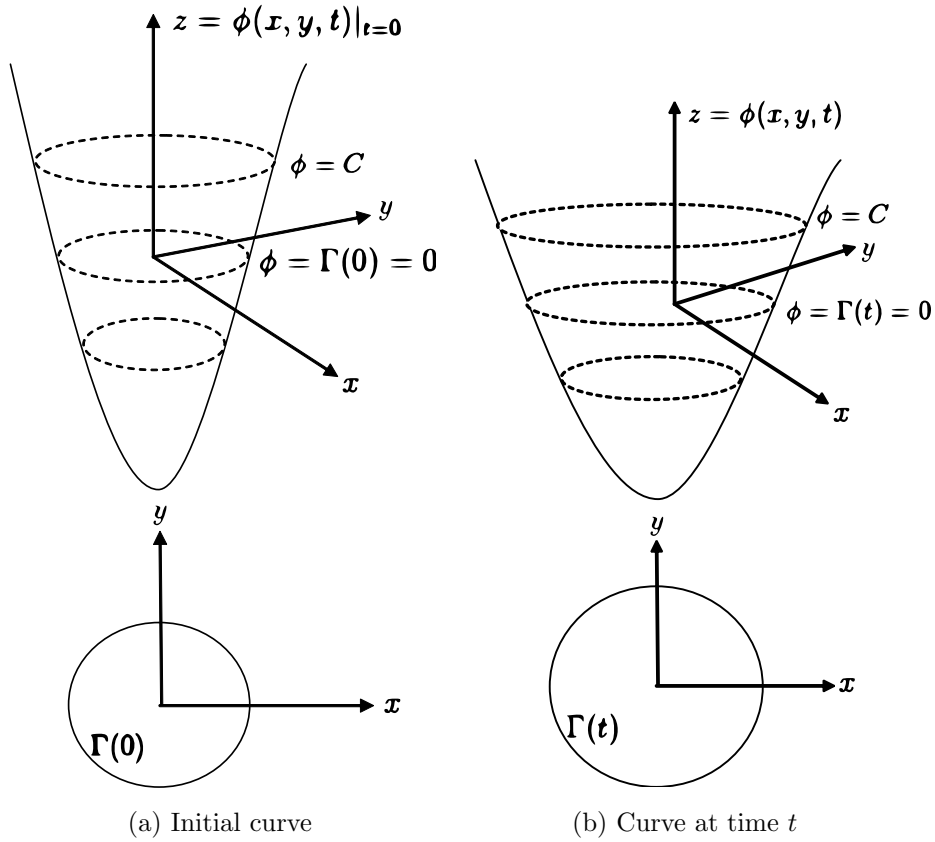


Figure 4.2: Level sets and front motion (a) The curve  $\Gamma$  and the surface  $\phi(x, y)$  at  $t = 0$ . (b) The curve  $\Gamma$  and the surface  $\phi(x, y)$  at time  $t$ .

Since the front  $\Gamma(t)$  is always represented by the zero level set, then  $\Gamma(t)|_t = \{\mathbf{x} \mid \phi(\mathbf{x}, t) = 0\}$ , and also  $\Gamma(t)|_{t+\Delta t} = \{\mathbf{x} \mid \phi(\mathbf{x}, t + \Delta t) = 0\}$ :

$$\Rightarrow \frac{d\phi}{dt} = 0,$$

and

$$\frac{\partial\phi}{\partial t} + \nabla\phi(\mathbf{x}(t), t) \frac{d\mathbf{x}}{dt} = 0. \quad (4.7)$$

Since  $F$  supplies the speed in the outward normal direction (see Figure 4.1), then

$$\frac{d\mathbf{x}}{dt} = F\hat{\mathbf{n}} = F \frac{\nabla\phi}{|\nabla\phi|}, \quad (4.8)$$

where  $\hat{\mathbf{n}} = \nabla\phi/|\nabla\phi|$ . By substitution in equation (4.7), we obtain

$$\frac{\partial\phi}{\partial t} + F \frac{|\nabla\phi|^2}{|\nabla\phi|} = 0, \quad (4.9)$$

which after algebraic simplification yields the evolution equation, namely

$$\boxed{\frac{\partial \phi}{\partial t} + F|\nabla \phi| = 0, \text{ with initial condition } \phi(\mathbf{x}, t)|_{t=0}.} \quad (4.10)$$

### 4.2.2 Segmentation using Level Set

Segmentation of an object is the detection of its boundaries. So, we can segment the desired object if we make the propagating front take the shape of its boundaries. To do that, the evolving front should be forced to stop in the vicinity of the object boundaries. In other words, we should define the final shape of the propagating front, i.e. when the propagating front reaches the steady state and all the points on the front come to a stop, to be the shape of the desired object boundaries.

The only input we have is the image information, and our goal is to define a speed function from this information that forces the propagating front to stop at the object boundaries. Let's split the speed function  $F$  into two components:  $F = F_P + F_G$ . The propagation term  $F_P$  is independent of the moving front's geometry. The front uniformly expands or contracts with speed  $F_P$  depending on its sign.  $F_G$  depends on the geometry of the front. Then equation (4.10) can be rewritten as

$$\frac{\partial \phi}{\partial t} + F_P|\nabla \phi| + F_G|\nabla \phi| = 0. \quad (4.11)$$

Let  $\mathbf{g}_I$  be defined as

$$\mathbf{g}_I(x, y) = \frac{1}{1 + |\nabla G_\sigma * I(x, y)|}, \quad (4.12)$$

then the evolution equation now is

$$\frac{\partial \phi}{\partial t} + \mathbf{g}_I(F_P + F_G)|\nabla \phi| = 0. \quad (4.13)$$

The term  $\mathbf{g}_I$  acts as an image dependent stopping function as it has values that are closer to zero in regions of high image gradient and values that are closer to unity

## 4.2. LEVEL SET SEGMENTATION

---

in regions with relatively constant intensity. The geometry dependent term  $F_G$  in equation (4.13) can be defined as the local curvature of the front. The curvature is defined as the divergence of the gradient of the unit normal vector to the front

$$\hat{\mathbf{n}} = \frac{\nabla\phi}{|\nabla\phi|}, \quad (4.14)$$

thus the curvature is given by

$$\kappa = \nabla \cdot \frac{\nabla\phi}{|\nabla\phi|} = \frac{-\phi_{xx}\phi_y^2 - 2\phi_x\phi_y\phi_{xy} - \phi_{yy}\phi_x^2}{(\phi_x^2 + \phi_y^2)^{3/2}}. \quad (4.15)$$

This curvature speed term is used to control the shape of the evolving front. The curvature speed at a certain point on the front acts inwards and is proportional to the curvature magnitude of the front at this point (Figure 4.3). The effect of this term is to slow down the front evolution at places of high curvature, such as sharp corners, and consequently smooth out the high curvature regions of the front [75]. It has also a regularization effect on the front which prevents *leakage* in case of incomplete boundary.

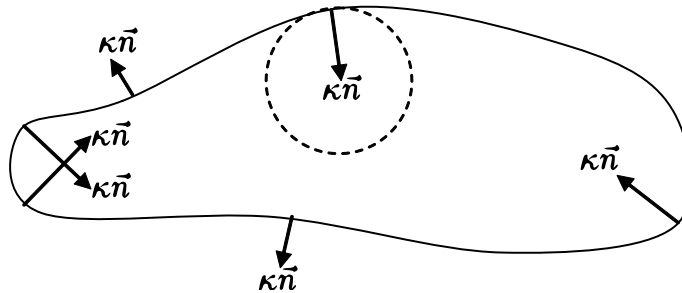


Figure 4.3: Curvature forces act in the direction of the unit normal vector.

### Surface Curvature (3D)

Curvature on a 3D surface is more difficult to define as there are infinitely many curves through a point on the surface [76]. However, there are two principal directions of

maximal and minimal curvatures (Figure 4.4). Once the principal directions at a point  $p$  are determined, two curves through the point  $p$  along those directions can be identified and curvature can be calculated similar to equation (4.15).

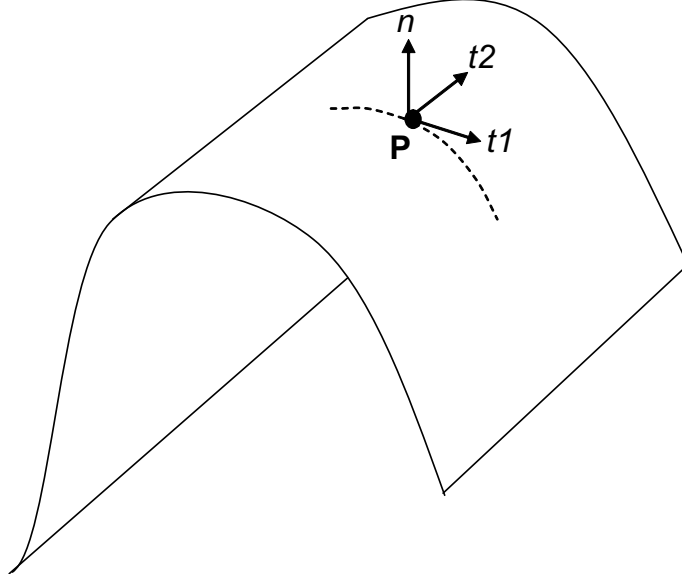


Figure 4.4: Principal curvature directions.

Let the curvatures  $\kappa_1$  along  $t_1$  and  $\kappa_2$  along  $t_2$  be the principal curvatures at some point  $p$  on the surface. Then we can locally determine the shape of the surface around  $p$  by calculating the *mean curvature* which is given as

$$H = \frac{\kappa_1 + \kappa_2}{2}. \quad (4.16)$$

### Final Evolution Model

Back to the evolution model  $\partial\phi/\partial t + \mathbf{g}_I(F_P + F_G)|\nabla\phi| = 0$ , the front evolves under two simultaneous motions, propagation force  $F_P$  and geometrical force  $F_G$ . Since the front expands or contracts with a constant speed, we can set  $F_P = c$ , where  $c$  is a scalar constant.  $F_G$  is proportional to the curvature magnitude and acting inwards, so it can be replaced by  $F_{curv} = -\epsilon\kappa$  and the evolution equation becomes

$$\frac{\partial\phi}{\partial t} + \mathbf{g}_I(c - \epsilon\kappa)|\nabla\phi| = 0. \quad (4.17)$$

Let's now add a third speed term to the evolution equation, advection speed  $F_{adv}$ , which is introduced by Caselles et al. [77]. The final model is called *Geodesic Active Contours*,<sup>2</sup> and can be written as

$$\boxed{\frac{\partial\phi}{\partial t} + \mathbf{g}_I(c - \epsilon\kappa)|\nabla\phi| + \alpha(\nabla\mathbf{g}_I \cdot \nabla\phi) = 0.} \quad (4.18)$$

The scalar constants  $c$ ,  $\epsilon$ , and  $\alpha$  weight the relative influence of each of the speed terms on the propagation of the front. Note that in equation (4.17) the front stops when  $\mathbf{g}_I = 0$ . This happens in case of ideal edges, but sometimes the boundaries in real images have high variations of the gradient along their boundaries. In some other cases the boundaries are incomplete or have small gaps.

The advection term  $\nabla\mathbf{g}_I \cdot \nabla\phi$  increases the attraction of the deforming front towards the boundary of the desired object, regardless of the possible high variation in the gradient values along the boundary. Figure 4.5 shows an image of a disc with high intensity value and low intensity background, mimicking the boundary of an object. A one-dimensional image  $I(x)$  is obtained by taking a cross section at one point along the disc.

The image is smoothed by the convolution with the Gaussian filter  $G_\sigma$ . Figure 4.6 shows the smoothed image and its  $\mathbf{g}_I$  function. The gradient vectors  $\nabla\mathbf{g}_I$  point toward the middle of the boundary [77]. Those vectors steer the propagating front into the “valley” of  $\mathbf{g}_I$  function. When we apply the same concept on the whole 2D image, the new term  $\nabla\mathbf{g}_I \cdot \nabla\phi = \nabla\mathbf{g}_I \cdot \mathbf{n}$  leads the evolving front to the boundary of the object and has the maximum effect when the gradient vectors coincide with the normal direction of the evolving front. Eventually, it forces the front to stay in the vicinity of the boundary.

---

<sup>2</sup>For details about the derivation of Geodesic Active Contours, see Caselles et al. [77].

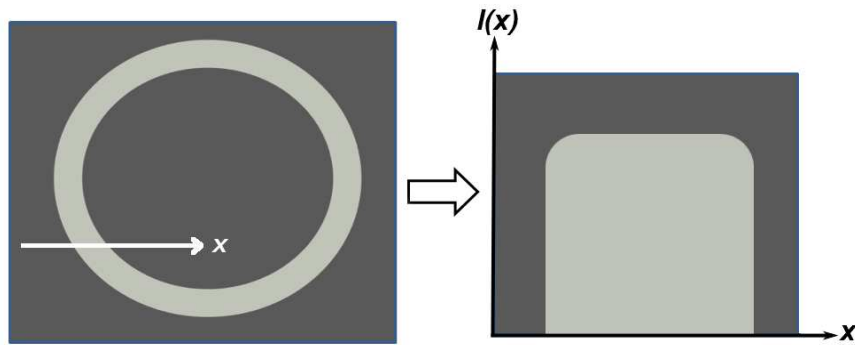


Figure 4.5: Image of a disc (boundary) and a through-cut at one point.

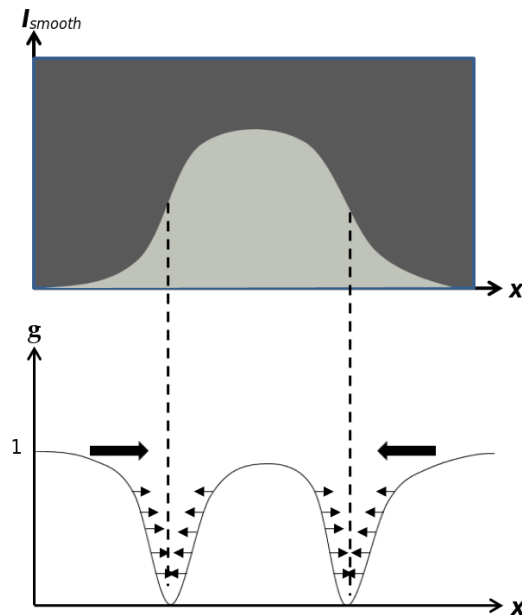


Figure 4.6: The smoothed 1D image and its  $g_I$ , arrows show  $\nabla g_I$  direction.

### 4.2.3 Segmentation Steps

In the previous section we presented the level set method and how different speed terms are integrated in the final evolution equation. This section describes the steps used to segment tumors in 3D US volumes. As a preprocessing step, we apply a median filter to smooth out the noise which might trap the evolving contour in a local minima. Figure 4.7 shows a metastatic liver tumor and the effect of the median filter on the image.

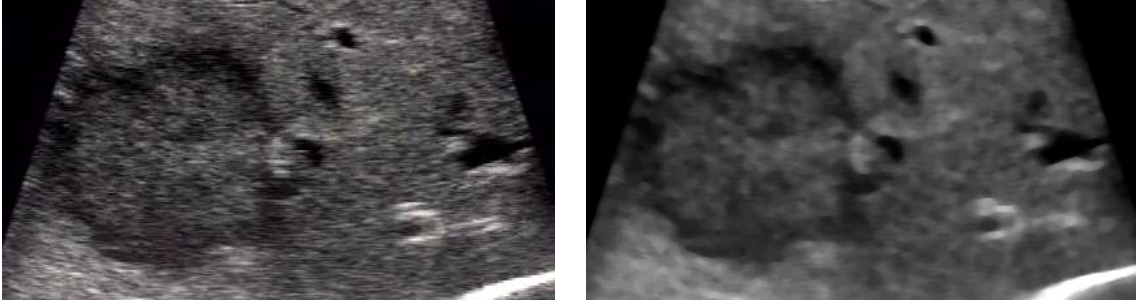


Figure 4.7: Effect of median filter on an US image of metastatic liver tumor.

The evolution PDE in equation (4.10) needs an initial value. The initial value in this case is an initial level set. In other words, it is the solution of a cheap and fast evolution PDE which gives an initial level set function  $\phi(\mathbf{x}, t)|_{t=0}$ . This fast evolution algorithm is known as the fast marching.

Fast marching algorithm starts the evolution from a seed point with a constant speed value. The pixel values of a unit speed image is used to determine the speed in the fast marching PDE, equation (4.19). The fast marching acts as a distance function to one or more user provided seed points.

Let  $T(\mathbf{x})$  be the arrival time of the front that indicates, for each pixel, how much time it would take to arrive at the pixel location, and since  $distance = speed \times time$ , we have

$$|\nabla T|F = 1, \quad T(\mathbf{x}) = 0 \text{ for seed points } \mathbf{x}. \quad (4.19)$$

Using a unit speed image, the equation reduces to the PDE of the distance function

$$|\nabla T| = 1, \quad T(\mathbf{x}) = 0 \text{ for seed points } \mathbf{x}. \quad (4.20)$$

Figure 4.8 shows a geometrical interpretation of the distance function in 1D and 2D. The output of the fast marching is the initial level set function and the zero level set of this function is the initial front  $\Gamma(0) = \{\mathbf{x} \mid \phi(\mathbf{x}, t) = 0\}|_{t=0}$ .

Now the level set algorithm is initialized and ready to evolve according to the governing speed terms. But before that, a sigmoid filter is applied to the input image in

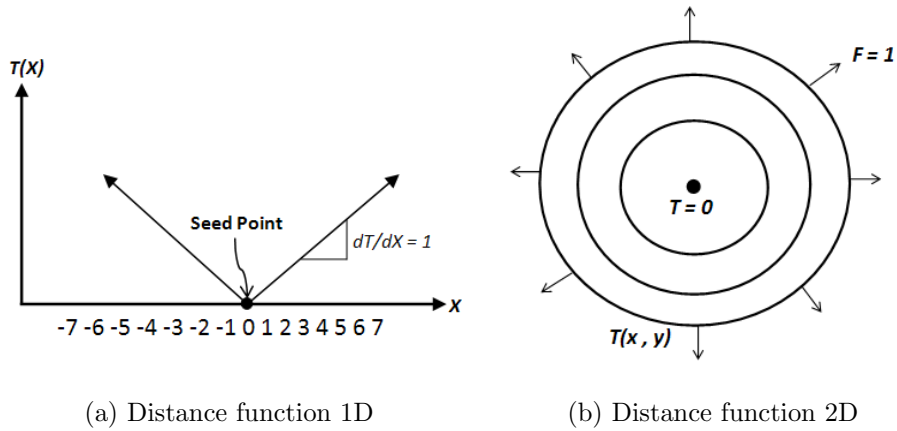


Figure 4.8: Geometric interpretation of the distance function. (a) 1D distance function. (b) 2D distance function.

order to enhance edges at the borders of the tumor by increasing the difference between gray values inside and outside the tumor. The sigmoid filter is a point-to-point intensity nonlinear mapping which transforms a certain range of gray values into a new range of gray values while keeping a continuous and smooth transition in the borders of the range [78].

$$I_{new} = (Max - Min) \frac{1}{(1 + \exp^{-\frac{I-\beta}{\alpha}})} + Min. \quad (4.21)$$

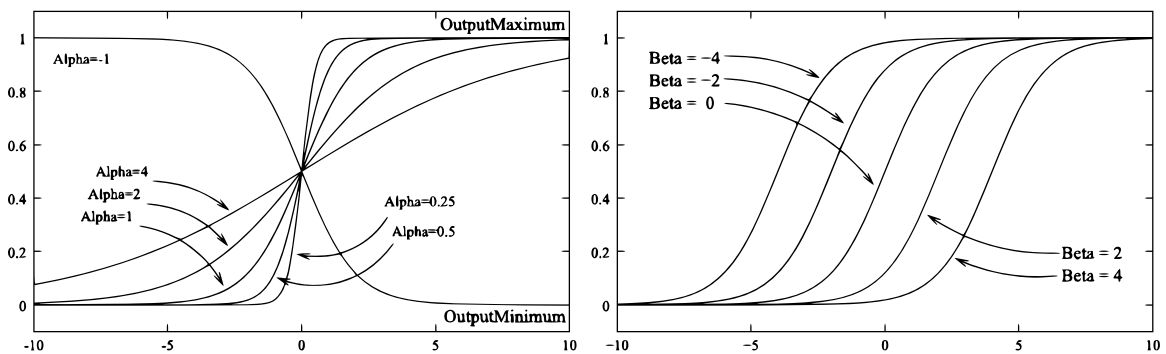


Figure 4.9: The significance of  $\alpha$  &  $\beta$  in equation (4.21). The  $\alpha$  parameter defines the width of the intensity window. The  $\beta$  parameter defines the center of the intensity window<sup>3</sup>.

<sup>3</sup>Source: *ITK Software Guide* [78]

## 4.2. LEVEL SET SEGMENTATION

---

In equation(4.21),  $I$  is the input gray value,  $I_{new}$  the output gray value,  $Min, Max$  are the minimum and maximum values of the output image,  $\alpha$  defines the width of the input gray value range, and  $\beta$  defines the gray value around which the range is centered. Figure 4.9 illustrates the significance of each parameter. The ideal effect of the sigmoid filter is that the gray values outside the tumor are mapped to the maximum gray level and the gray values inside are mapped to the minimum gray value, or vice versa depending on the sign of  $\alpha$ , while keeping a smooth transition at the border.

In the segmentation process, user interaction is required only once to initialize the segmentation algorithm. A cross section of the tumor was visualized by slicing through the reconstructed US volume. Using the mouse pointer a line was drawn along the tumor diameter. The mid point of this line was fed as a seed point to the fast marching algorithm. Also, the length of this line gives an estimate of the tumor size, and accordingly the region of interest (ROI) around the tumor. This ROI is preprocessed using a median filter to smooth out the noise, followed by the sigmoid filter explained before to enhance tumor edges. The sigmoid  $\alpha$  was set to  $\pm 1.5$  depending on whether the tumor hyper or hypoechoic, while  $\beta$  was automatically set to the mean gray value of the image area covered by the circle defined by the line drawn along the tumor.

The output of the sigmoid filter is the *edge image* (Figure 4.10), from its name it defines the edges of the borders at which the propagating front should stop. However, some parts of the tumor contour are not well defined by the sigmoid filter. Thus, the sigmoid filter is not completely delineating the tumor from the surrounding tissue. Nevertheless, those edges defined in the sigmoid image, even if they don't draw a complete contour, contribute significantly to the speed terms in equation (4.18).

Finally, the initial contour (fast marching output) evolves according to the level set function to segment the 3D tumor in the *edge image*. Figure 4.11 shows how the initial contour evolved iteratively to eventually take the shape of the tumor.

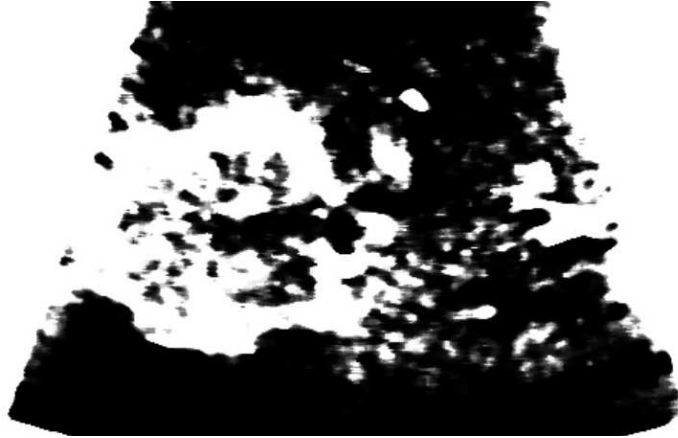


Figure 4.10: Tumor image after applying sigmoid filter, most of the pixel intensities inside the tumor are mapped to a maximum value and most of those outside are mapped to a minimum value. The tumor borders are not completely defined by the sigmoid filter, however edges making parts of the tumor contour contribute significantly to the energy terms.

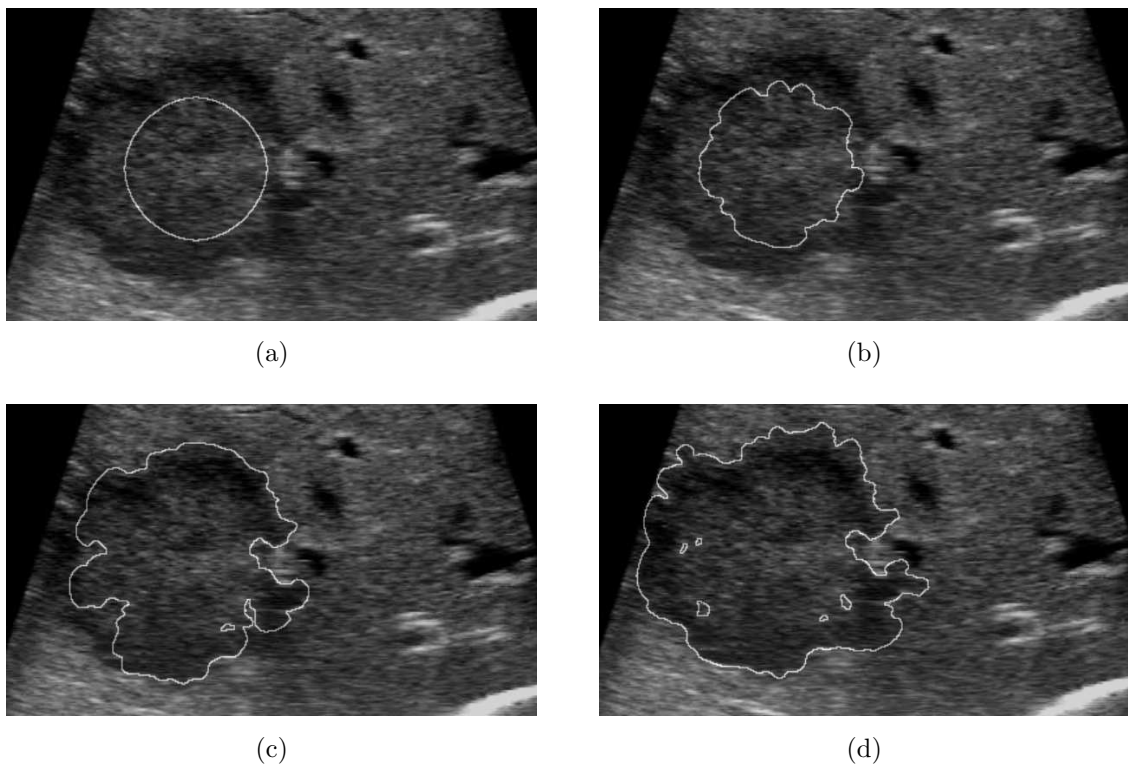


Figure 4.11: Initial contour evolves according to the governing level set function to eventually take the shape of the tumor.

## 4.3 Graph Cut Segmentation

Image segmentation using graph cut algorithms was proposed by Boykov et al. [79]. The graph cut segmentation framework uses implicit representation of object boundaries, thus the method is considered a discrete counterpart of level sets. It doesn't rely on approximating numerical schemes, instead a discrete energy formula is solved directly in a graph-based optimization. This makes the optimization potentially fast and numerically stable. As explained in more details later in this section, the discrete energy can combine both boundary and regional properties of the image segments.

A graph  $\mathcal{G} = \langle \mathcal{V}, \mathcal{E} \rangle$  consists of nodes (vertices)  $\mathcal{V}$  and lines connecting them called edges  $\mathcal{E}$ . The nodes correspond to image pixels and each edge between them are assigned a weight. Some nodes (pixels) are labeled as terminal nodes: *source* ( $s$ ) and *sink* ( $t$ ) [3]. Figure 4.12 shows a two-terminal graph on a  $3 \times 3$  image with two labels. Edges can be directed or undirected, the graph in the figure illustrates the case of directed edges, where the weights assigned to the edges differ depending on the direction, i.e. the weight of the edge between two arbitrary nodes ( $p, q$ ) may differ from the weight of the reverse edge ( $q, p$ ).

Two types of edges are connected to each (node) pixel in the image: n-links (neighborhood links) and t-links (terminal links). Two sets of pixels are labeled by the user as object ( $s$ ) or background ( $t$ ) to provide hard constraints for the segmentation. Each pixel  $p$  has two t-links  $\{p, s\}$  and  $\{p, t\}$  connecting it to each terminal. Each pair of neighboring pixels  $\{p, q\}$  is connected by an n-link. The weight assigned to an n-link corresponds to the similarity between two neighboring pixels. The weight assigned to a t-link corresponds to the similarity between an image pixel and the labeled pixels ( $s$  and  $t$ ). An  $s$ - $t$  cut is a subset of edges  $\mathcal{C} \subset \mathcal{E}$  which completely separate the source and sink terminals.

The labeled pixels (seeds) defined by the user represent a hard constraints for the segmentation, as those pixels are predefined as part of the object or the background.

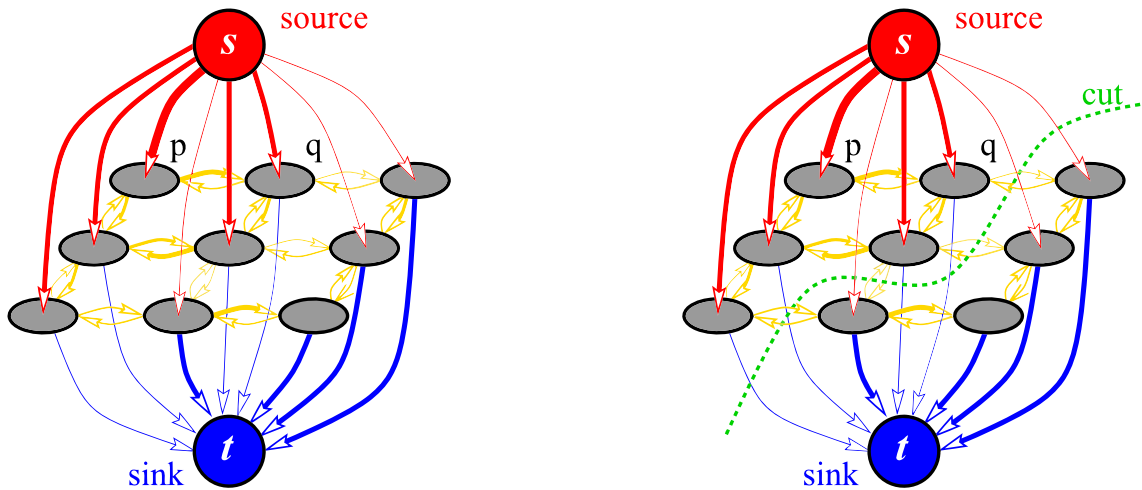


Figure 4.12: Illustration of a graph cut on  $3 \times 3$  image, thickness of the directed edges represent their weights. Two types of links: n-links between the neighboring pixels (yellow), t-links between the pixels and the source (red), and t-links between the pixels and the sink (blue). From Boykov et al. [3].

The rest of the pixels are automatically classified as object or background by computing a global minimum of a cost function among all segmentations satisfying the hard constraints. The cost function incorporates soft constraints: boundary and region information [3].

### 4.3.1 Segmentation Cost Function

Let  $P$  be an arbitrary set of pixels in a 2D (or 3D) grid and  $\mathcal{N}$  a set of all pairs  $\{p, q\}$  of neighboring pixels, 8-neighborhood or 26-neighborhood in cases of 2D or 3D respectively. Let  $A = (A_1, \dots, A_p, \dots, A_{|P|})$  be a binary vector, whose elements  $A_p$  mark the pixel  $p$  in  $P$  as *object* or *background*; i.e. vector  $A$  defines a segmentation. Then the cost function that imposes the region and boundary soft constraints can be defined as:

$$E(A) = \lambda \cdot R(A) + B(A) \quad (4.22)$$

where the regional term is

$$R(A) = \sum_{p \in P} R_p(A_p) \quad (4.23)$$

and the boundary term is

$$B(A) = \sum_{\{p,q\} \in N} B_{p,q} \cdot \delta_{A_p \neq A_q} \quad , \quad \delta_{A_p \neq A_q} = \begin{cases} 1 & A_p \neq A_q \\ 0 & A_p = A_q \end{cases} \quad (4.24)$$

The constant  $\lambda \geq 0$  in equation (4.22) defines the relative weight of the regional  $R(A)$  term versus the boundary term  $B(A)$ . The regional term corresponds to the probability that a certain pixel belongs to the object or the background. Following the model proposed by Boykov et al. [79], we used the seed pixels (hard constraints) to get histograms for *object* ( $\Pr(I|\mathcal{O})$ ) and *background* ( $\Pr(I|\mathcal{B})$ ) intensity distributions. Then, the regional term was calculated as the negative log-likelihoods:

$$\begin{aligned} R_p(\text{"obj"}) &= -\ln \Pr(I_p|\mathcal{O}) \\ R_p(\text{"bkg"}) &= -\ln \Pr(I_p|\mathcal{B}) \end{aligned} \quad (4.25)$$

For each neighboring pair pixels  $p$  and  $q$ , the boundary term  $B(A)$  varies according to the similarity or dissimilarity between the pixels. The value of  $B_{p,q}$  is large when the pixel intensities are similar and approaches zero when discontinuity occurs. Accordingly, we set the boundary term function to:

$$B(p, q) = F \cdot \exp\left(-\frac{(I_p - I_q)^2}{2\sigma^2}\right) \quad (4.26)$$

where  $F$  is a constant factor and  $\sigma$  serves as a similarity variance. When intensities are similar ( $|I_p - I_q| < \sigma$ ), the bond between the neighboring pixel is strong and the weight assigned to this edge is large. However, if pixels are very different ( $|I_p - I_q| > \sigma$ ), then the bond is weak and the weight assigned is small.

Table 4.1: Weights of all types of edges in the graph.

edge	weight (cost)	for
$\{p, q\}$	$B_{p,q}$	$\{p, q\} \in \mathcal{N}$
	$\lambda \cdot R_p(\text{“bkg”})$	$p \in P, p \notin \mathcal{O} \cup \mathcal{B}$
$\{p, s\}$	$K$	$p \in \mathcal{O}$
	$0$	$p \in \mathcal{B}$
	$\lambda \cdot R_p(\text{“obj”})$	$p \in P, p \notin \mathcal{O} \cup \mathcal{B}$
$\{p, t\}$	$0$	$p \in \mathcal{O}$
	$K$	$p \in \mathcal{B}$

Table 4.1 summarizes all the weights assigned to the graph, where  $K$  is a constant greater than the sum of all n-links costs. After defining the nodes, edges, and corresponding weights of the graph  $\mathcal{G}$ , the minimum cost cut  $\hat{\mathcal{C}}$  on the graph  $\mathcal{G}$  defines the segmentation boundary between the object and the background. The cost of a cut  $\mathcal{C} = \{s, t\}$  is defined as the sum of the costs of boundary edges  $(p, q)$ , where  $p \in s$  and  $q \in t$ . The minimum cut problem on a graph is to find a cut that has the minimum cost among all cuts.

The minimum s-t cut problem can be solved by finding a maximum flow from the source  $s$  to the sink  $t$ . We can think about the maximum flow as the maximum “amount of water” that can flow from the source to the sink and the graph edges as “pipes” with capacities equal to edge weights [3]. Solving for the maximum flow from  $s$  to  $t$  dividing the nodes into two segments is equivalent to solving for the minimum cut (minimum cost) [80]. We used an implementation of max-flow/min-cut algorithm provided by [3]<sup>4</sup>.

<sup>4</sup>The implementation is freely available for research purposes on <http://vision.csd.uwo.ca/code>. For more details about the max-flow/min-cut algorithm, please see Boykov et al. [3]

### 4.3.2 Segmentation Steps

After explaining the theory of using the graph cut method in image segmentation, we present our approach to segment tumors in US images using graph cut. Our implementation considered only 2D image segmentation; Chapter 6 illustrates how several 2D segmented tumors were used to obtain 3D information.

First step is to label one set of pixels as object and another as background. Normally these pixels are selected manually by brushing separate parts of the image before running the segmentation algorithm; however, automatic initialization can be done as described in Chapter 6. Figure 4.13 shows how the object and background nodes (hard constraints) were set in our implementation. The object (tumor) was labeled by a filled circle inside the tumor and the background (rest of the image) by a hollow disc around the tumor.



Figure 4.13: Initialization of the graph cut algorithm by selecting two sets of pixels: object (tumor) and background.

The edge weights were assigned according to table 4.1, with the constants as follows:  $K = 10000$ ,  $\lambda = 100$ ,  $F = 10$ , and  $\sigma = 1$ . After initializing the algorithm by setting

the hard constraints and the weights, the algorithm is practically ready to segment the image. However, this would segment the whole image including irrelevant parts far from the tumor. But we are interested only in the tumor, therefore we limited the area considered in the segmentation to a *narrowband* around the tumor. Figure 4.14 demonstrates the segmentation result without applying the *narrowband*.

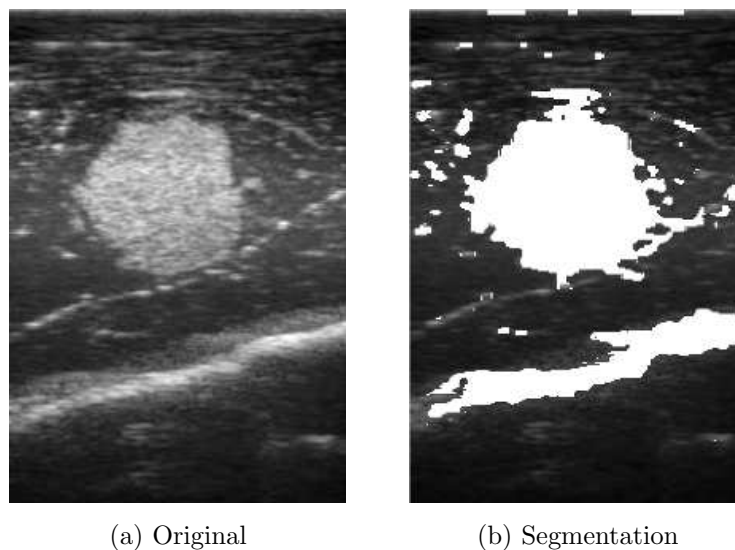


Figure 4.14: Segmentation result without limiting the segmentation algorithm to the area around the tumor. The segmented image shows that not only the tumor was segmented, but also some other irrelevant parts of the image.

Since the tumor boundary must lie between the *source* and the *sink*, the narrowband was defined as the area between the circle inside the tumor and the inner diameter of the disc around the tumor, Figure 4.13. By limiting the number of pixels (nodes) on which the graph cut algorithm is applied, we reduced the segmentation time and also avoided unwanted segmentation of image parts far from the object. Additionally, due to the noisy nature of the US images, morphological post-processing of the segmentation results was required. This was done by applying erosion filter to eat away small false segmentation around the tumor and then dilation filter to restore the original size of the main segmented object. Figure 4.15 shows the segmentation when only the *narrowband* was considered and the final segmentation after applying the morphological filters.

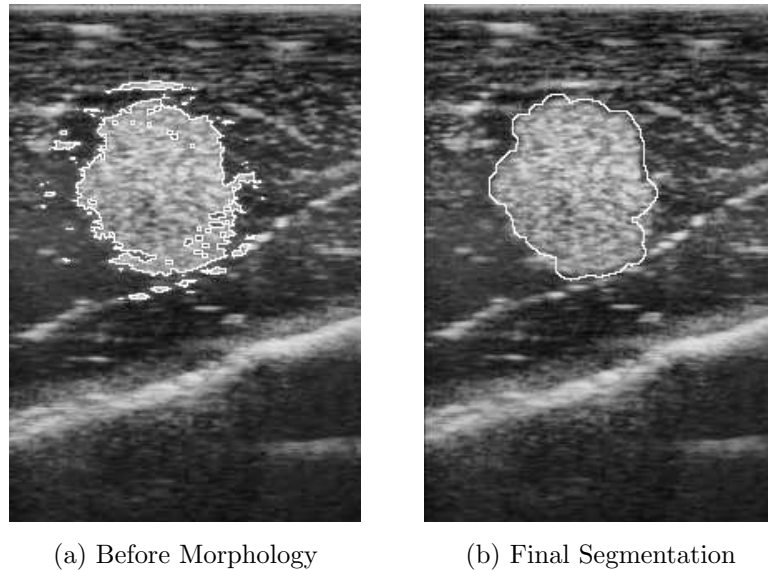


Figure 4.15: (a) Segmentation when the area considered in the segmentation was limited to the *narrowband* around the tumor. (b) Final segmentation after applying erosion and dilation morphological filters.

## 4.4 Segmentation Cases

The explained segmentation methods are used in the following chapters as part of tumor localization algorithms. The level set algorithm is performed on both 2D and 3D images; however, our graph cut implementation is limited to 2D images. Figure 4.16 demonstrates two segmentation examples of real liver tumors using the two illustrated methods.

## 4.5 Conclusion

We presented two methods for tumor segmentation on US images. Both methods were capable of dealing with the noisy nature of the US images. In case of the level set method, user interaction was required to provide an initial contour (seed point) inside the object. Afterwards, the initial contour evolved to match the tumor

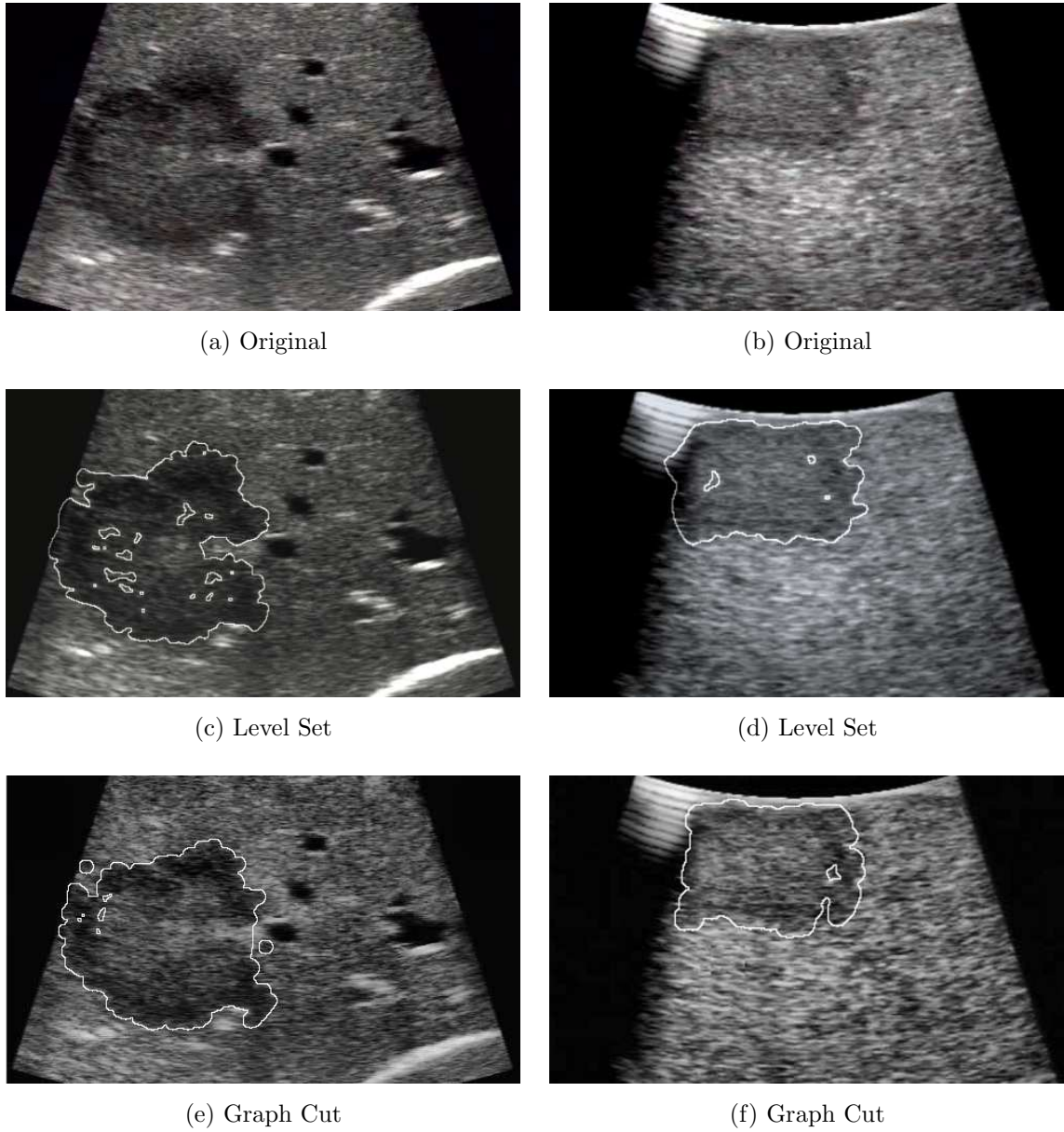


Figure 4.16: Segmentation results of real liver tumors using level set and graph cut algorithms.

## 4.5. CONCLUSION

---

boundaries. Also the graph cut method requires labeling parts of the image as object and background. Then a global minimum of a cost function is computed among all segmentations that separate the object and background labels. This chapter aimed to present the theory and steps involved in the segmentation process. In the next two chapters, these methods are used to segment tumors in tumor localization approaches.

# Chapter 5

## Local Registration

### 5.1 Introduction

In image guided interventions, additional information is obtained from imaging modalities and tracking systems. Based on this information, positions of the surgical tools and the organ anatomy are represented on the navigation screen to support the surgeon approaching targets. Therefore, it is essential for the model representing the organ on the navigation screen to reflect accurately the actual surgical situation. This is not easily achievable in a highly deformable organ such as the liver.

The liver is subjected to motions throughout the surgery, either periodic due to respiration or irregular due to surgical manipulation. Due to these motions, the position of the target tumor inside the liver changes during the operation. Hence, intraoperative update of the target position is necessary in navigated liver procedures. In section 2.6, several navigation approaches developed by other groups were presented. Most of them aimed to find a global solution which maps the preoperative liver model to the actual liver. The drawback of this process is that, it is complicated to repeat once the surgery starts, as it requires access to multiple regions of the liver. Also, whole liver mapping is typically computationally expensive and consequently very time consum-

ing. Moreover, it is very unlikely after registering the whole liver to achieve adequate navigation accuracy at arbitrary proximal targets in the liver. Especially as the liver anatomy is divided into lobes and segments [15].

On the other hand, the surgical workflow is local by default; the surgeon focuses on only one tumor at a time and then on another in case of multiple ones. Since the key information in the navigation procedure is the target tumor, we can focus on this target to reach a high navigation accuracy and then move to the next target. This is achieved by performing local registration considering only one tumor region at a time according to the surgical workflow. Another important aspect to consider is that the process of updating the target position should be repeatable, as changes in the target position usually are not predictable.

In this chapter we present a navigation approach based on tracked LUS and focused on the neighborhood of the tumor. As LUS is routinely used in laparoscopic liver procedures, the approach doesn't introduce major changes to the surgical work flow. The aim is to quickly compensate for tumor movements due to surgical manipulation, and subsequently, maintain high navigation accuracy in the region of interest containing the tumor throughout the procedure.

## 5.2 Methods

In Chapter 4, tumors were successfully segmented in reconstructed US volumes. As we know the position and orientation of every acquired US frame (Chapter 3), we also know the location of the segmented tumor in the reference (EM transmitter) coordinates. So basically we can navigate to the tumor centroid. But, segmenting the tumor in 3D takes substantial time to solve and requires user interaction to place an initial contour. Thus, repeating this process during the surgery to get the actual tumor position is impractical for the surgical workflow. However, we do not need to start segmentation of the tumor from scratch for each newly acquired volume, but instead use the segmented tumor as a priori knowledge.

The main idea of the proposed approach is to use the segmented tumor as a tumor model in a registration scheme. Hence, the time consuming segmentation is required only once at the beginning of the procedure. After that, quick registration is performed to update the navigation system with the actual tumor position. Figure 5.1 demonstrates the overall steps involved:

- LUS probe calibration
- Intraoperative volume reconstruction
- Tumor segmentation
- Tumor monitoring (US scan  $\Rightarrow$  registration)

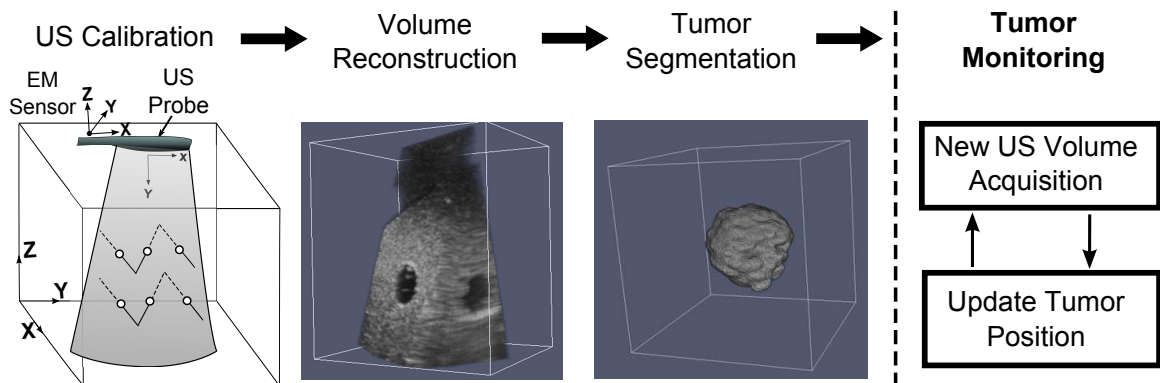


Figure 5.1: Steps involved in the approach. First step resembles the US calibration procedure (section 3.2), where an US image intersects the wires (white dots) inside the calibration phantom. Second, an US volume is reconstructed. Third, tumor is segmented and its position is determined. Those three steps are performed initially; afterwards, automatic monitoring of the tumor position is performed with each newly acquired US volume using the segmented tumor and its previous position as priori knowledge.

First of all, calibration of the US probe was performed (Chapter 3); this step is only necessary if there was no calibration done beforehand or the sensor position on the probe has been changed. Then an initial US volume was acquired, in which the tumor was segmented (Chapter 4) and its center of mass (centroid) was computed.

Afterwards, with every new scan of the tumor region, the tumor position is automatically determined in two steps:

- Local surface registration
- Tumor-based registration

### 5.2.1 Local Surface Registration

While scanning the tumor region with the US probe, the points along the transducer array are located on the liver surface. Accordingly, a line of surface points can be collected per frame acquisition. But we don't need all those points to perform a surface registration, so only three points corresponding to the beginning, mid, and end of the transducer array were recorded. By completing the US scan, we obtained a set of points representing the surface of the liver above the tumor region.

Point clouds from two consecutive scans (Figure 5.2) were used to perform a 6D rigid registration using an ICP method [78]. This iterative process involves matching the nearest neighbors from the two point sets, minimizing a mean square cost function, and estimating the transformation parameters.

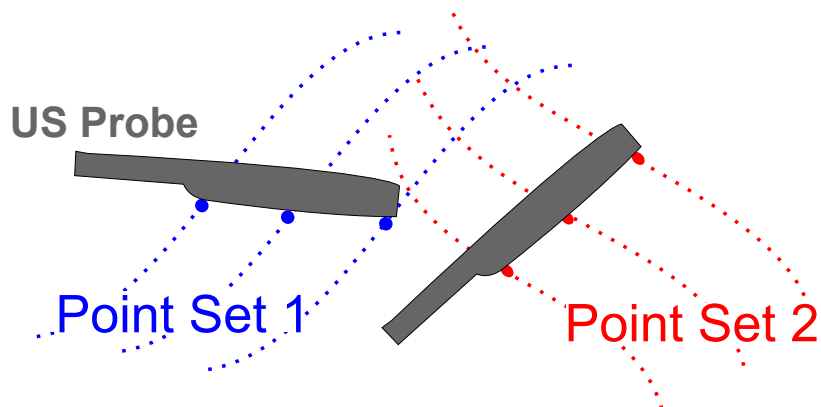


Figure 5.2: Illustration of the ICP registration algorithm between two sets of points. For each US frame acquisition, three points on the liver surface are collected. By completing the scan, these points form a set of points.

### 5.2.2 Tumor-based Registration

Although the surface registration was done locally for the tumor region and not for the whole liver, it is only using surface points, so the registration error can extrapolate to significant numbers at points located deeper in the tissue. Thus, surface registration is not enough to guarantee good registration accuracy at the target tumor. However, the surface registration brings the tumor model closer to the actual tumor. Following the ICP registration, another registration was performed using the tumor itself as the registration object.

At this point, the tumor model (segmented tumor) is mapped and located inside the newly acquired US volume in the neighborhood of the actual tumor. Since tumors are usually stiffer than the surrounding normal liver tissue [81], we assumed tumor rigidity and consequently the tumor shape didn't change. Hence, rigid registration was applied using the tumor model as a moving image to search in the neighborhood for the best match. Using image information from the segmented tumor and the US volume, we applied a mutual information (MI) registration metric with a gradient decent optimizer [72].

Optimization of registration metrics aim to maximize or minimize cost functions by iteratively evaluating the output value given a set of transformation parameters. Gradient descent optimizer searches in the parameters space so that the optimization follows the negative gradient of the cost function. It is the direction along which the cost function decreases most rapidly. If we want to maximize the cost function, the optimizer moves along the positive gradient direction. First, we set an initial step for the optimizer, this step is reduced by a factor once the gradient changes direction. Eventually, the optimizer finds the spatial transformation that maps the moving tumor model to the best match in the fixed US volume.

### Mutual Information Metric

Given two random variables (images), MI measures the average amount of information that first variable conveys about the other or vice versa [82]. MI registration metrics are based on probabilistic measures of image intensity values [83].

Let

$$H(A) = - \int P_A(a) \log P_A(a) da \quad (5.1)$$

be the entropy of random variable A,  $H(B)$  the entropy of random variable B and

$$H(A, B) = \int P_{AB}(a, b) \log P_{AB}(a, b) da db \quad (5.2)$$

be the joint entropy of A and B. If A and B are independent, then

$$P_{AB}(a, b) = P_A(a)P_B(b) \quad (5.3)$$

and

$$H(A, B) = H(A) + H(B). \quad (5.4)$$

However, if there is any dependency, then

$$H(A, B) < H(A) + H(B). \quad (5.5)$$

The difference is called mutual information :  $I(A, B)$

$$I(A, B) = H(A) + H(B) - H(A, B). \quad (5.6)$$

## 5.3 Experiments and Results

To evaluate the proposed approach, we conducted an ex-vivo experiment on a porcine liver. Fourteen pseudo-tumors were embedded into several pieces of the liver and their center of masses were set as navigation targets. We also assessed how accurate the tumor-based registration algorithm can estimate the tumor position by moving a target on a known trajectory and estimating its position.

### 5.3.1 Pseudo Tumors Preparation

The tumors were created by mixing 6 g agarose, 6 g cellulose, 14 ml glycerol, and a trace of color powder in 200 ml distilled water [84]. The mixture was then heated until having a homogeneous solution, then left to cool in room temperature. Just before the mixture solidified, while it was still viscous, approx. 4 ml ( $\approx 1$  cm tumor radius) of the mixture was injected into several locations in the tissue. Figure 5.3 shows how the tumor-mimic mixture looked like under US imaging.

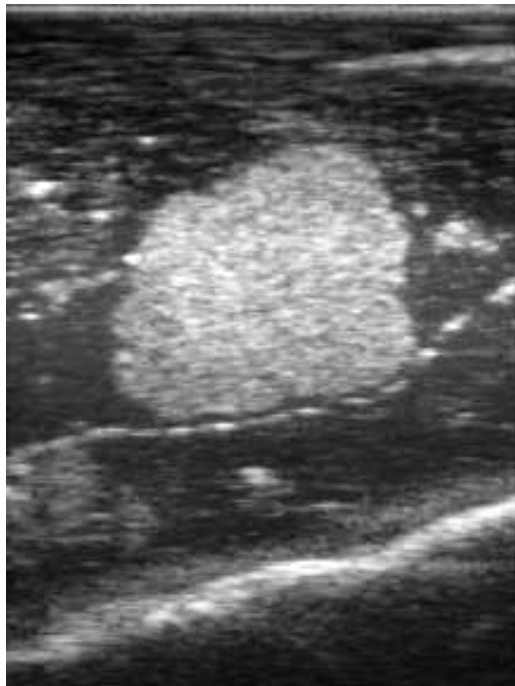


Figure 5.3: Ultrasound image showing one of the pseudo-tumors embedded in porcine liver tissue.

### 5.3.2 Experiment 1: Position Monitoring Validation

We immersed one of the pseudo-tumors in a container filled with water. A trace of cellulose and agarose was added to the water to create speckle background in US images. We fixed the tumor to a needle tip and mounted the needle to a robot. The tumor was moved by the robot to a starting position in the water. At this position we

### 5.3. EXPERIMENTS AND RESULTS

---

acquired US images of the tumor and reconstructed a volume. Then we moved the robot 5 mm to a next position and again acquired an US volume, Figure (5.4). The process was repeated 4 times, so we had 20 different start-end position combinations. For each combination, the tumor was segmented in one volume and registered to the other.

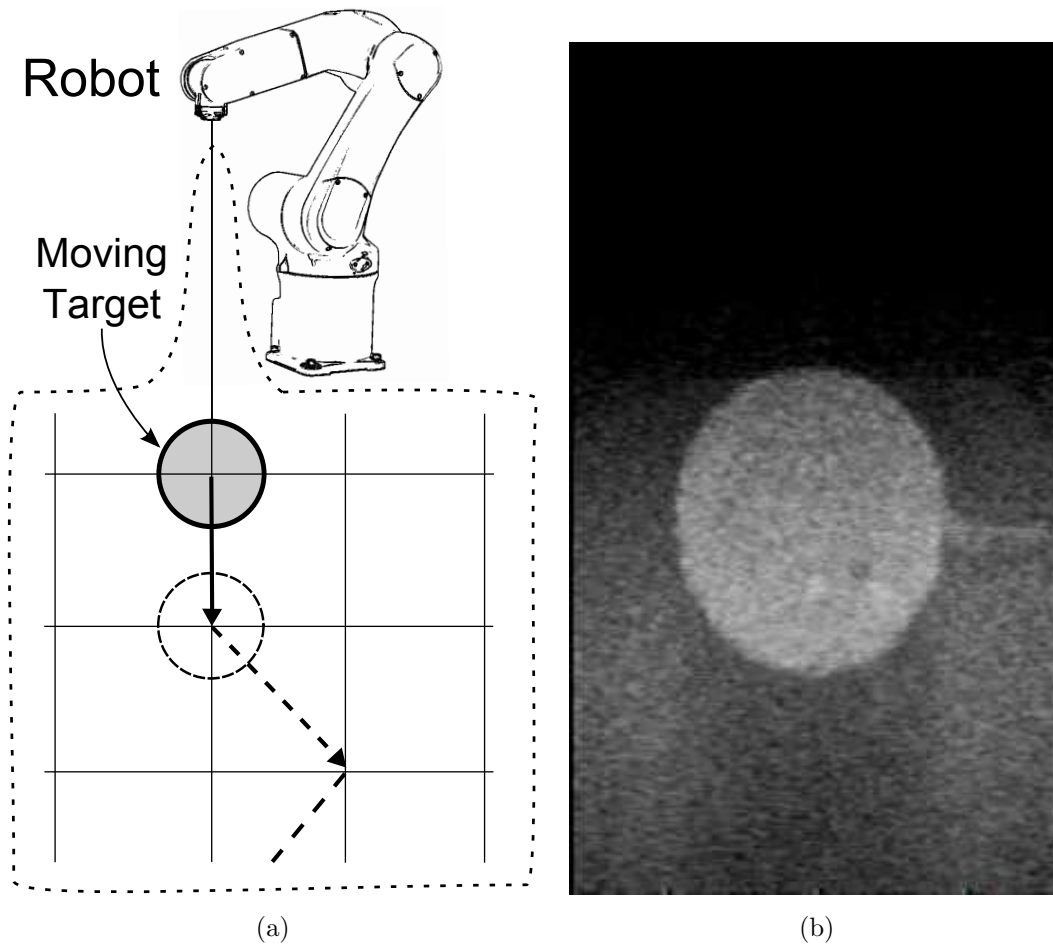


Figure 5.4: (a) Target tumor was moved inside a water tank on a known trajectory using a robot.  
(b) One of the US images acquired while scanning the target in the water tank.

The distance between the target centroids before and after the registration was calculated. Accuracy of the registration was estimated by comparing this distance to the known robot movement. The mean difference error for all the movements was  $0.4 \text{ mm} \pm 0.3 \text{ SD}$ .

### 5.3.3 Experiment 2: Needle Navigation

This experiment tests the approach in a scenario where the surgeon navigates an ablation needle to a tumor center and tries to compensate for possible tumor shift during the process. Tumors were injected at several positions into the liver tissue. For each tumor region, a 3D US volume was acquired and the tumor was segmented. The centroid of the tumor was calculated and set as the navigation target.

To guide the needle to the target, we built navigation software based on open source libraries [72,85]. The software enables 3D visualization of the needle trajectory and the needle tip relative to the target tumor. Figure 5.5 shows a snapshot of the software, where the needle (arrow head) was aligned towards the target point (trajectory to target distance  $< 1$  mm) and the needle tip was 18.4 mm distant from the target. The segmented tumor is visualized within the surrounding tissue, with the option to adjust tissue/tumor transparency to see the target. When the needle tip reaches a distance less than 1 mm from the tumor centroid, the target is considered reached.

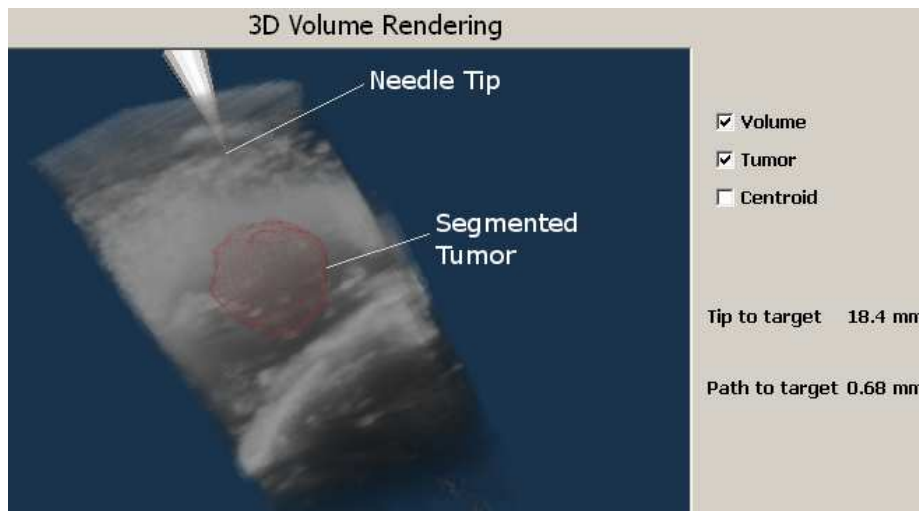


Figure 5.5: Snapshot of the navigation software showing rendered US volume and segmented tumor. It gives the option to show/hide or change the transparencies of the volume/tumor. Also it provides the distances from the needle tip to the tumor centroid and from the needle trajectory (path) to the tumor centroid.

### 5.3. EXPERIMENTS AND RESULTS

---

Before navigating the needle to the target, we needed to determine the spatial location of the needle tip in the world (transmitter) space and consequently its position relative to the target. A 6D sensor was fixed to the needle handle and a standard pivot calibration was performed [33]. The RMS error of the calibration was 0.53 mm. After that, the needle was oriented with the help of the navigation software towards the center of the tumor. Then, it was advanced till the software indicated that the target was reached ( $< 1$  mm).

However, needle insertion into the tissue causes a shift in the physical target position, hence, the needle tip was not at the actual center of the tumor. Moreover, we purposely moved and deformed the tissue to mimic a real surgical situation. To compensate for the tumor shift and update its position in the navigation software, a second US volume was acquired, Figure 5.6. Automatically, the registration algorithm found the actual tumor position in the new US volume. Accordingly, a new centroid was calculated and set as a new navigation target. Finally, the needle was navigated to the new target. We stopped after two iterations; nevertheless, the procedure can be repeated whenever tumor position update is necessary.

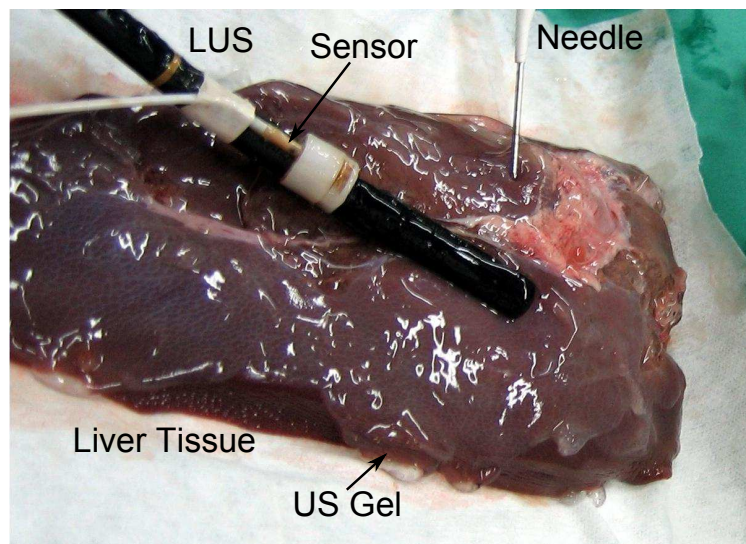


Figure 5.6: Photo taken during the experiment: tracked LUS probe scanning piece of porcine liver to acquire an US volume. Meanwhile, tracked needle was navigated towards an embedded pseudo-tumor.

To estimate the navigation error, the tumor was also segmented in the second US volume and centroids of the registered and segmented tumors were compared. Table 5.1 demonstrates the results of the surface registration using ICP. The results show the final registration parameters, the time elapsed, and how far the transformed tumor was from the actual target position (distance between centroids).

Table 5.1: Results of the local surface registration using ICP: translation, rotation, time required to update the tumor position, and distance between the transformed tumor position and the actual tumor position.

<b>T #</b>	Rotation (Deg.)			Translation (mm)			Time (s)	RMSE (mm)	Distance (mm)
	$R_x$	$R_y$	$R_z$	$T_x$	$T_y$	$T_z$			
<b>T1</b>	-1.36	2.36	0.92	4.2	5.6	7.5	0.02	1.23	3.3
<b>T2</b>	1.47	-2.22	-0.37	-6.5	-4.7	-0.6	0.16	4.38	4.4
<b>T3</b>	1.74	-1.78	-7.38	3.42	12.4	-4.2	0.08	2.05	3.6
<b>T4</b>	-17.97	-9.33	-7.62	-24.5	57.5	-35.3	0.15	1.56	4.3
<b>T5</b>	-20.21	-3.23	8.71	1.7	39.6	-34.0	0.25	2.78	2.5
<b>T6</b>	-19.10	-4.27	27.58	-16.2	-25.6	-23.9	0.05	1.54	3.3
<b>T7</b>	-5.61	2.49	-4.86	8.2	26.2	-7.7	0.15	2.76	5.3
<b>T8</b>	4.12	8.17	-4.54	18.8	21.0	7.6	0.05	4.41	8.1
<b>T9</b>	2.22	1.95	-4.65	5.0	-5.8	28.7	0.06	1.51	2.8
<b>T10</b>	-14.12	-10.18	-10.73	-8.6	30.6	1.6	0.03	1.34	3.3
<b>T11</b>	-25.65	-7.01	17.36	-8.4	24.5	-32.2	0.20	4.97	8.2
<b>T12</b>	-3.61	4.14	-15.82	5.3	17.2	-7.2	0.15	2.31	2.5
<b>T13</b>	-12.27	1.11	-19.99	11.1	53.2	3.0	0.18	2.08	1.5
<b>T14</b>	-18.58	14.34	17.32	21.9	47.2	33.0	0.03	2.44	2.4

Tables 5.2 demonstrate the results of the tumor-based registration using MI. The results show the distance each tumor was translated and the time needed to register the tumor. The last column in the table depicts the residual navigation error after compensating for the tumor shift.

## 5.4. DISCUSSION

---

Table 5.2: Results of the tumor-based registration using MI: translation, time required to update the tumor position, distance the tumor was shifted, and the residual navigation error after updating the tumor position.

<b>T #</b>	Translation (mm)			Time	Error
	$T_x$	$T_y$	$T_z$	(s)	(mm)
<b>T1</b>	0.4	-2.2	-2.3	0.59	0.2
<b>T2</b>	-0.4	-3.9	0.7	0.78	1.5
<b>T3</b>	-2.2	-0.6	1.7	0.67	1.2
<b>T4</b>	-1.0	-2.6	1.9	0.96	2.6
<b>T5</b>	0.5	-1.9	0.5	0.73	1.5
<b>T6</b>	0.2	2.2	1.7	0.82	0.5
<b>T7</b>	-0.1	5.8	0.4	0.75	0.7
<b>T8</b>	-0.2	-8.0	-0.4	0.78	1.4
<b>T9</b>	0.2	0.7	-1.7	0.51	1.5
<b>T10</b>	-0.7	-0.2	-1.3	0.52	2.5
<b>T11</b>	1.9	8.8	1.1	0.87	1.4
<b>T12</b>	0.5	-0.5	-0.3	0.41	2.3
<b>T13</b>	0.1	0.9	-1.0	0.47	0.2
<b>T14</b>	0.0	0.2	0.7	0.50	2.4

Table 5.3 presents the overall time required to update the tumor position and the distance between the original position of the tumor model and the position after the registration. It also compares the navigation error before and after applying the tumor-based registration.

## 5.4 Discussion

It is crucial while performing a navigated intervention to maintain high accuracy throughout the procedure. Particularly, accurate navigation must be maintained in

Table 5.3: Overall tumor shift recovered by the registration, total time required to update tumor position, error after ICP, and residual navigation error after the tumor-based registration.

<b>T #</b>	Distance	Time (s)	Error <sub>ICP</sub> (mm)	Error <sub>total</sub> (mm)
<b>T1</b>	2.3	0.61	3.3	0.2
<b>T2</b>	8.0	0.94	4.4	1.5
<b>T3</b>	1.5	0.75	3.6	1.2
<b>T4</b>	13.2	1.11	4.3	2.6
<b>T5</b>	33.4	0.98	2.5	1.5
<b>T6</b>	15.1	0.87	3.3	0.5
<b>T7</b>	12.4	0.90	5.3	0.7
<b>T8</b>	19.7	0.83	8.1	1.4
<b>T9</b>	25.2	0.57	2.8	1.5
<b>T10</b>	18.1	0.55	3.3	2.5
<b>T11</b>	26.3	1.07	8.2	1.4
<b>T12</b>	13.2	0.56	2.5	2.3
<b>T13</b>	14.2	0.63	1.5	0.2
<b>T14</b>	38.4	0.53	2.4	2.4

the region of interest containing the tumor. Therefore, the proposed technique was focused on the tumor neighborhood and utilized the tumor itself as the registration object. The technique is particularly useful when multiple tumors are approached subsequently, i.e. in a situation that further complicates whole liver registration.

The registration algorithm found the new tumor position in all the cases. The results show that tumor shift caused by needle insertion and tissue handling was up to 38 mm. Once a new US volume of the tumor region was acquired, the actual tumor position was found in an average time of 0.78 sec. After the ICP registration, the tumor model was closer to the actual tumor, nevertheless there was still an error margin up to 8.2 mm. As demonstrated in table 5.3, following the ICP with a tumor-based registration significantly increased the average accuracy to 1.2 mm in 12 of the

cases. In the other two cases, the MI algorithm almost didn't move the tumor model and the algorithm could not converge to a better tumor match in the neighborhood; thus the tumor-based registration didn't improve the ICP results in these cases and the accuracy remained around 2.4 mm.

In the experiments, we acquired only two US volumes per tumor, one before causing the tumor shift and one after. However, one of the advantages of this approach is that it is based on US, which is a widely available imaging modality and used routinely in liver interventions. Hence, whenever a tumor position update is necessary, the surgeon can simply scan the tumor region again and the new target position will be automatically identified. On the other hand, due to the limited field of view US imaging provides, compared to CT for instance, and the noisy nature of the images, visualization of only US images on the navigation screen might be insufficient for the whole navigation procedure. Therefore, this approach can be ideally used in combination with a preoperative-based model. Initial global registration (e.g. surface registration) can be applied to the model, and then the proposed method can at any time during the surgery further improve the navigation accuracy in the tumor region.

## 5.5 Conclusion

We demonstrated a navigation approach focused on a local region where the tumor is located. The technique does fast update of the tumor position by compensating for the tumor shift caused by surgical manipulation. The results indicate that maintaining an accurate navigation during laparoscopic liver procedures is feasible. The strength of this technique is that it can be performed intraoperatively, and it is repeatable throughout the operation. However, the algorithm requires acquisition of a dense US volume containing the whole tumor. In the next chapter we present an alternative approach which can estimate the tumor position using only a few US frames not necessarily covering the whole tumor.

# Chapter 6

## Sparse Segmentation

### 6.1 Introduction

The image localization approach described in the previous chapter is based on registration methods. It uses the output of an initial tumor segmentation to localize the tumor throughout the operation in subsequent US volumes. However, one of the limitations of this approach is that it requires dense scanning of the tumor region every time a tumor position update is needed. Otherwise, the registration algorithm wouldn't have enough image information about the tumor. In this chapter, we propose an alternative technique which doesn't require dense US volume in order to determine the actual tumor position during the surgery. This technique is mainly based on image segmentation; nevertheless, it provides a quick tumor position update using a few US images of the tumor.

### 6.2 Methods

The concept of this approach is to estimate the tumor position and shape using sparse information about the tumor. Similar to the local registration approach (Chapter 5),

an initial US volume containing the tumor is acquired at the beginning of the procedure. Then, the tumor was segmented in this volume to extract information about the tumor such as maximum diameter and distribution of pixel intensities. This information is used later on to automatically detect the tumor in subsequently acquired US images.

Whenever a tumor position update is necessary, an US scan of the tumor region is required. But, in contrast to the local registration approach, it is enough to swiftly scan the region of the tumor in a very natural manner as performed usually during the operation. This scan triggers a fully automated algorithm which determines the 3D position of the tumor.

During this scan, a few images are selected based on two factors: how much information the image contains (entropy), and its position given by the tracking system. Images are discarded if they don't contain enough information, which means they are unlikely to show the tumor. Also tracking information is used to ensure that the selected images are spatially distributed along the tumor and not representing the same slice or adjacent slices.

Steps of the algorithm are as follows:

- Frame selection
- Tumor detection
- Tumor segmentation
- Position estimation

### 6.2.1 Frame Selection

Once the tumor region was scanned using the tracked US probe, the position of each acquired frame relative to the previous one was determined. From 100 images acquired in approx. 5 sec, a number of frames were selected such that the distance between each two consecutive frames was between 1 and 5 mm. The lower threshold value

was set to ensure that the selected frames are not redundant and covering substantial part of the tumor. The upper threshold was used to avoid any inconsistency (jitter) in the selected frames which may result from irregular scanning.

### 6.2.2 Tumor Detection

Since the tumor was initially segmented in 3D, a slice through the tumor was taken as a reference image. For every selected frame, we calculated the entropy and compared it to the entropy of the reference image. If the difference between the two entropies was greater than 20%, the frame was excluded from the selected list. For the images which passed the entropy test, a template matching algorithm was applied to detect the tumor. The tumor in the reference image was used as a template in a template matching method based on normalized cross correlation (NCC) [86]. For every pixel in the image  $I(x_i, y_i)$ , a cross correlation score  $R$  was calculated by sliding the template tumor over the current US image and applying the following equation:

$$R(x_i, y_i) = \frac{\sum_{x_t, y_t} (T(x_t, y_t) - I(x_i + x_t, y_i + y_t))^2}{\sqrt{\sum_{x_t, y_t} T(x_t, y_t)^2 \cdot \sum_{x_t, y_t} I(x_i + x_t, y_i + y_t)^2}} \quad (6.1)$$

where  $T(x_t, y_t)$  represents a pixel in the template image. The pixel with the highest score determines the position where the overlaid template found the best match in the US image. In case of a perfect match, the correlation score would be 1.0. A threshold score of 0.95 was set for a successful tumor detection, accordingly images were excluded when the  $R$  value was less than the threshold.

### 6.2.3 Tumor Segmentation

The tumor location in the US image is now determined, also the *maximum diameter* and *mean intensity* of the tumor is known from the initial segmentation. Accordingly,

automatic initialization of the level set and graph cut segmentation methods described in Chapter 4 is possible.

The level set segmentation method was initialized by placing an initial contour centered at the point where the tumor is detected and with a diameter equals one third of the *maximum diameter*. The sigmoid filter parameter ( $\beta$ ) was set equal to the *mean intensity* value. Also the graph cut method was automatically initialized; the foreground region was defined as a circle inside the tumor, while the background was a hollow circle around the tumor (Figure 4.13). Then either of the segmentation methods was applied to segment the tumor.

Before accepting the segmentation result, another test was performed to compare the segmentation output to the initial segmentation. This check uses prior knowledge about the tumor vertical and horizontal diameters to detect incorrect segmentation, e.g. due to leakage. For each segmented tumor, the maximum vertical and horizontal diameters were automatically calculated. If any of the diameters was different by more than 25% compared to the reference diameters, the segmentation result was rejected. When five segmentation results of the tumor pass all the tests, the algorithm moves to the next step to determine the 3D tumor position.

### 6.2.4 Position Estimation

The contours of the segmented tumors are actually points on the surface of the tumor. Since the shape of the tumor is known from the initial whole tumor 3D segmentation, we can fit these contours to the whole tumor surface. This is done by applying a 6D rigid ICP registration that maps the tumor surface to the contours. To speed up the process, the surface of the tumor and the segmented contours were downsampled before running the ICP algorithm. Finally, the centroid of the registered tumor points was set as the updated tumor position.

## 6.3 Results

The data from the experiment in Chapter 5 were used to test the proposed algorithm. For each tumor we had two US acquisitions, one before causing a tumor movement and one after. The first acquisition was used as a reference, where the tumor was segmented to produce a 3D tumor model. This model was used in the ICP registration to estimate the tumor location. Also a 2D template image was obtained from this initial volume, which was used for the automatic tumor detection.

An arbitrary set of consecutive images (100 frames) from the second US scan was fed as an input to the algorithm. Then the steps explained in the methods section were applied in order. Both the level set and graph cut segmentation methods were tested separately. The frame selection step based on relative frame positions took less than 1 msec in all cases. Also the tumor detection step including the entropy check and the template matching took in average 0.015 sec.

For each successful tumor detection, the tumor was segmented and the result was accepted or rejected based on the tumor size. The algorithm stopped when five contours per tumor were obtained. Figures 6.3 and 6.2 show one of the segmented tumors on three different frames, using the graph cut and level set methods respectively. Figure 6.3 shows the surface points of the tumor registered to the segmented contours.

Tables 6.1 and 6.2 demonstrate the results. They show the average segmentation time per image and the time required to map the tumor model to the segmented contours using ICP. The tables also show the total time from frame selection till position estimation for each tumor. The error in the last column was calculated by comparing the estimated tumor centroid to the actual tumor centroid obtained from the experiment in the previous chapter.

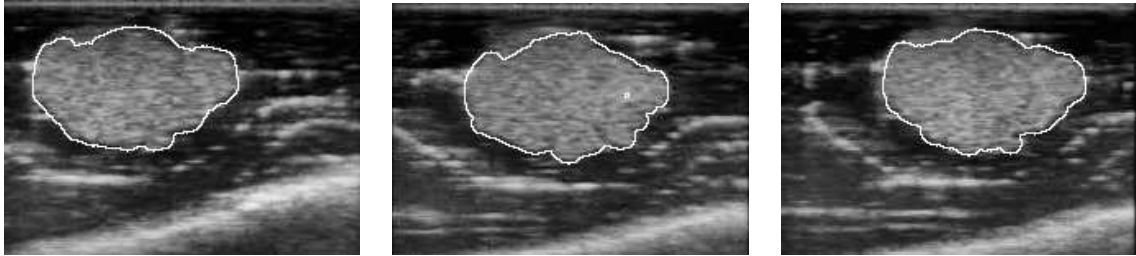


Figure 6.1: Tumor contours segmented using *graph cut* on three of the selected US frames.

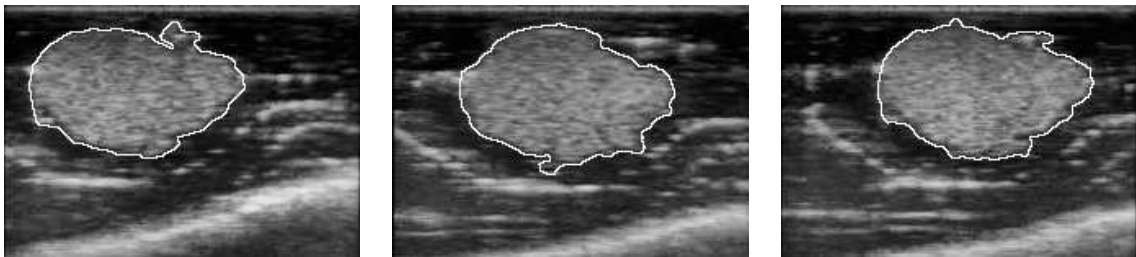


Figure 6.2: Tumor contours segmented using *level set* on three of the selected US frames.

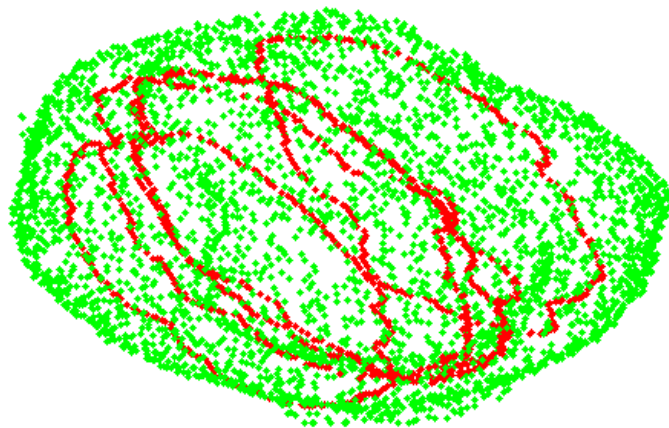


Figure 6.3: Tumor surface points (green) mapped to the segmented contours (red).

Table 6.1: Results of the sparse segmentation algorithm using the *graph cut* segmentation: average segmentation time per image, registration time using ICP, total time from frame selection till position estimation, and the error calculated as the distance between the estimated tumor centroid and the actual tumor centroid.

<b>T #</b>	Time/Image (s)	Time <sub>ICP</sub> (s)	Time <sub>total</sub> (s)	Error (mm)
<b>T1</b>	0.70	0.56	5.43	2.1
<b>T2</b>	0.73	0.76	5.80	3.0
<b>T3</b>	0.79	0.89	5.09	1.2
<b>T4</b>	0.62	0.61	6.47	2.4
<b>T5</b>	0.75	0.71	6.55	2.4
<b>T6</b>	0.59	0.81	5.51	1.6
<b>T7</b>	0.72	0.57	5.36	2.1
<b>T8</b>	0.73	0.62	5.88	2.4
<b>T9</b>	0.56	0.46	4.72	1.0
<b>T10</b>	0.64	0.98	5.68	0.7
<b>T11</b>	0.57	0.59	7.46	2.4
<b>T12</b>	0.58	1.14	5.32	3.0
<b>T13</b>	0.59	0.84	5.65	0.7
<b>T14</b>	0.57	0.90	5.44	2.6

## 6.4 Discussion

The goal of the proposed approach is to estimate the tumor position using sparse tumor surface. The sparse surface was built by performing automated tumor segmentation. A few frames were automatically selected based on their positions and entropies. In these frames, the tumor was detected and segmented. The template matching threshold was set to a high value (0.95) to reduce false tumor detections. Correct segmentation of the tumor is the core of this approach; hence, prior knowledge about the tumor obtained from an initial segmentation was used to decide whether to accept or reject the segmentation result.

## 6.4. DISCUSSION

---

Table 6.2: Results of the sparse segmentation algorithm using the *level set* segmentation: average level set segmentation time per image, registration time using ICP, total time from frame selection till position estimation, and the error calculated as the distance between the estimated tumor centroid and the actual tumor centroid.

<b>T #</b>	Time/Image (s)	Time <sub>ICP</sub> (s)	Time <sub>total</sub> (s)	Error (mm)
<b>T1</b>	0.55	0.59	5.30	1.5
<b>T2</b>	0.52	0.82	5.74	2.3
<b>T3</b>	0.65	1.34	5.37	2.1
<b>T4</b>	0.50	0.67	6.37	3.3
<b>T5</b>	0.51	0.68	3.68	2.2
<b>T6</b>	0.47	0.79	3.60	1.2
<b>T7</b>	0.51	0.81	3.63	2.3
<b>T8</b>	0.50	0.56	3.38	2.8
<b>T9</b>	0.44	0.48	3.99	0.7
<b>T10</b>	0.47	0.90	3.52	1.0
<b>T11</b>	0.45	0.89	6.62	2.4
<b>T12</b>	0.47	0.62	3.20	3.0
<b>T13</b>	0.51	0.64	3.57	1.9
<b>T14</b>	0.48	1.00	3.84	3.0

Although graph cut optimization is generally faster than level set optimization, the foreground/background pixel assignments in our implementation made the time required to perform a graph cut segmentation slightly higher than that required by the level set method. Nevertheless, both methods segmented the tumor in an average time of 0.65 sec for the graph cut and 0.5 sec for the level set. The segmented contours were not identical using the two methods. However, the differences are mostly due to the degree of border smoothness. Hence, it didn't significantly affect the estimation of the tumor position.

As an alternative to the previous tumor localization method in Chapter 5, this method is more suitable for the hectic surgical workflow, as it doesn't need scanning the

tumor region in a special fashion. Also, volume reconstruction is not required, and consequently the total time needed to update the tumor position is less. Although the algorithm uses only a few surface contours to estimate the 3D position of the tumor, the accuracy of the approach is comparable to the one obtained previously by using registration based on the whole tumor. The error using the graph cut segmentation methods was  $2.0 \pm 0.8$  mm, mean error  $\pm$ SD. The error using the level set segmentation methods was also in the same range:  $2.1 \pm 0.8$  mm. Both the level set and the graph cut algorithms took in average 0.57 sec to segment the tumor in each frame. The total time to localize the tumor was  $5.74 \pm 0.67$  and  $4.42 \pm 1.15$  using the graph cut and level set methods respectively. This method is at least 5 times faster than the previous method which required a longer US scan followed by a volume reconstruction.

## 6.5 Conclusion

The approach presented in this chapter aimed, similar to the local registration approach, to compensate for the tumor shift during the surgery. This approach, however, considered practical issues concerning the surgical workflow. One of these issues is that the surgeon might not be able to cover the whole tumor volume in one US scan. Therefore, we considered an approach which automatically estimates the tumor position given a few number of US frames showing the tumor. Also the proposed algorithm doesn't need any special considerations while scanning the tumor region, unlike the local registration technique which requires dense scanning of the tumor region. The results indicate that the algorithm can quickly compensate for tumor movements during the surgery with an accuracy comparable to the local registration approach.



# Chapter 7

## Discussion and Outlook

Technological developments in the fields of tracking and intraoperative imaging in combination with the availability of high computational power have led to the recent advance in image guided interventions. While commercial systems are available for surgical domains such as orthopedics, ear, nose, and throat (ENT), and neurosurgery, clinical practice of navigation on soft organs such as the liver is still limited. This is directly attributed to the deformability and mobility of the organ during the surgery.

Different factors cause tumor shift during minimally invasive interventions, including surgical manipulation, respiration, and heartbeat. Also tumor shift due to pneumoperitoneum in laparoscopic surgeries was reported by [8] as high as 28 mm. Liver surface registration after gas insufflations can significantly reduce this error [57]. Clifford et al. [9] reviewed nine publications about liver movement due to respiration. All studies agree that the most significant motion is observed in cranio-caudal direction, with translation ranging from 10 to 26 mm. These studies, however, didn't take into account that mobilization of the liver, which is usually done at the beginning of the surgery, may significantly decrease any effect of the respiration on the liver. Generally, the periodic motion due to respiration can be modeled and recovered [11,12,87]. Another approach to avoid the effect of respiratory motion is gating, which assumes

that the liver periodically reoccupies the same position in the respiratory cycle [88]. The other involuntary movement that may affect the liver is the heartbeat, it was studied by Kolen et al. [10] and found to be cyclic with a mean liver displacement below 1 mm.

Our experiments were focused on non-periodic intraoperative liver motions which can be caused by surgical manipulation and movement of the patient. Several preoperative-based and intraoperative-based systems [1, 45, 55, 57, 64, 65] have reported anatomical shift during the surgery as a serious problem affecting the navigation accuracy. Surgical navigation techniques can be evaluated based on several criteria, among them:

- Intraoperative navigation accuracy
- Time required to estimate target changes
- Visualization type and field of view

## 7.1 Navigation Accuracy

For liver procedures, it is challenging to develop image guided systems that provide the same accuracy of systems designed for bony or bone-encapsulated parts of the body. However, an accuracy of 3-5 mm is considered sufficient for abdominal interventions [32]. The overall system accuracy is affected by different components, including tracking system distortion [1], instrument and ultrasound calibration errors, and above all the registration error. We focus here on the registration error, as it is usually the main source of error, assuming the others are constants.

Penney et al. [58] generated vessel probability images from MRI and ultrasound images using training datasets and performed intensity-based rigid registration. For each ultrasound frame, the MRI probability volume was resliced according to the frame orientation, then an NCC similarity measure was applied to solve for the 3D translation parameters. Registration results were compared to a reference ICP-based

manual registration. The residual error in the reference registration was between 2.7 - 3.5 mm. By setting the points used in the reference registration as targets, the average target registration error (TRE) obtained after applying the NCC-based registration was 3.6 mm. Since no surgical interventions was necessary, they tested the algorithm on data of volunteers and patients.

Another interesting approach was proposed by Wein et al. [59,60], they developed a method to simulate ultrasound from CT images, then tested rigid and semi-affine registrations using a modified NCC similarity measure. The technique was evaluated in a study involving 25 patients with lesions in liver and kidney. They reported that *automatic* registration succeeded in 76% of the cases. Corresponding target points (1-5 points) were set, mostly lesion centers. The resulting TRE was 9.0 and 8.1 mm for the rigid and affine registrations respectively. Non-rigid registration was investigated by [2, 61, 62]. Their algorithms utilized vessel information to register preoperative data; consequently, only vessels were deformed and used to evaluate the accuracy. In [2], registration error was estimated as the mean square distance (MSD) between corresponding points on center lines of portal and hepatic veins. For three open surgery cases, the mean error was 3.7 mm  $\pm$ 4.3 SD.

A percutaneous needle insertion approach was presented by Maier-Hein et al. [89]. Optically tracked navigation aids (needles with markers) were placed adjacent to the tumor to continuously estimate the position of the target and update a preoperative CT model. Then post-procedural CT was performed to calculate the error as the distance between the needle tip and the tumor centroid in the images. The reported mean navigation error is 3.5  $\pm$ 1.1 mm. In comparison to their results, the mean errors using our approaches, also calculated based on tumor centroids, were 1.4 mm  $\pm$ 0.8 and 2.1  $\pm$ 0.8. Also other groups [90–92] investigated different techniques to perform needle navigation under CT guidance and reported less accurate navigation.

It is difficult to directly compare accuracies delivered by different approaches because the used intraoperative imaging modality can be different and the way each error is estimated is usually different. Some methods consider a global solution to register

the whole or big part of the liver. In terms of accuracy, based on solutions currently available, global registration may lead to inaccurate registration at points where accuracy is desired for an optimal treatment. Hence, having a local registration focused on the tumor region provides more accurate navigation. However, orientation can be less accurate because the area considered in the surface registration is relatively small and tumor shape can be spherical.

## 7.2 Speed

Another important aspect for intraoperative navigation is how quick the system can update the target according to the actual situation. This is usually proportional to the complexity of the registration algorithm and the need for intraoperative user interaction, for example to set corresponding landmarks. Most of the published literature didn't consider a quick solution a requirement, but a few reported the time their algorithms took. Wein et al. [11] stated that the time required to set landmarks was around 10 min per patient, while their automated intensity-based registration took less than 40 sec. The same range of time was required to set landmarks in [2], and the non-rigid landmark-intensity-based registration took approximately 10 min. The method in [61] also used initial landmark-based registration, however they reported that the non-rigid registration afterwards converged to a stable solution, no error estimation is given, in less than 5 sec.

The initial steps in the proposed solutions are ultrasound volume reconstruction and 3D tumor segmentation. Scanning the tumor region with the ultrasound probe took 20 sec, and the reconstruction of the volume took  $18 \pm 2$  sec. The time for the 3D tumor segmentation varied with the tumor size and was up to 1 min. In case of the “*local registration*” approach, a new volume reconstruction is needed every time a tumor position update is required (18 sec), then the tumor was registered in approx. 1 sec. The “*sparse segmentation*” approach neither requires a new ultrasound scan covering the whole tumor nor volume reconstruction, thus it was faster and estimated the new

position of the tumor in a total time of 5 sec in average. A real time estimation of the target position was reported by Maier-Hein et al. [89], however the technique is based on optically tracked fiducial needles, which can be only applied in percutaneous ablation procedures.

## 7.3 Visualization

Visualization was considered mainly by the research groups worked on developing a complete system for liver interventions. The image quality and the large field of view provided by CT and MRI make them superior to ultrasound when it comes to visualization. That is the main reason why most of the systems use preoperative CT/MRI data to create a liver model [44,47,57,93]. The second reason is that the time (days) between image acquisition and the surgery allows for accurate identification and segmentation of tumors and main vessels, usually this process is done interactively via semi-automated methods [94].

However, the main problem remains; the preoperative model must be modified intraoperatively according to the actual anatomy. Therefore, some groups developed their visualization based directly on intraoperative 3D ultrasound [63–65]. Integration (fusion) of 3D ultrasound with preoperative images can help interpreting the position of the ultrasound volume within the larger anatomy. One of the limitations of our approach is that it segments only the tumor. Ideally the navigation screen should not only visualize target tumors, but also important structures to be avoided, like main blood vessels. Therefore, it is important to combine our ultrasound-based navigation, which can quickly provide updated information that the surgeon relies on during the surgery, with a preoperative model to give larger field of view and better understanding of the anatomy.



## Part II

# Ablation Assessment



# Chapter 8

## Image-Guided Tumor Ablation

### 8.1 Introduction

Ablation refers to minimally invasive therapeutic procedures that destroy liver tumors without removing them. These techniques are usually performed for patients with no more than a few small tumors or when surgery is not a good option because of poor patient's health or reduced liver function . Although ablation is considered as a second option after surgery, it can still be very helpful in some case such as patients waiting for a liver transplant [15].

Several ablation techniques are available, including radiofrequency ablation (RFA), microwave ablation, high-intensity focused ultrasound (HIFU), laser-induced interstitial thermotherapy (LITT), percutaneous ethanol injection, and cryoablation. We concentrate in this work on RFA as it is currently the most commonly used ablative therapy [95].

RFA is performed under image guidance either percutaneously or in a laparoscopic intervention. During the treatment, high frequency alternating current is delivered through a probe with an active tip consisting of multiple prongs forming an umbrella-like shape when deployed; this helps to cover the whole tumor region. The alternating

current generates heat which turns cancer tissue into dead tissue, which is gradually replaced by fibrosis and scar tissue [15].

The ablation procedure involves five steps:

- **Planning:** imaging techniques are used to determine tumor size, shape, and whether the tumor is adjacent to critical structures or blood vessels.
- **Targeting:** placement of the ablation probe into the target tumor under imaging guidance. The aim of the targeting is to accurately guide the probe tip to the center of the tumor.
- **Monitoring:** visualization of the ablation effect on the tissue during the procedure. Tissue changes are reflected in the images and subsequently give a realtime feedback to the surgeon.
- **Controlling:** based on the information obtained during the monitoring, the operator can control the procedure. In RFA, this can be probe repositioning, temperature tuning, or even termination of the procedure in critical situations.
- **Assessment:** after the procedure, images are acquired to evaluate the efficiency of the treatment.

Among these steps, tumor targeting and monitoring are the most crucial for a successful RFA procedure. Particularly while performing an ablation in the liver, the high deformability of the organ presents a challenge for accurate probe placement in the target tumor. In addition to image-based guidance while targeting the tumor, navigation techniques were investigated to guide the probe accurately to the volumetric tumor center. Techniques for accurate tumor targeting were covered in Part I.

Supposing that the needle was successfully inserted accurately into the tumor, feedback and monitoring of the procedure plays the most important role in determining the efficiency of the therapy. This is not a simple task, especially when the same ablation zone can appear differently depending on the used monitoring technique.

## 8.2 Ablation Monitoring

Monitoring the ablation process is essential in order to determine how well the tumor is being covered by the ablation zone. At the same time, it helps to insure that vital normal structures are not affected during the procedure. Inaccurate visualization of the necrosis zone can cause incomplete ablation and subsequently tumor recurrence. Studies show that, local recurrence rates are up to 55% after RFA therapy [14, 96–99]. This emphasizes the urgent need for an ablation monitoring technique that can accurately distinguish between necrotic and non-necrotic tissue. That enables the surgeon to decide whether further ablation is required or the tumor is wholly burned.

Different imaging techniques can be used to visualize tissue changes during ablation procedures. Some are handy, portable, fast, and inexpensive such as US-based techniques. Others are more sensitive to thermal changes in the tissue and present the ablation zone more accurately such as MRI [100]. But the latter techniques are expensive and not easy to integrate in the operating room, therefore they are not as practical as US in ablation monitoring. Currently, B-mode US is the conventional intraoperative imaging modality for RFA monitoring [101]. But the zone of necrosis is not easily visualized in B-mode due to tissue vaporization and micro-bubbles formation. This produces a hyperechoic region which doesn't accurately represent the coagulated region (Figure 8.1) and becomes over time isoechoic [96]. This causes uncertainty in determining the extent of the ablation procedure using B-mode US [21].

In addition to conventional B-mode US, several techniques based on US have been recently investigated. These include temperature estimation by applying a cross-correlation algorithm to radio frequency (RF) US echo signals acquired at discrete time intervals during the ablation [14]. This method utilizes that changes in tissue temperature cause changes in the speed of sound and consequently the echo arrival time. Other methods monitor tissue elasticity changes before and after applying a small amount of compression [4, 96, 102]. These methods are based on the fact that

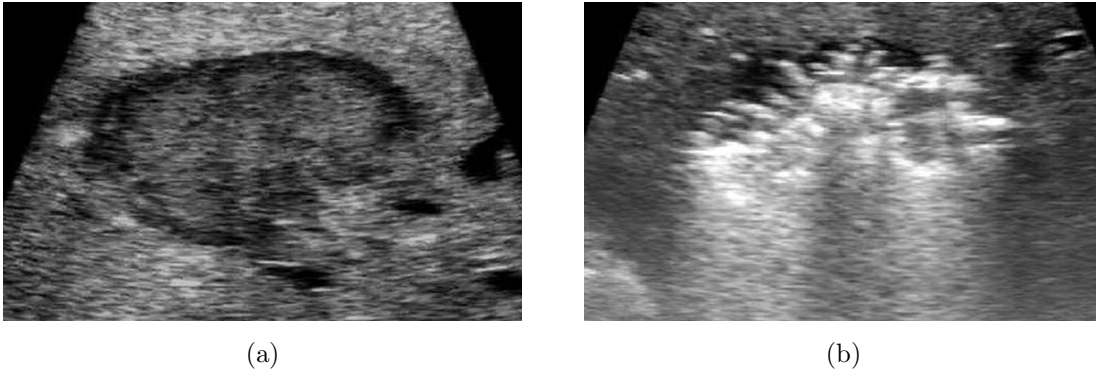


Figure 8.1: Radiofrequency tumor ablation causes vaporization in the tissue.

the stiffness of the ablated tissue increases after the ablation. US-based elastography is a promising technique to visualize ablated lesions that are barely visible with conventional US.

### 8.2.1 Elastography

Pathological changes are usually correlated with changes in tissue stiffness. The standard diagnostic palpation is used routinely to sense tissue stiffness and detect any abnormalities, which may indicate tumor existence. Also mechanical properties of ablated tissue are different from normal tissue. As a result of tissue heating and protein denaturation during the ablation procedure, the ablated zone becomes stiffer than the surrounding normal tissue [103]. Hence, imaging tissue elasticity, or a related parameter such as local tissue strain, is an emerging medical imaging method used for tumor detection and ablation monitoring.

Elasticity imaging visualizes the mechanical properties of the tissue as a response to an external mechanical stimulus. Detection of internal tissue motions due to this stimulus can be done using US, MRI, or other imaging modalities. In the ultrasound-based elasticity imaging, the probe is used to apply a quasi-static compression to the tissue, and the resulting strain is estimated. This method was first introduced in 1991 by Ophir et al. [104] and known as “*elastography*”. Another approach is to

stimulate the tissue by applying low frequency ( $< 1\text{kHz}$ ) vibration and capture the tissue response by ultrasonic or audible acoustic means [105, 106].

Elastography is based on measuring the time shift differences between congruent segments in an US A-line pair. First a set of radiofrequency echo signals is acquired of a certain region of interest containing a lesion. Then the US probe is pressed to compress the tissue along the axial direction by a small amount (1% of the total tissue depth) and a second set of echo signals is acquired. The pre and post-compression signals are then subdivided into small temporal windows. The difference in echo arrival time between corresponding segments is compared using one of the time-delay estimation techniques such as cross-correlation. Assuming a constant speed of sound, the displacement is obtained and the local longitudinal strain is estimated as the gradient of the displacement, Figure 8.2 and 8.3. The main assumption in elastography is that speckle motion adequately correlates with the underlying tissue motion for small uniaxial compressions. This holds as long as the distributions of the scatterers before and after compression remain highly correlated [105], i.e. small tissue deformations.

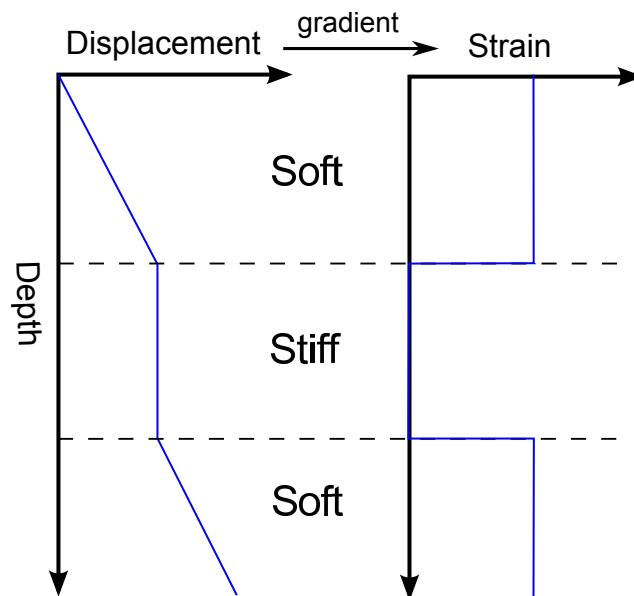


Figure 8.2: Displacement and strain caused by a constant pressure applied to a tissue with different stiffness layers.

### 8.3. ABLATION CORRELATION

---

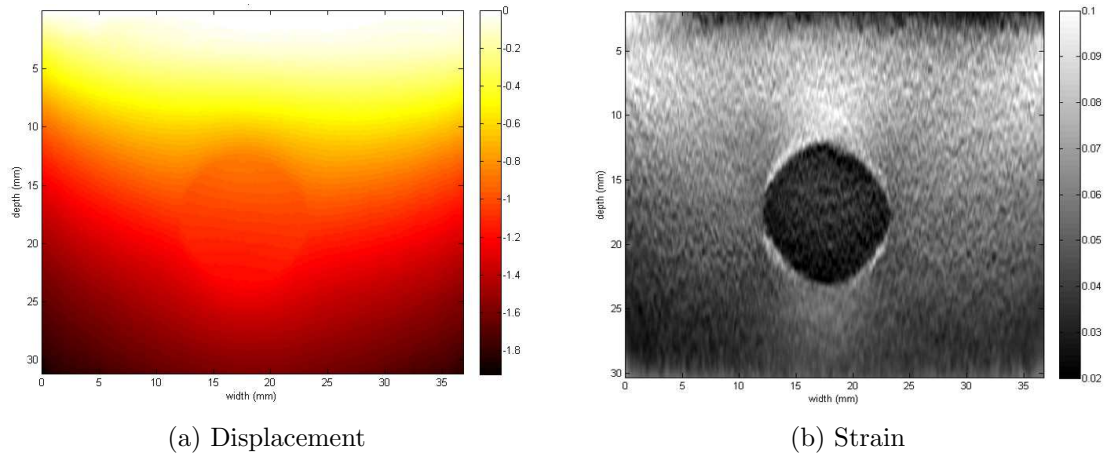


Figure 8.3: Displacement and strain images of a phantom containing a sphere made of stiffer material to mimic a tumor (Rivaz et al. [4]).

Quality of the strain images is highly dependent on how the compression is generated. Probe compression against the tissue should be in the axial direction. Any lateral or out-of-plane motions can deteriorate the quality of the images. Therefore, robot-assisted elastography produces better quality images compared to user-dependent freehand procedures [107]. This is the main reason why elastography is not yet widely used in clinical routines. A recent approach to improve the quality of freehand elastography is to track the US probe and use only image pairs which meet the optimum compression criteria to produce strain images [108]. However, 3D strain imaging with a reasonable image quality hasn't been yet achieved.

## 8.3 Ablation Correlation

Conventional US, MRI, and other promising techniques such as elastography provide valuable feedback to the surgeon during and after the ablation; however, it is still necessary to know the correlation between the actual necrosis and the lesion appearance on the images. It is very important that the used imaging modality can reflect the actual cellular damage. Usually, intraoperative ablation monitoring is done using

US as a handy, safe, widely available modality. Moreover, it is well integrated into minimally invasive procedures. Other imaging modalities such as CT or MRI can be used in postoperative control and follow up. However, imaging modalities are based on different physical concepts, consequently the same lesion can appear differently on different images.

Currently, MRI is the only modality with well validated techniques for real time temperature monitoring [109]. Although new monitoring modalities such as US elastography showed promising results to detect the ablated lesion [4, 96, 102], the actual relation between strain images and actual necroses is not clear. Relating actual necroses to lesions on the images will lead to better understanding of the images and help to promote the use of new monitoring techniques such as US elasticity.

## 8.4 Conclusion

Ablation procedures involve several steps, the most crucial among them are tumor targeting and monitoring of the process. These two steps play a major role in determining the efficiency of the procedure. The targeting problem was covered previously in Part I. In this chapter we focused on the ablation monitoring techniques to image the ablation procedure. This raised the question if the lesion appearance on the images reflects the actual necrosis and how it may vary depending on the imaging modality. Therefore, ablation correlation between different modalities and the actual necrosis is a necessity. Next two chapters address this topic, where we present approaches for multimodal ablation correlation.



# Chapter 9

## Ex-Vivo Ablation Correlation

### 9.1 Introduction

The previous chapter highlighted the importance of lesion monitoring during RFA. The question now is that if the lesion appearance on the images during the monitoring reflects the real necrosis. To investigate this point, correlation between the lesions on the images and the actual necrosis is required. The aim of the correlation is to enable direct comparison of images from different modalities used in RFA monitoring to a ground truth. This ground truth can be obtained by slicing through the actual tissue. However, it is necessary to match this particular slice to the corresponding slice in the acquired images.

In the standard slice matching method, first the tissue is scanned with the imaging modality and an image volume is obtained. Then, the ablated lesion is sliced at certain intervals (5 mm). These slices are manually matched to the corresponding ones in the acquired image volumes [110–112]. However, thin slicing is not achievable in all kind of tissues, especially in case of liver tissue. Additionally, slice matching is usually done by comparing the actual lesion size, measured on the slice, to the lesion size measured on the image. But the size of the lesion is exactly the questionable

point: do lesions appear the same on different imaging modalities or is the lesion size over- resp. underestimated by one modality?

We present a platform for ablation correlation which enables algorithmic mapping of the slices between different modalities. A phantom was designed to enable accurate pose estimation based on the phantom geometry. Regardless of the lesion shape and size on different modalities, only the phantom information was taken into account in the slice mapping process. This eliminated any subjective influence in the procedure.

## 9.2 Methods

### 9.2.1 Phantom Construction

To compare ablation outcomes on different imaging modalities to actual necroses, a phantom was so constructed that its features were visible with the naked eye as well as with the imaging modalities. Gelatin models were built containing a section of bovine liver in which a 5-10 mm lesion was created using RFA. The tissue within the gelatin was surrounded by four fiducials made of agarose such that each side view of the phantom had a “*Z-Shape*” geometry.

The model was constructed in the following fashion: first, a 10% porcine gelatin, 1% cellulose and 3% glycerol mixture was prepared at 95°C. This mixture was cooled down to 35°C and then poured in a plastic container. After this, an acrylic glass model, Figure 9.1 and 9.2, was placed in the gelatin mixture to create a negative space for the fiducials footprint. Just before congealing of the gelatin, an approximately  $4 \times 4 \times 4$  cm section of fresh bovine liver was submerged in the gelatin within the boundary of the fiducials.



Figure 9.1: 3D model of the acrylic glass mold which was used to create a fiducial footprint in the gelatin mixture.

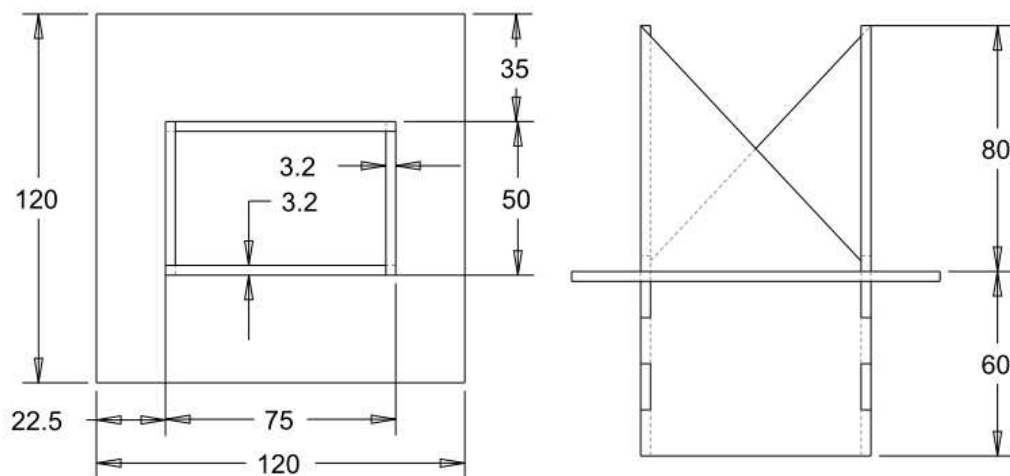


Figure 9.2: Dimensions of the acrylic glass model used to create the fiducials in the gelatin phantom.

After this, the containers were placed in a refrigerator over night to allow for complete solidification of the gelatin. The next day, the acrylic glass model was removed, thus creating four triangle shaped cavities around the piece of liver. These cavities were

## 9.2. METHODS

---

filled with a mixture of 1% agarose and 1% methylene blue dye. At last, lesions were created in the submerged piece of liver using a 4 cm deployable radiofrequency ablation probe connected to a RITA model 1500 RF generator (Angiodynamics, NY, USA). For tumor creation, the model was removed from the container and placed on a grounding pad connected to the generator. The probe was inserted in the center of the piece of liver under ultrasound guidance. The probe was then deployed to 1 cm and ablation was performed at 500 watts until target temperature of 100°C was reached.

The idea of the phantom is based on triangle similarity and a priori knowledge of the vertices in the phantom space. By measuring the ratio between the two segments EF and EG in Figure 9.3, coordinates of the point F in the X-Y space can be calculated according to equation (9.1), given that we know the exact geometry of the phantom.

$$\begin{aligned} X_F &= X_B + \frac{EF}{EG} \times (X_C - X_B) \\ Y_F &= Y_B + \frac{EF}{EG} \times (Y_C - Y_B) \end{aligned} \quad (9.1)$$

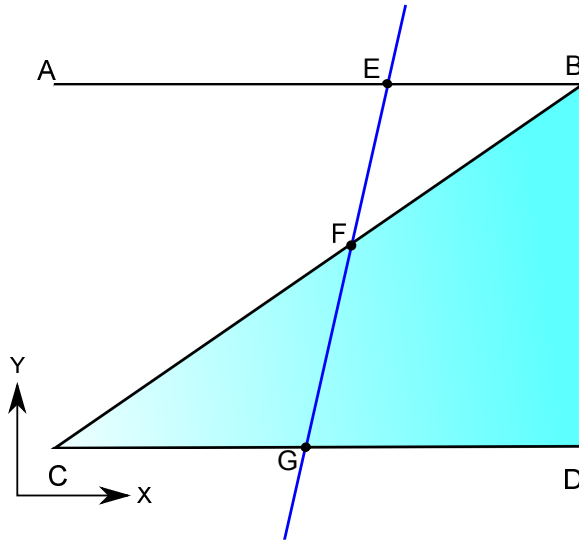


Figure 9.3: From the similar triangles (ABC) and (BCE), the coordinates of the point F can be determined by equation (9.1), given the ratio  $EF/EG$  and the exact geometry of the phantom.

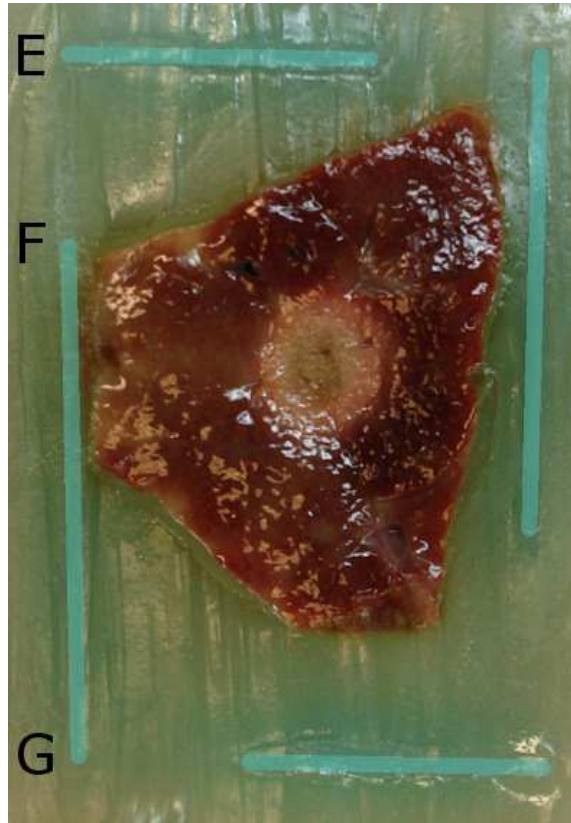


Figure 9.4: Cross section through the phantom showing the tissue and the fiducials. The segments  $EG$  and  $EF$  were measured for each fiducial to determine the ratio  $EF/EG$  at each phantom side.

Each side of the phantom forms a “*Z-Shape*” like the one in Figure 9.3. The phantom was scanned using robotized 3D-US and MRI, then a straight cut was made using a sharp knife through the ablated liver tissue. The tissue was then photographed next to a metric ruler. Figure 9.4 shows an image after cutting the phantom, where the lesion appears in the middle of the tissue, the points  $E$ ,  $F$ ,  $G$  in the image correspond to the same points in Figure 9.3. For each side of the phantom, we measured the segments  $EF$  and  $EG$  and calculated the coordinates of the point  $F$  using equation 9.1. Hence, we had four points lying on the cutting plane. These four points were used to define the plane in the phantom space; however, we want to find the corresponding plane in the images.

### 9.2.2 Phantom Imaging

Ultrasound data were collected using a Sonix RP ultrasound system (Ultrasonix Medical Corporation, Canada) with a 60mm-width linear array high frequency ultrasound transducer (L14/5W-60; 128 transducers). Real-time RF data acquisition was available through the Texo SDK provided by Ultrasonix. In order to provide reliable and reproducible volume information, the ultrasound data were sampled with a robot-based system, yielding a series of 2D parallel slices through the respective phantom. The phantoms were pre-positioned manually within the workspace of a high-precision three-DOF Cartesian robot. The robot translated the probe successively 1 mm in the elevation direction to cover the whole scanning area. To allow for elasticity images, the robot also performed at every elevation position one compression-decompression cycle with amplitude 1 mm (approx. 1.25% strain). At the top and bottom extreme of each such motion, one RF frame was captured. Strain images were generated using the algorithm introduced by [4].

MRI images of the phantoms were obtained using a 1.5 T Siemens Espree scanner (Siemens Medical Solutions, Malvern, PA). T-2 sequence images were collected at a slice thickness of 1 mm.

After scanning the phantoms using US and MRI, the phantoms were sliced and gross pathology (ground truth) images were obtained. Depending on the lesion size, one or two cuts were made per phantom. Measurements of the fiducials were taken. Also, the slices were positioned next to a metric ruler and photographed using a digital camera.

### 9.2.3 Pose Registration

Three-dimensional US and MRI image volumes were reconstructed for each phantom; scales of the reconstructed volumes were obtained from the machines. Previously, we defined the cutting plane in the phantom space. In order to transform the cutting



Figure 9.5: The phantom ready to be scanned with the robotized US probe.

plane from the phantom space to the image space, we need to determine the position and orientation of the fiducials in the image volume. During the MRI and US scans, the phantom was placed such that the image plane was orthogonal to the fiducial wedges, Figure 9.5. Consequently, the reference frame of the phantom space (phantom origin) was parallel to the reference frame of the image space (image origin). Hence, the orientation vector from the phantom space was directly mapped to the image space.

However, we still need a point to define the plane in the image space. Fiducials appearance in the image space was necessary to map this point from the phantom space to the image space. The fiducials were clearly visible on the MRI volumes, so the phantom space origin was determined with respect to the image origin. Thus, the point satisfying the plane equation was easily determined in the MRI image space. However, quality of the fiducials on the US images were not as good as on MRI.

Due to attenuation and shadowing, only the upper part of the US images showed distinguishable fiducials against the background. Nevertheless, since the dimensions of the fiducials were known, we virtually extrapolated the visible part of the fiducials to complete them. After that, the plane point was mapped in the US image space. The volumes were opened in an open-source data analysis and visualization application (ParaView) [113] and planes were interpolated using the slicing function.

Finally, the registration error was quantified by measuring the fiducials on the interpolated images and comparing them to the actual measurements done beforehand on the gross pathology (GP). It was not possible to measure all the fiducials on the US images, therefore, we couldn't calculate the US registration error. The MRI mean registration error was calculated for each slice by equation (9.2), where  $F^{MR}$  and  $F^{Phantom}$  are the fiducial lengths on the MRI image and the actual phantom respectively.

$$E = \frac{\sum_{i=1}^4 |F_i^{MR} - F_i^{Phantom}|}{4} \quad (9.2)$$

## 9.3 Results

We prepared 18 *Z-Shape* phantoms with pieces of bovine liver inside. After scanning and cutting the phantoms, four of them were not suitable for the experiment; either the tissue was extruded from the mold due to gelatin damage or the contrast between the fiducials and the background was not enough to take the measurements. The unsuitable phantoms were excluded and the experiments were performed on 14 phantoms. Depending on the lesion size, one or two cuts were made per phantom. The GP slices were registered and interpolated in both US and MRI volumes. Figure 9.6 shows a GP slice with resulting corresponding slices from US and MRI. The fiducials were distinct and clear in the MRI images. However, the attenuation and shadowing deteriorated the quality of fiducials in US images proportional to depth.

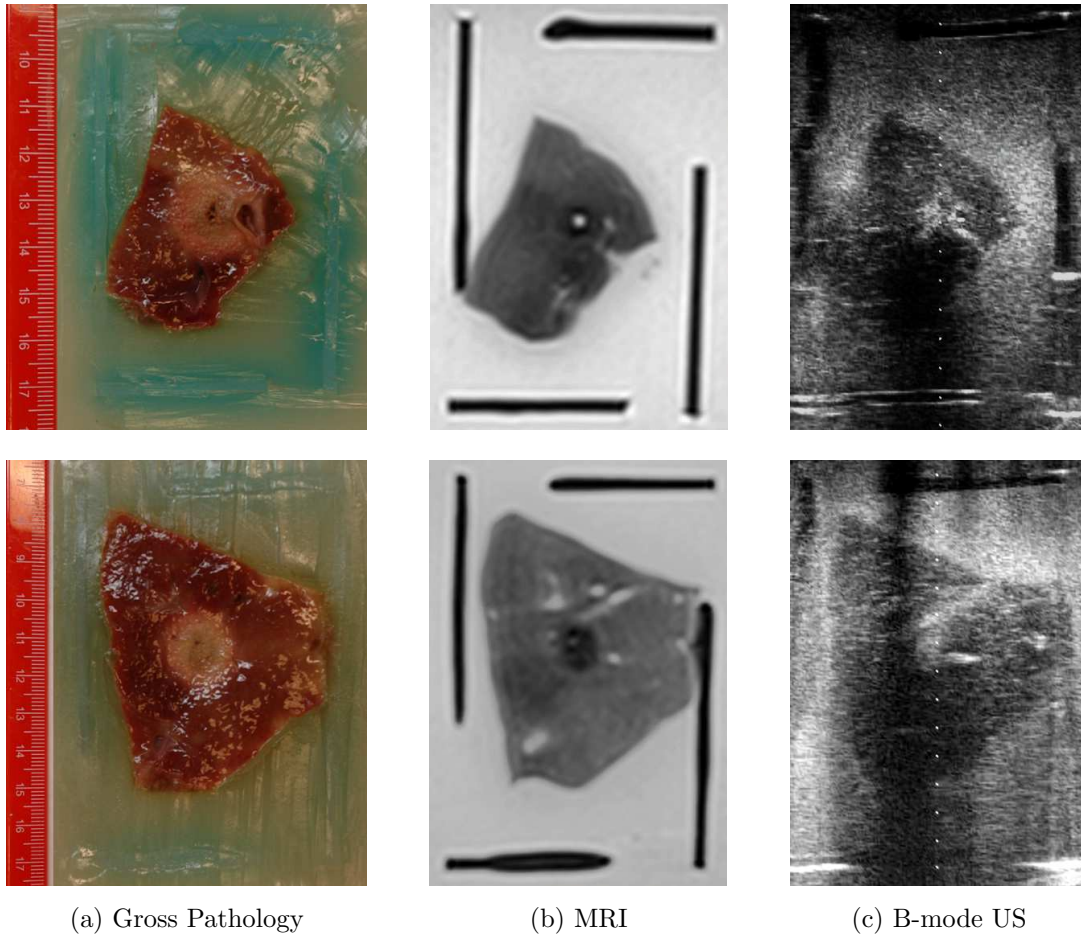


Figure 9.6: Gross pathology slices registered to corresponding MRI and US images using the “Z-Shape” correlation phantom.

Slice matching error was estimated by comparing the fiducial lengths, see equation (9.2). Figure 9.7 plots the mean error per slice for the MRI images. The data collected during the robotized US scan of the phantom were used to generate the strain images. Hence, the b-mode and strain images are two different representations of the same data and no registration is required to align them. Figure 9.8 shows examples of strain images correlated to actual lesions. Although the obtained strain images don’t clearly delineate the ablated lesions, a contrast can be observed between the ablated lesions and the surrounding tissue. As the ablated lesions are stiffer than the surrounding tissue, they have lower strain values and appear mostly darker.

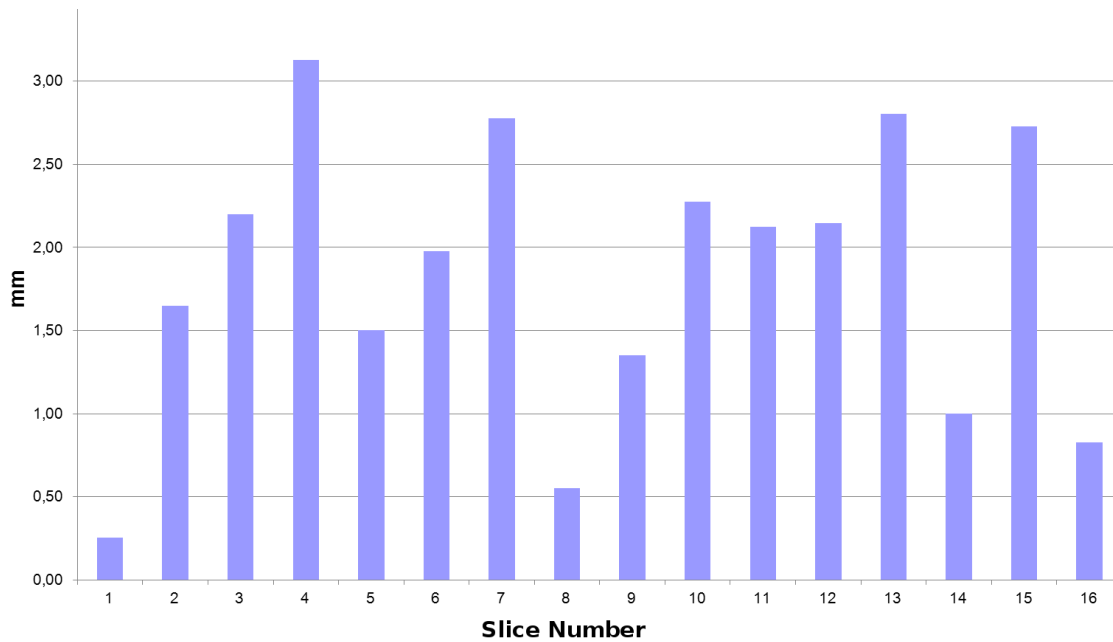


Figure 9.7: Mean error on the MRI slice calculated by measuring the fiducial lengths on the images and comparing them to the actual lengths on the gross pathology.

## 9.4 Discussion

Monitoring the ablation procedure is crucial to ensure that the tumor is completely treated. While different modalities can be used to perform this task, it is not clear how the area of necrosis correlates to the lesion on the image. Standard correlation method requires slicing the tissue and manually matching the slices. Instead, we developed an algorithmic approach to perform multimodal ablation correlation. The phantom geometry enabled unique pose estimation on different imaging modalities. It was necessary, however, that the phantom fiducials appear clearly in every imaging modality. Although this point was considered while preparing the phantom material, the fiducials appeared incomplete under US due to shadowing and attenuation. Therefore, the slice matching accuracy was measured based on the MRI images and found to be  $1.83 \pm 0.83$  mm, mean  $\pm$ SD.

It is obvious from the results in Figure 9.6 and 9.8 that lesions appear differently based on the imaging modality. This emphasizes the importance of developing such

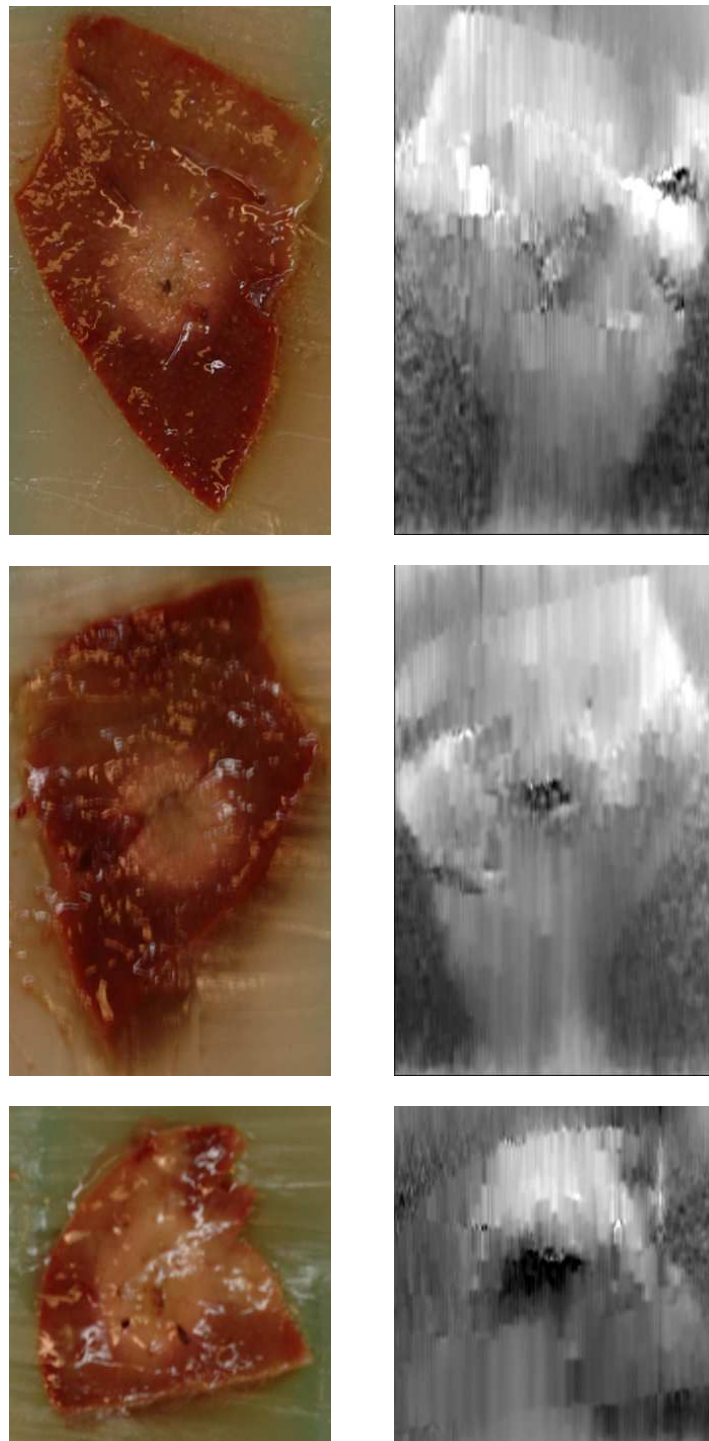


Figure 9.8: Gross pathology slices and the corresponding strain images.

a technique to enable accurate slice matching between different imaging modalities. This is particularly helpful for new imaging techniques such as elastography. Using this technique, strain images can be compared to ground truth (gross pathology) and quantitative relation can be drawn. However, this work focused on the correlation problem, a larger dataset will be considered to quantify the relation between lesion sizes obtained from different imaging techniques.

One of the drawbacks of this technique is that it is applicable only on ex-vivo tissue, while coagulation response differs in dead ex-vivo tissue compared to live in-vivo tissue [114]. Also, the approach was not optimal for US imaging, as the fiducials appeared fuzzy and incomplete. Yet US imaging is the most commonly used modality in ablation monitoring. Therefore, we consider in the next chapter a new ablation correlation approach suitable for US imaging and applicable in in-vivo experiments.

## 9.5 Conclusion

The recurrence rate after RFA procedures is remarkably high. One of the main reasons causing that is the uncertainty during the monitoring of the procedure. This uncertainty is directly related to inaccurate estimation of the necrotic area during the ablation. We developed a novel platform for ablation correlation to enable accurate comparison of ablated lesions on different imaging modalities. Using the geometrical properties of the used phantom, multimodal image slices were matched with GP slices. Hence, the approach allowed validation of the ablation outcome against a ground truth. The results showed how lesion sizes may vary significantly depending on the imaging technique. This indicates the need for such a validation scheme to standardize the ablation monitoring and eventually improve the RFA recurrence rate.

# Chapter 10

## In-Vivo Ablation Correlation

### 10.1 Introduction

We presented in the previous chapter a platform for ablation correlation, which enabled accurate ablation correlation between MRI and gross pathology images. However fiducial-based registration made the algorithm not optimal in case of US imaging. But US is the most commonly used ablation monitoring modality as it is portable, inexpensive, and radiation-free technique. In addition, various new US-based imaging techniques are being developed to enhance the US capability to monitor the ablation procedure; one of them for instance is elastography. Therefore, an approach which avoids the limitation of the previous one regarding US imaging is required.

Another aspect that encouraged a new solution for ablation correlation is that a phantom-based solution is not applicable in an in-vivo setup. However, tissue coagulation response differs in live in-vivo tissue in comparison to dead ex-vivo tissue [114]. For this reason it is more important to find the correlation between in-vivo necrosis and in-vivo imaging.

We propose an in-vivo approach to correlate ablation outcomes on multimodal images with actual necroses. This technique utilizes tracking systems to map intraoperative

images and an actual cut through the ablated lesion in a common reference frame; hence, it enables in-vivo ablation correlation. The method was tested in an animal study, where intraoperative MRI and US images were acquired to visualize a number of ablations made in a porcine liver. Eventually, the ablations on the acquired images were compared to gross and histopathology (HP) results.

## 10.2 Methods

The aim is to spatially correlate the actual necrosis and intraoperative images. This requires mapping two images showing the ablated tumor and obtained using different modalities in the same coordinate system. We developed a tracking-based approach to register multimodal images in one reference frame. An electromagnetic (EM) 6D sensor was anchored as the reference frame adjacent to the lesion to minimize the effect of tissue deformation with respect to the reference. In the experiments, we used a medSAFE EM tracking system (Ascension, VT, USA). Intraoperative images were obtained using a Sonix RP ultrasound system with a motor-driven 3D probe (Ultrasonix Medical Corporation, BC, Canada) and a Siemens Espree MRI 1.5 T scanner (Siemens AG, Munich, Germany). Also a Polaris optical tracking system (NDI, Ontario, Canada) was used to track the 3D US probe to avoid EM signal interference due to the motor.

### 10.2.1 Local Rigidity

Deformation is a major challenge when dealing with liver tissues. In the previous approach the deformation was controlled by embedding the tissue in a gelatin mold. Also in this approach it is required to limit the liver deformation effect. Usually when using a tracking system, the reference frame is the transmitter in case of EM tracking or the camera in case of optical tracking. Instead, since we are only interested in the small region containing the tumor, we defined the reference frame within this region

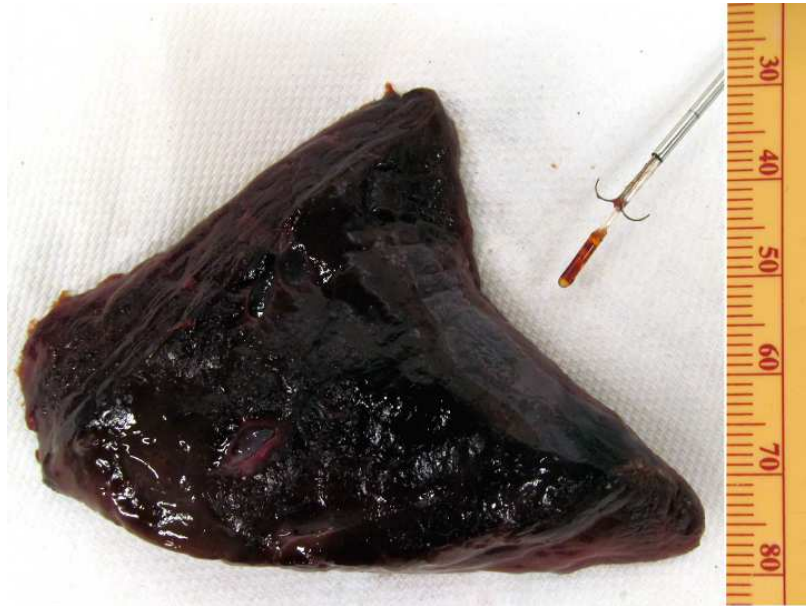


Figure 10.1: EM sensor glued to a biopsy needle with a hooked end. First the needle was used to insert the EM sensor into the tissue, and then the anchor was deployed to keep the sensor in place.

to minimize the liver deformation effect relative to the reference. This was achieved by anchoring a 6D EM sensor ((Model 180, Ascension, VT, USA) ) adjacent to the ablated lesion.

A biopsy needle was used to insert the sensor into the tissue, Figure 10.1. The sensor was first glued to a biopsy needle with a hooked end. First, the anchor and the sensor were retracted inside the needle shaft. Then, the shaft was inserted into the tissue to place the sensor next to the lesion. The anchor was deployed by pushing the needle out of the surrounding shaft. This anchor helped to keep the sensor in place in the tissue by preventing translation and rotation around its own axis.

### 10.2.2 US Volume Mapping

The idea is to map intraoperative image volumes in the anchored sensor frame, then make a straight cut through the ablated lesion and interpolate the cutting plane in

the same reference frame. Figure 10.2 shows a sketch demonstrating the procedure and the transformations involved in case of US imaging. The tracked 3D US probe (U) was used to acquire a volume with an origin (V). Cuboid 1 represents a region of the liver with a lesion inside. Sensor (S) was anchored into the tissue next to the lesion. Rigid body (R) with optical markers was mounted to the EM transmitter (M); the use of two tracking systems was only necessary because the 3D US probe was not compatible with the EM tracking system.

The arrows in the sketch represent the transformations which were either given directly by the tracking systems or were determined beforehand through calibrations. The  ${}^M T_R$  represents the calibration between the EM and optical trackers, it was calculated by simultaneously recording two sets of points relative to the EM transmitter (M) and the rigid body (R). These points were collected using a pointer calibrated in both tracking systems using the standard pivot calibration procedure. The two sets were then fed to Horn's method to compute  ${}^M T_R$ .

The  ${}^U T_V$  was determined in two steps: first the US probe was calibrated to get the transformation from the optical markers mounted on the US probe to the origin of the central image, second the origin of the volume was determined relative to the central image. The sensor-to-volume transformation matrix  ${}^S T_V$  is calculated by:

$${}^S T_V = {}^S T_M \cdot {}^M T_R \cdot {}^R T_O \cdot {}^O T_U \cdot {}^U T_V \quad (10.1)$$

### 10.2.3 Plane Mapping

Cuboid 2 in Figure 10.2 represents the liver region after cutting through the lesion; the assumption is that the sensor position (S) is fixed before and after the cut with respect to the lesion. A tracked pointer was used to scan the cutting plane and collect a point cloud. The points were then mapped to the sensor space and subsequently to the US volume space using the following equation:

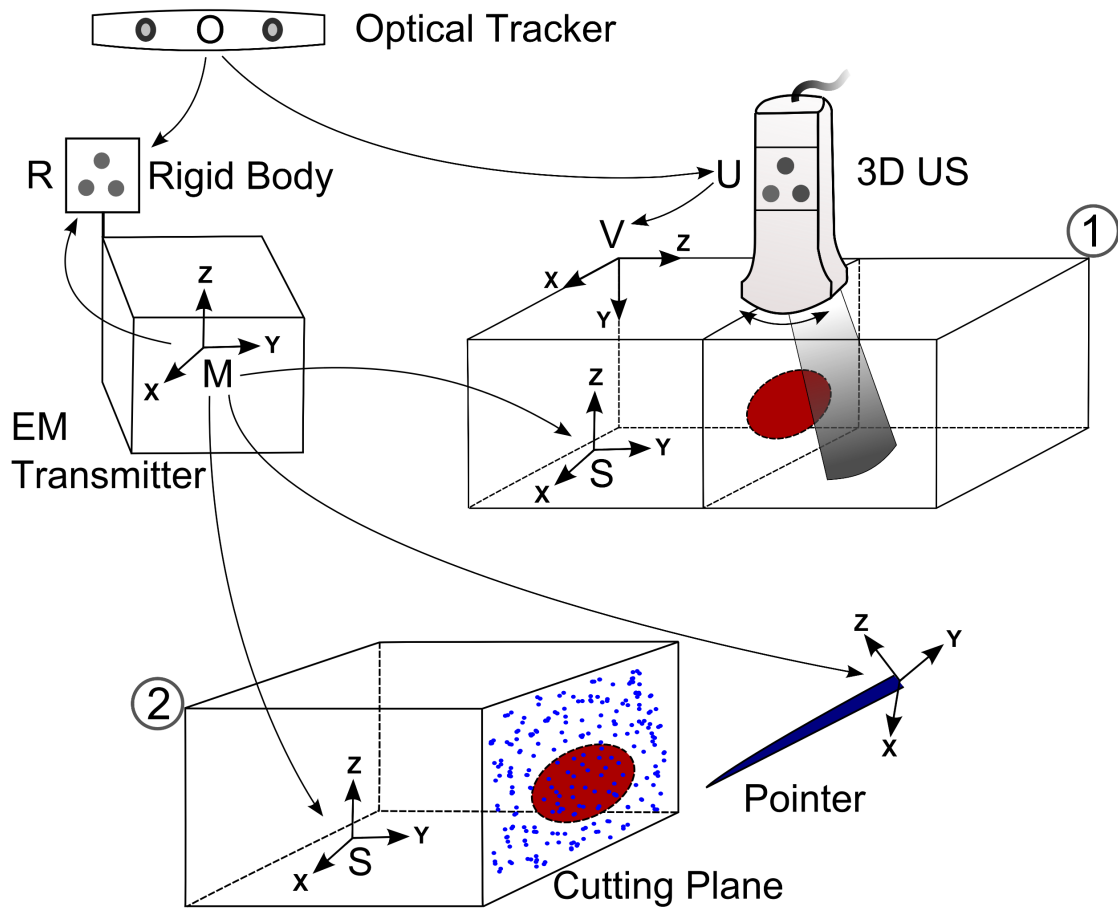


Figure 10.2: Sketch of the approach setup while using US to image the ablation: step 1 symbolizes a liver section having a lesion inside and a 6D EM sensor (S) anchored next to the lesion; step 2 is after cutting through the lesion, where a tracked pointer was used to collect points on the cutting surface. Transformations between frames were either obtained directly from the tracking systems or via calibration.

$$(x_V \ y_V \ z_V \ 1)^T = ({}^S T_V)^{-1} \cdot ({}^M T_S)^{-1} \cdot (x_M \ y_M \ z_M \ 1)^T \quad (10.2)$$

where  $(x_M \ y_M \ z_M)$  represents a point from the collected point cloud in the EM tracking space, and  $(x_V \ y_V \ z_V)$  is the corresponding point in the image volume space. Finally, the mapped points were fitted into a plane and interpolated in the volume.

### 10.2.4 Validation Test

This test aims to prove that the end-to-end error of the proposed scheme is within a reasonable margin. We built a phantom with a feature that can be seen with the naked eye as well as with US. A cubic phantom was made of transparent gelatin mold, while keeping 4 marginal sides of the phantom occupied by plastic sheets of 2 mm thickness. After the mold had been hardened, the plastic sheets were replaced by gelatin mixed with cellulose to create a *speckle layer* when imaged with US. Then an EM sensor was anchored in the middle of the phantom cube, ca. 3 cm distance from each layer. After that, we immersed the phantom in a water tank and scanned each of the four sides using tracked US. Accordingly, we had 4 US volumes each containing a 2 mm *speckle layer*.

Then the phantom was taken out of the water and the outer transparent gelatin covering the *speckle layers* was removed to expose the surfaces of the layers, Figure 10.3. Each surface was scanned by a tracked pointer and the collected points were fed to equation (10.2). The resulting points were fitted into a plane and interpolated in the US volume to check if it was within the 2 mm *speckle layer*.

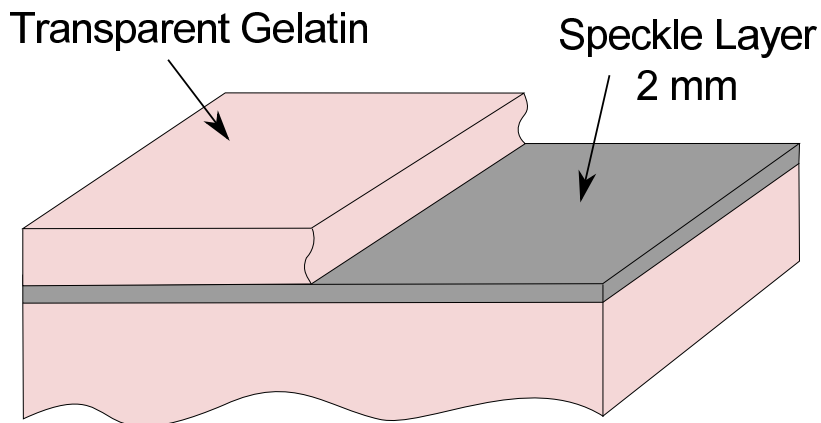


Figure 10.3: Drawing illustrates one side of the phantom: the transparent gelatin was removed after the US acquisition, then points were collected on the speckle layer.

## 10.3 Animal Experiment

The aim of this experiment was to test the feasibility of the outlined approach, particularly in case of US imaging. Four ablations were made in a pig liver. Afterwards, we stitched 4 MRI fiducials to the surface of the liver and closed the pig. Then a T1 VIBE (volumetric interpolated breath-hold examination) MRI sequence was acquired. After that, the pig was reopened and the EM transmitter was placed close to the liver. Next, an EM sensor was anchored approximately in the middle of the ablated lesions using a thin biopsy needle. Then we recorded the positions of the fiducials using a tracked pointer. Thereby, we determined the transformation between the anchored sensor and the MRI volume. Figure 10.4 shows the liver while we were registering the MRI fiducials using the pointer. Also it shows the EM sensor glued to the biopsy needle; a hook at the needle end was used to keep the sensor in place inside the tissue.

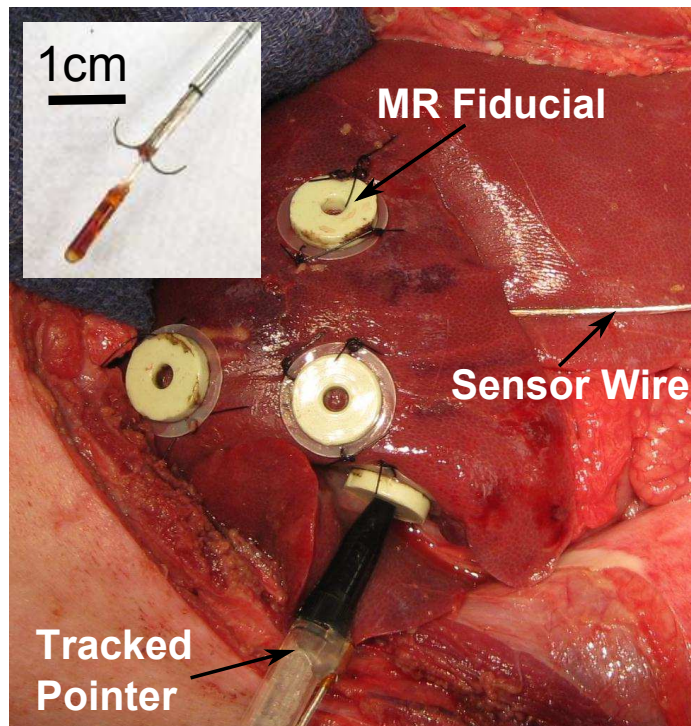


Figure 10.4: Tracked pointer while registering the MRI fiducials during the animal experiment. Overlaid picture explains how the anchored sensor was deployed inside the tissue.

Afterwards, the fiducials were removed and tracked 3D US scans of the lesions were acquired. With the embedded sensor still in place inside the tissue, the whole liver was harvested and placed on a side table. Then we cut straight through each lesion and collected a point cloud on the cutting surface using the tracked pointer. Finally, the lesions were sliced and mounted on glass slides, and later on HP tests were performed.

## 10.4 Results

Figure 10.5 shows two planes in one of the validation US volumes. One plane is the mapped *speckle layer* and the other is an arbitrary axial plane. As shown in the image, the mapped plane was within the 2 mm speckle. The 4 resulting planes of the validation test were all within the corresponding *speckle layers*. Hence, the end-to-end plane mapping error, using a nonrigid gelatin phantom and having the sensor anchored ca. 3 cm apart from the scanned surface, was  $\leq 2$  mm.

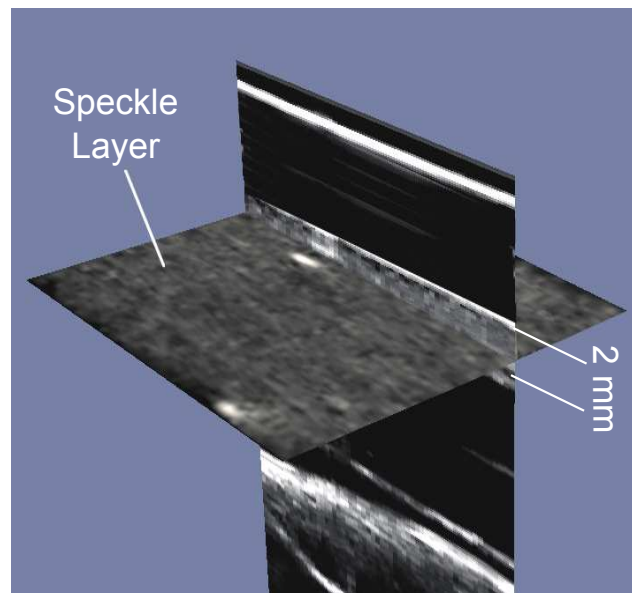


Figure 10.5: Example of the validation results demonstrates that the *speckle layer* was mapped correctly to the US volume; i.e. the end-to-end plane mapping error was within 2 mm.

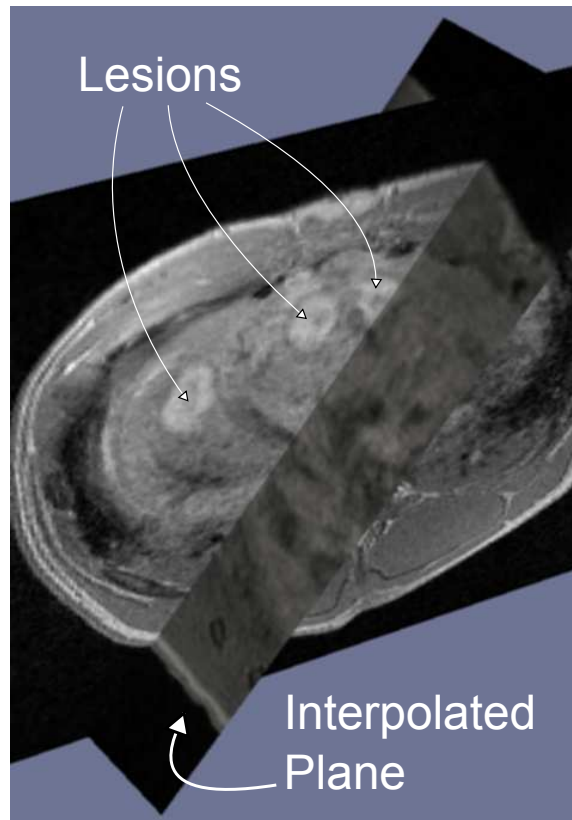


Figure 10.6: Cross section in the MRI volume showing three of the lesions and one of the mapped planes intersecting the corresponding lesion.

In the animal experiment, the four cutting planes corresponding to the lesions were mapped into the MRI and US volumes. Figure 10.6 demonstrates a cross section in the MRI volume showing three of the lesions and one of the interpolated planes cutting through the corresponding lesion. One of the ablations (left lesion in the image) happened to be relatively far from the anchored sensor (5 cm) and located in a different liver lobe. Except for this lesion, the resulting planes intersected the corresponding lesions in the volumes.

Figure 10.7 represents one set of the correlated images showing a lesion on the interpolated MRI and US slices and the corresponding necrosis in gross and histopathology. Manual segmentation was performed to determine the margin of the lesions. Areas of the lesions on different modalities and the gross pathology were calculated and

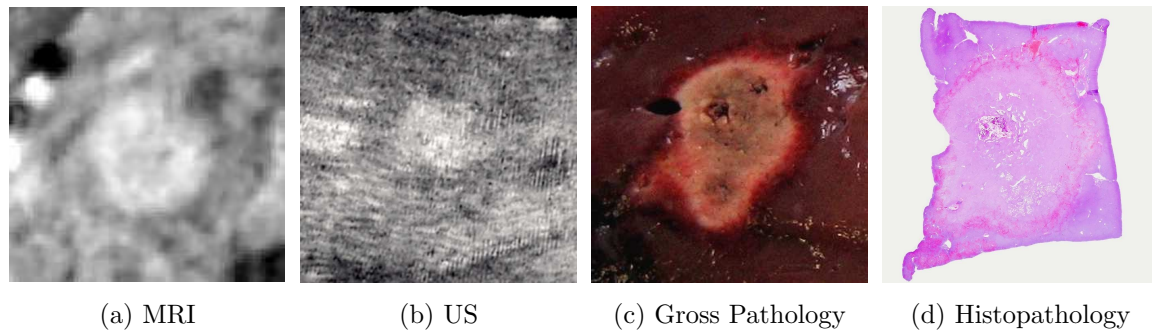


Figure 10.7: Set of results (MRI, US, gross and histopathology slices) shows the ablated lesion and allows for multimodal ablation correlation.

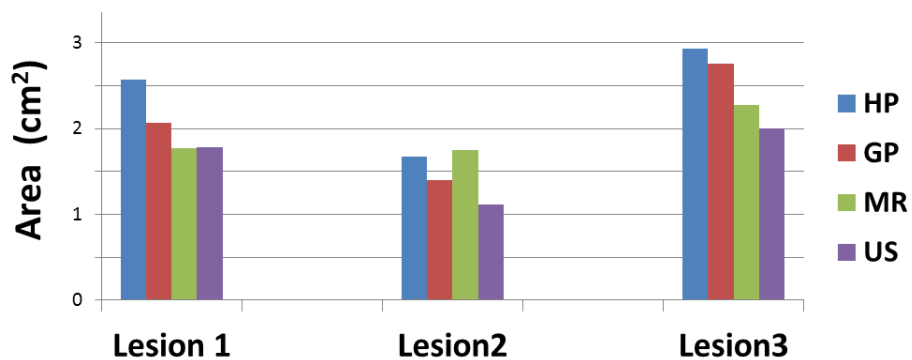


Figure 10.8: Chart plotting areas of the lesions measured on correlated histopathology (ground truth), gross pathology, MRI, and US images.

compared to the HP as a ground truth. Figure 10.8 plots the areas of the segmented lesions.

## 10.5 Discussion

The proposed approach provided a multimodal in-vivo ablation correlation. In contrast to the method used in [115], we developed a tracking-based approach which doesn't require slicing the tissue at certain intervals. In addition, this approach is particularly advantageous in case of US imaging, where fiducial-based registration is difficult to achieve. The approach was feasible in a real liver ablation scenario. The

anchor (Figure 10.4) prevented sensor translations and rotations around its own axis. By anchoring the sensor adjacent to the lesions, the effect of the other two degrees of freedom was minimized. We performed a validation test and found the overall accuracy  $\leq 2$  mm.

Three out of four lesions in the animal experiment were successfully correlated, while the fourth failed because it was located in a different lobe, far from the reference sensor. In this study, we used only one reference sensor and tried to center it between the lesions. In order to improve local rigidity in future experiments, more than one sensor can be used and the number of lesions per sensor will be limited to two.

Conventional US (Figure 10.7b) is the common modality for ablation monitoring [101], yet in agreement with [116], the US results underestimated the necrosis area compared to the HP. Measurements on MRI were closer to the actual necroses. In this initial experiment, we used a limited number of samples to investigate the feasibility of the approach. In future work, it is planned to increase the number of samples and include other imaging modalities such as US elastography.

## 10.6 Conclusion

We developed a novel technique to perform multimodal ablation validation in an in-vivo setup. The main idea of the approach is to map intraoperative images showing the lesion and a cut through the lesion in a common reference frame. This reference frame was defined by a 6D EM sensor anchored next to the lesion. The proposed technique was feasible in a real liver ablation experiment and enabled correlation of actual necroses (gross and histopathology) and intraoperative images (MRI and US). Ultimately, this will improve the interpretation of the ablation monitoring and reduce the recurrence rates associated with RFA.



# Chapter 11

## Summary

Image guided navigation is used routinely in surgical applications such as neurosurgery and orthopedics. However, its adaption to soft organs faces some challenges, mainly because of the organ's deformability which leads to intraoperative anatomical changes. To navigate reliably and accurately in the liver, the navigation system must be able to intraoperatively reflect the actual surgical situation, especially in the tumor region. The methods developed aimed to solve this problem for minimally invasive liver interventions. We focused on minimally invasive procedures for two reasons. First, it has a great benefit for the patient. Second, navigation is particularly important in such procedures, as the surgeon has no direct access to the organ.

In this work, we studied two important points which directly affect the efficiency of minimally invasive navigated interventions.

- Intraoperative estimation of the tumor position
- Evaluation of the RFA monitoring feedback

Two navigation approaches based on tracked 2D ultrasound were developed. The approaches are focused on the tumor to reach high accuracy at the navigation target. Intraoperative update of the tumor position was triggered by scanning the tumor region using a tracked ultrasound probe. The first method built a 3D ultrasound

---

volume from the acquired 2D images, then used an initial 3D tumor segmentation to find the new position of the tumor in the reconstructed volume. The second method segmented the tumor in automatically selected ultrasound frames, not necessarily covering the whole tumor, to build a sparse tumor surface. Then an initial 3D tumor segmentation was registered to the sparse surface points to estimate the tumor position.

As the proposed techniques are based on 2D ultrasound, they have the following advantages:

- Repeatable throughout the surgical procedure
- Applicable in laparoscopic interventions and ablation procedures
- Radiation-free and without additional overhead to the surgical workflow

We tested the approaches in needle navigation experiments on ex-vivo porcine liver. The results showed that the methods can quickly and accurately compensate for changes in the tumor position during the procedure. This provides a solution for intraoperative tumor shift caused by patient movement or surgical manipulation. It is ideal to combine our focused techniques with preoperative liver models to benefit from their larger field of view and better visualization. Thereby, the whole anatomy is visualized and at the same time high navigation accuracy focused on the tumor is achieved.

In the second part of the thesis, we developed methods to assess RFA ablation outcomes by correlating intraoperative images of ablated lesions to actual necroses. In an ex-vivo experiment, ablated lesions were observed using MRI and ultrasound. Ablations were made in pieces of bovine liver encompassed by a gelatin phantom. The geometrical properties of the phantom enabled unique pose estimation on different imaging modalities including gross pathology as a ground truth showing the actual necroses. The results showed how lesion sizes may significantly vary depending on the imaging technique. This encouraged us to develop another ablation correlation approach, which is based on EM tracking and applicable in in-vivo studies.

---

The in-vivo approach mapped intraoperative images of the ablated lesions and the actual liver in a common reference frame. Hence, the transformation between an actual cut through the lesion and the corresponding slice in each of the acquired image was determined. The technique proved to be feasible in an animal experiment and enabled correlation of actual necroses to intraoperative images. Results of the ex-vivo and in-vivo experiments showed that the feedback given to the surgeon, upon which the extent of the ablation is determined, varies depending on the imaging modality. This indicates the need for such validation schemes to standardize the ablation monitoring, especially for potential techniques such as ultrasound elastography, and eventually improve the RFA recurrence rate.



## Bibliography

- [1] O. V. Solberg, T. Langø, G. A. Tangen, R. Mårvik, B. Ystgaard, A. Rethy, and T. A. N. Hernes, “Navigated ultrasound in laparoscopic surgery,” *Minimally Invasive Therapy & Allied Technologies*, vol. 18, no. 1, pp. 36–53, 2009.
- [2] T. Lange, N. Papenberg, S. Heldmann, J. Modersitzki, B. Fischer, H. Lamecker, and P. M. Schlag, “3D ultrasound-CT registration of the liver using combined landmark-intensity information,” *International journal of computer assisted radiology and surgery*, vol. 4, no. 1, pp. 79–88, 2009.
- [3] Y. Boykov and V. Kolmogorov, “An experimental comparison of min-cut/max-flow algorithms for energy minimization in vision,” *Pattern Analysis and Machine Intelligence, IEEE Transactions on*, vol. 26, no. 9, pp. 1124–1137, 2004.
- [4] H. Rivaz, I. Fleming, L. Assumpcao, G. Fichtinger, U. Hamper, M. Choti, G. Hager, and E. Boctor, “Ablation monitoring with elastography: 2D in-vivo and 3D ex-vivo studies,” in *Medical Image Computing and Computer-Assisted Intervention–MICCAI 2008*. Springer, 2008, pp. 458–466.
- [5] [www.who.int/mediacentre/factsheets](http://www.who.int/mediacentre/factsheets), “World Health Organization,” retrieved: 15/1/2013.
- [6] D. Ansari and R. Andersson, “Radiofrequency ablation or percutaneous ethanol

- injection for the treatment of liver tumors,” *World journal of gastroenterology: WJG*, vol. 18, no. 10, p. 1003, 2012.
- [7] S. Breitenstein, J. Belghiti, R. S. Chari, J. M. Llovet, C.-M. Lo, M. A. Morse, T. Takayama, J.-N. Vauthey, and P.-A. Clavien, *Malignant Liver Tumors: Current and Emerging Therapies*. Wiley-Blackwell, 2011.
- [8] M. Zijlmans, T. Langø, E. F. Hofstad, C. F. Van Swol, and A. Rethy, “Navigated laparoscopy-liver shift and deformation due to pneumoperitoneum in an animal model,” *Minimally Invasive Therapy & Allied Technologies*, vol. 21, no. 3, pp. 241–248, 2012.
- [9] M. A. Clifford, F. Banovac, E. Levy, and K. Cleary, “Assessment of hepatic motion secondary to respiration for computer assisted interventions,” *Computer Aided Surgery*, vol. 7, no. 5, pp. 291–299, 2002.
- [10] A. F. Kolen, N. R. Miller, E. E. Ahmed, and J. C. Bamber, “Characterization of cardiovascular liver motion for the eventual application of elasticity imaging to the liver in vivo,” *Physics in medicine and biology*, vol. 49, no. 18, p. 4187, 2004.
- [11] W. Wein, J.-Z. Cheng, and A. Khamene, “Ultrasound based respiratory motion compensation in the abdomen,” *MICCAI 2008 Workshop on Image Guidance and Computer Assistance for Softissue Interventions*, vol. 32, no. 6, p. 294, 2008.
- [12] M. Nakamoto, H. Hirayama, Y. Sato, K. Konishi, Y. Kakeji, M. Hashizume, and S. Tamura, “Recovery of respiratory motion and deformation of the liver using laparoscopic freehand 3D ultrasound system,” *Medical image analysis*, vol. 11, no. 5, pp. 429–442, 2007.
- [13] M. Kudo, “Local ablation therapy for hepatocellular carcinoma: current status and future perspectives,” *Journal of gastroenterology*, vol. 39, no. 3, pp. 205–214, 2004.
- [14] T. Varghese, J. Zagzebski, Q. Chen, U. Techavipoo, G. Frank, C. Johnson,

- A. Wright, and F. L. Jr, "Ultrasound monitoring of temperature change during radiofrequency ablation: preliminary in-vivo results," *Ultrasound in Medicine & Biology*, vol. 28, no. 3, pp. 321 – 329, 2002.
- [15] <http://www.cancer.org/cancer/livercancer/detailedguide>, "Liver Cancer - Detailed Guide," retrieved: 25/11/2012.
- [16] A. K. Singh, C. G. Cronin, H. A. Verma, G. W. Boland, S. Saini, P. R. Mueller, and D. V. Sahani, "Imaging of Preoperative Liver Transplantation in Adults: What Radiologists Should Know," *Radiographics*, vol. 31, no. 4, pp. 1017–1030, 2011.
- [17] <http://www.cancer.gov/cancertopics/cancerlibrary/what-is-cancer>, "What Is Cancer?" retrieved: 22/11/2012.
- [18] A. Jemal, F. Bray, M. M. Center, J. Ferlay, E. Ward, and D. Forman, "Global cancer statistics," *CA: a cancer journal for clinicians*, vol. 61, no. 2, pp. 69–90, 2011.
- [19] A. Rao, G. Rao, and I. Ahmed, "Laparoscopic or open liver resection? Let systematic review decide it," *The American Journal of Surgery*, vol. 204, no. 2, pp. 222 – 231, 2012.
- [20] W. Bechstein, "Which liver metastases are resectable?" *European Journal of Cancer Supplements*, vol. 5, no. 5, pp. 301–306, 2007.
- [21] T. D. Mast, D. P. Pucke, S. E. Subramanian, W. J. Bowlus, S. M. Rudich, and J. F. Buell, "Ultrasound Monitoring of In Vitro Radio Frequency Ablation by Echo Decorrelation Imaging," *Journal of Ultrasound in Medicine*, vol. 27, no. 12, pp. 1685–1697, 2008.
- [22] R. Mostaedi, Z. Milosevic, H. S. Han, and V. P. Khatri, "Laparoscopic liver resection: Current role and limitations," *World journal of gastrointestinal oncology*, vol. 4, no. 8, pp. 187–192, Aug 2012.

## BIBLIOGRAPHY

---

- [23] B. Edwin, A. Nordin, A. Kazaryan *et al.*, “Laparoscopic liver surgery: new frontiers,” *Scandinavian Journal of Surgery*, vol. 100, no. 1, p. 54, 2011.
- [24] J. F. Buell, D. Cherqui, D. A. Geller, N. O’Rourke, D. Iannitti, I. Dagher, A. J. Koffron, M. Thomas, B. Gayet, H. S. Han, G. Wakabayashi, G. Belli, H. Kaneko, C. G. Ker, O. Scatton, A. Laurent, E. K. Abdalla, P. Chaudhury, E. Dutson, C. Gamblin, M. D’Angelica, D. Nagorney, G. Testa, D. Labow, D. Manas, R. T. Poon, H. Nelson, R. Martin, B. Clary, W. C. Pinson, J. Martinie, J. N. Vauthey, R. Goldstein, S. Roayaie, D. Barlet, J. Espat, M. Abecassis, M. Rees, Y. Fong, K. M. McMasters, C. Broelsch, R. Busuttil, J. Belghiti, S. Strasberg, and R. S. Chari, “The international position on laparoscopic liver surgery: The Louisville Statement, 2008,” *Ann. Surg.*, vol. 250, no. 5, pp. 825–830, Nov 2009.
- [25] R. M. Cannon, G. N. Brock, M. R. Marvin, and J. F. Buell, “Laparoscopic liver resection: an examination of our first 300 patients,” *J. Am. Coll. Surg.*, vol. 213, no. 4, pp. 501–507, Oct 2011.
- [26] K. T. Nguyen, J. W. Marsh, A. Tsung, J. J. Steel, T. C. Gamblin, and D. A. Geller, “Comparative benefits of laparoscopic vs open hepatic resection: a critical appraisal,” *Arch Surg*, vol. 146, no. 3, pp. 348–356, Mar 2011.
- [27] E. Westebring-van der Putten, R. Goossens, J. Jakimowicz, and J. Dankelman, “Haptics in minimally invasive surgery—a review,” *Minimally Invasive Therapy & Allied Technologies*, vol. 17, no. 1, pp. 3–16, 2008.
- [28] L. Vigano, C. Tayar, A. Laurent, and D. Cherqui, “Laparoscopic liver resection: a systematic review,” *Journal of hepato-biliary-pancreatic surgery*, vol. 16, no. 4, pp. 410–421, 2009.
- [29] S. Rossi, F. Fornari, C. Pathies, and L. Buscarini, “Thermal lesions induced by 480 KHz localized current field in guinea pig and pig liver.” *Tumori*, vol. 76, no. 1, p. 54, 1990.

- [30] J. P. McGahan, P. D. Browning, J. M. Brock, and H. Tesluk, "Hepatic ablation using radiofrequency electrocautery," *Investigative radiology*, vol. 25, no. 3, pp. 267–270, 1990.
- [31] R. A. Brown, "A computerized tomography-computer graphics approach to stereotaxic localization," *Journal of neurosurgery*, vol. 50, no. 6, pp. 715–720, 1979.
- [32] T. M. Peters and K. R. Cleary, *Image-guided Interventions: Technology and Applications*. Springer, 2008.
- [33] C. R. Maurer, J. M. Fitzpatrick, M. Y. Wang, S. Member, R. L. Galloway, R. J. Maciunas, and G. S. Allen, "Registration of Head Volume Images Using Implantable Fiducial Markers," *IEEE Transactions on Medical Imaging*, vol. 16, pp. 447–462, 1997.
- [34] H. J. Scudder, "Introduction to computer aided tomography," *Proceedings of the IEEE*, vol. 66, no. 6, pp. 628–637, 1978.
- [35] G. T. Herman and H. K. Liu, "Display of three-dimensional information in computed tomography," *Journal of Computer Assisted Tomography*, vol. 1, no. 1, pp. 155–160, 1977.
- [36] D. A. Christensen, *Ultrasonic Bioinstrumentation*. Wiley New York, 1988.
- [37] M. W. Walker, L. Shao, and R. A. Volz, "Estimating 3-D location parameters using dual number quaternions," *CVGIP: image understanding*, vol. 54, no. 3, pp. 358–367, 1991.
- [38] K. Horn, Berthold, "Closed-form solution of absolute orientation using unit quaternions," *Journal of the Optical Society of America A*, vol. 4, no. 4, pp. 629–642, 1987.
- [39] P. J. Besl and N. D. McKay, "Method for registration of 3-D shapes," in

## BIBLIOGRAPHY

---

- Robotics-DL tentative*. International Society for Optics and Photonics, 1992, pp. 586–606.
- [40] A. J. Herline, J. D. Stefansic, J. P. Debelak, S. L. Hartmann, C. W. Pinson, R. L. Galloway, and W. C. Chapman, “Image-guided surgery: preliminary feasibility studies of frameless stereotactic liver surgery,” *Archives of Surgery*, vol. 134, no. 6, p. 644, 1999.
- [41] D. M. Cash, T. K. Sinha, W. C. Chapman, H. Terawaki, B. M. Dawant, R. L. Galloway, and M. I. Miga, “Incorporation of a laser range scanner into image-guided liver surgery: Surface acquisition, registration, and tracking,” *Medical Physics*, vol. 30, p. 1671, 2003.
- [42] D. M. Cash, M. I. Miga, T. K. Sinha, R. L. Galloway, and W. C. Chapman, “Compensating for intraoperative soft-tissue deformations using incomplete surface data and finite elements,” *Medical Imaging, IEEE Transactions on*, vol. 24, no. 11, pp. 1479–1491, 2005.
- [43] M. Markert, S. Weber, and T. C. Lueth, “Manual registration of ultrasound with CT/planning data for hepatic surgery,” *Stud Health Technol Inform*, vol. 125, pp. 319–321, 2007.
- [44] K. J. Oldhafer, G. A. Stavrou, G. Prause, H.-O. Peitgen, T. C. Lueth, and S. Weber, “How to operate a liver tumor you cannot see,” *Langenbeck’s archives of surgery*, vol. 394, no. 3, pp. 489–494, 2009.
- [45] S. Beller, M. Hünerbein, S. Eulenstein, T. Lange, and P. M. Schlag, “Feasibility of navigated resection of liver tumors using multiplanar visualization of intraoperative 3-dimensional ultrasound data,” *Ann. Surg.*, vol. 246, pp. 288–294, Aug 2007.
- [46] S. Chopra, M. Hünerbein, S. Eulenstein, T. Lange, P. Schlag, and S. Beller, “Development and validation of a three dimensional ultrasound based

- navigation system for tumor resection,” *European Journal of Surgical Oncology (EJSO)*, vol. 34, no. 4, pp. 456–461, 2008.
- [47] M. Peterhans, A. vom Berg, B. Dagon, D. Inderbitzin, C. Baur, D. Candinas, and S. Weber, “A navigation system for open liver surgery: design, workflow and first clinical applications,” *The International Journal of Medical Robotics and Computer Assisted Surgery*, vol. 7, no. 1, pp. 7–16, 2011.
- [48] C. D. Herickhoff, E. D. Light, K. F. Bing, S. Mukundan, G. A. Grant, P. D. Wolf, and S. W. Smith, “Dual-mode intracranial catheter integrating 3D ultrasound imaging and hyperthermia for neuro-oncology: feasibility study,” *Ultrason Imaging*, vol. 31, pp. 81–100, Apr 2009.
- [49] E. D. Light, S. F. Idriss, K. F. Sullivan, P. D. Wolf, and S. W. Smith, “Real-time 3D laparoscopic ultrasonography,” *Ultrasonic Imaging*, vol. 27, pp. 129–144, Jul 2005.
- [50] O. V. Solberg, F. Lindseth, H. Torp, R. E. Blake, and T. A. Nagelhus Hernes, “Freehand 3D ultrasound reconstruction algorithms—a review,” *Ultrasound Med Biol*, vol. 33, pp. 991–1009, Jul 2007.
- [51] T. Langø, S. Vijayan, A. Rethy, C. Våpenstad, O. V. Solberg, R. Mårvik, G. Johnsen, and T. N. Hernes, “Navigated laparoscopic ultrasound in abdominal soft tissue surgery: technological overview and perspectives,” *International journal of computer assisted radiology and surgery*, vol. 7, no. 4, pp. 585–599, 2012.
- [52] K. Konishi, M. Nakamoto, Y. Kakeji, K. Tanoue, H. Kawanaka, S. Yamaguchi, S. Ieiri, Y. Sato, Y. Maehara, S. Tamura, and M. Hashizume, “A real-time navigation system for laparoscopic surgery based on three-dimensional ultrasound using magneto-optic hybrid tracking configuration,” *International Journal of Computer Assisted Radiology and Surgery*, vol. 2, pp. 1–10, 2007.
- [53] M. Nakamoto, K. Nakada, Y. Sato, K. Konishi, M. Hashizume, and

- S. Tamura, "Intraoperative Magnetic Tracker Calibration Using a Magneto-Optic Hybrid Tracker for 3-D Ultrasound-Based Navigation in Laparoscopic Surgery," *Medical Imaging, IEEE Transactions on*, vol. 27, no. 2, pp. 255–270, feb. 2008.
- [54] M. Feuerstein, T. Mussack, S. M. Heining, and N. Navab, "Registration-free laparoscope augmentation for intra-operative liver resection planning," in *Medical Imaging*. International Society for Optics and Photonics, 2007, pp. 650 915–650 915.
- [55] T. Langø, G. A. Tangen, R. Mårvik, B. Ystgaard, Y. Yavuz, J. H. Kaspersen, O. V. Solberg, and T. A. N. Hernes, "Navigation in laparoscopy - prototype research platform for improved image-guided surgery," *Minimally Invasive Therapy & Allied Technologies*, vol. 17, no. 1, pp. 17–33, 2008.
- [56] S. Billings, A. Kapoor, M. Keil, B. J. Wood, and E. Boctor, "A hybrid surface/image-based approach to facilitate ultrasound/CT registration," in *SPIE Medical Imaging*. International Society for Optics and Photonics, 2011, pp. 79 680V–79 680V.
- [57] V. Martens, A. Beširević, O. Shahin, and M. Kleemann, "LapAssistent - computer assisted laparoscopic liver surgery," in *BMT*, 2010, special session, no peer-review.
- [58] G. P. Penney, J. M. Blackall, M. Hamady, T. Sabharwal, A. Adam, and D. J. Hawkes, "Registration of freehand 3D ultrasound and magnetic resonance liver images," *Medical image analysis*, vol. 8, no. 1, pp. 81–91, 2004.
- [59] W. Wein, A. Khamene, D.-A. Clevert, O. Kutter, and N. Navab, "Simulation and fully automatic multimodal registration of medical ultrasound," in *Medical Image Computing and Computer-Assisted Intervention–MICCAI 2007*. Springer, 2007, pp. 136–143.
- [60] W. Wein, S. Brunke, A. Khamene, M. R. Callstrom, and N. Navab,

- “Automatic CT-ultrasound registration for diagnostic imaging and image-guided intervention,” *Medical image analysis*, vol. 12, no. 5, pp. 577–585, 2008.
- [61] B. Dagon, C. Baur, and V. Bettschart, “Real-time update of 3D deformable models for computer aided liver surgery,” in *Pattern Recognition, 2008. ICPR 2008. 19th International Conference on*. IEEE, 2008, pp. 1–4.
- [62] J. Olesch, B. Beuthien, S. Heldmann, N. Papenberg, and B. Fischer, “Fast intra-operative non-linear registration of 3D-CT to tracked, selected 2D-ultrasound slices,” in *SPIE Medical Imaging*. International Society for Optics and Photonics, 2011, pp. 79 642R–79 642R.
- [63] J. Harms, H. Feussner, M. Baumgartner, A. Schneider, M. Donhauser, and G. Wessels, “Three-dimensional navigated laparoscopic ultrasonography,” *Surg Endosc*, vol. 15, pp. 1459–1462, 2001.
- [64] E. Sjølie, T. Langø, B. Ystgaard, G. A. Tangen, T. A. Nagelhus Hernes, and R. Marvik, “3D ultrasound-based navigation for radiofrequency thermal ablation in the treatment of liver malignancies,” *Surg Endosc*, vol. 17, pp. 933–938, Jun 2003.
- [65] P. Bao, T. K. Sinha, C. C. Chen, J. R. Warmath, R. L. Galloway, and A. J. Herline, “A prototype ultrasound-guided laparoscopic radiofrequency ablation system,” *Surg Endosc*, vol. 21, pp. 74–79, Jan 2007.
- [66] T. K. Chen, A. D. Thurston, M. H. Moghari, R. E. Ellis, and P. Abolmaesumi, “A real-time ultrasound calibration system with automatic accuracy control and incorporation of ultrasound section thickness,” in *Medical Imaging*. International Society for Optics and Photonics, 2008, pp. 69 182A–69 182A.
- [67] N. Pagoulatos, D. R. Haynor, and Y. Kim, “A fast calibration method for 3-D tracking of ultrasound images using a spatial localizer,” *Ultrasound Med Biol*, vol. 27, no. 9, pp. 1219–1229, Sep 2001.

- [68] V. Martens, “Entwurf und Entwicklung eines Assistenzsystems für die laparoskopische Leberchirurgie,” Ph.D. dissertation, Universität zu Lübeck, 2012.
- [69] K. Shoemake, “Animating rotation with quaternion curves,” *ACM SIGGRAPH computer graphics*, vol. 19, no. 3, pp. 245–254, 1985.
- [70] D. G. Gobbi and T. M. Peters, “Interactive intra-operative 3D ultrasound reconstruction and visualization,” in *Medical Image Computing and Computer-Assisted Intervention - MICCAI 2002*. Springer, 2002, pp. 156–163.
- [71] J. A. Noble and D. Boukerroui, “Ultrasound image segmentation: a survey,” *IEEE Trans Med Imaging*, vol. 25, pp. 987–1010, Aug 2006.
- [72] T. S. Yoo, *Insight into images: principles and practice for segmentation, registration, and image analysis*. AK Peters/CRC Press, 2004.
- [73] R. Malladi, J. A. Sethian, and B. C. Vemuri, “Shape modeling with front propagation: A level set approach,” *IEEE Transactions on Pattern Analysis and Machine Intelligence*, vol. 17, pp. 158–175, 1995.
- [74] I. Bronshtein, K. Semendyayev, G. Musiol, H. Muehlig, and H. Mühlig, *Handbook of Mathematics*. Springer, 2004.
- [75] P. A. Yushkevich, J. Piven, H. C. Hazlett, R. G. Smith, S. Ho, J. C. Gee, and G. Gerig, “User-guided 3D active contour segmentation of anatomical structures: significantly improved efficiency and reliability,” *Neuroimage*, vol. 31, no. 3, pp. 1116–1128, 2006.
- [76] G. Lohmann, *Volumetric Image Analysis*. Wiley, 1998.
- [77] V. Caselles, R. Kimmel, and G. Sapiro, “Geodesic Active Contours,” *International Journal of Computer Vision*, vol. 22, pp. 61–79, 1995.

- [78] L. Ibanez, W. Schroeder, L. Ng, and J. Cates, *The ITK Software Guide*, 1st ed., Kitware, Inc. ISBN 1-930934-10-6, 2003.
- [79] Y. Y. Boykov and M.-P. Jolly, “Interactive graph cuts for optimal boundary & region segmentation of objects in ND images,” in *Computer Vision, 2001. ICCV 2001. Proceedings. Eighth IEEE International Conference on*, vol. 1. IEEE, 2001, pp. 105–112.
- [80] L. Ford and D. Fulkerson, “Flows in networks,” *Princeton U. Press, Princeton, NJ*, 1962.
- [81] M. J. Paszek, N. Zahir, K. R. Johnson, J. N. Lakins, G. I. Rozenberg, A. Gefen, C. A. Reinhart-King, S. S. Margulies, M. Dembo, D. Boettiger *et al.*, “Tensional homeostasis and the malignant phenotype,” *Cancer cell*, vol. 8, no. 3, pp. 241–254, 2005.
- [82] D. J. C. MacKay, *Information Theory, Inference and Learning Algorithms*. Cambridge University Press, 2003.
- [83] D. Mattes, D. R. Haynor, H. Vesselle, T. K. Lewellyn, and W. Eubank, “Nonrigid multimodality image registration,” in *Medical Imaging 2001*. International Society for Optics and Photonics, 2001, pp. 1609–1620.
- [84] M. D. Scott DJ, W. N. Young, L. M. Watumull, G. Lindberg, J. B. Fleming, R. V. Rege, R. J. Brown, and D. B. Jones, “Development of an in vivo tumor-mimic model for learning radiofrequency ablation,” *J. Gastrointest. Surg.*, vol. 4, no. 6, pp. 620–625, 2000.
- [85] W. J. Schroeder, K. Martin, and W. Lorensen, *The Visualization Toolkit: An Object-Oriented Approach to 3D Graphics, Third Edition*. Kitware, Inc. (formerly Prentice-Hall), 2003.
- [86] G. Bradski, “The OpenCV Library,” *Dr. Dobb’s Journal of Software Tools*, 2000.

- [87] T. Rohlfing, C. R. Maurer Jr, W. G. Odell, and J. Zhong, “Modeling liver motion and deformation during the respiratory cycle using intensity-based nonrigid registration of gated MR images,” *Medical Physics*, vol. 31, p. 427, 2004.
- [88] B. Olbrich, J. Traub, S. Wiesner, A. Wichert, H. Feußner, and N. Navab, “Respiratory motion analysis: Towards gated augmentation of the liver,” in *International Congress Series*, vol. 1281. Elsevier, 2005, pp. 248–253.
- [89] L. Maier-Hein, F. Pianka, A. Seitel, S. Müller, A. Tekbas, M. Seitel, I. Wolf, B. Schmied, and H.-P. Meinzer, “Precision targeting of liver lesions with a needle-based soft tissue navigation system,” in *Medical Image Computing and Computer-Assisted Intervention—MICCAI 2007*. Springer, 2007, pp. 42–49.
- [90] H. Zhang, F. Banovac, R. Lin, N. Glossop, B. J. Wood, D. Lindisch, E. Levy, and K. Cleary, “Electromagnetic tracking for abdominal interventions in computer aided surgery,” *Computer Aided Surgery*, vol. 11, no. 3, pp. 127–136, 2006.
- [91] M. F. Khan, S. Dogan, A. Maataoui, S. Wesarg, J. Gurung, H. Ackermann, M. Schiemann, G. Wimmer-Greinecker, and T. J. Vogl, “Navigation-based needle puncture of a cadaver using a hybrid tracking navigational system,” *Investigative radiology*, vol. 41, no. 10, pp. 713–720, 2006.
- [92] G. Fichtinger, A. Deguet, G. Fischer, I. Iordachita, E. Balogh, K. Masamune, R. H. Taylor, L. M. Fayad, M. De Oliveira, and S. J. Zinreich, “Image overlay for CT-guided needle insertions,” *Computer Aided Surgery*, vol. 10, no. 4, pp. 241–255, 2005.
- [93] D. M. Cash, M. I. Miga, S. C. Glasgow, B. M. Dawant, L. W. Clements, Z. Cao, R. L. Galloway, and W. C. Chapman, “Concepts and preliminary data toward the realization of image-guided liver surgery,” *Journal of Gastrointestinal Surgery*, vol. 11, no. 7, pp. 844–859, 2007.

- [94] A. Schenk, G. Prause, and H.-O. Peitgen, “Efficient semiautomatic segmentation of 3D objects in medical images,” in *Medical Image Computing and Computer-Assisted Intervention–MICCAI 2000*. Springer, 2000, pp. 186–195.
- [95] “Standards for radiofrequency ablation (RFA).” London: The Royal College of Radiologists., December 2009, ISBN: 978-1-905034-40-6 Ref No. BFCR(09)12.
- [96] T. Varghese, J. Zagzebski, and F. L. Jr., “Elastographic imaging of thermal lesions in the liver in vivo following radiofrequency ablation: preliminary results,” *Ultrasound in Medicine & Biology*, vol. 28, pp. 1467 – 1473, 2002.
- [97] J. Kim, H. Yim, K. Lee, S. Kim, E. Jung, Y. Jung, J. Kim, Y. Seo, J. Yeon, H. Lee, S. Um, K. Byun, and H. Ryu, “Recurrence rates and factors for recurrence after radiofrequency ablation combined with transarterial chemoembolization for hepatocellular carcinoma: a retrospective cohort study,” *Hepatology International*, vol. 6, pp. 505–510, 2012.
- [98] Y. K. Cho, H. Rhim, and S. Noh, “Radiofrequency ablation versus surgical resection as primary treatment of hepatocellular carcinoma meeting the Milan criteria: A systematic review,” *Journal of Gastroenterology and Hepatology*, vol. 26, no. 9, pp. 1354–1360, 2011.
- [99] L. Tiong and G. J. Maddern, “Systematic review and meta-analysis of survival and disease recurrence after radiofrequency ablation for hepatocellular carcinoma,” *British Journal of Surgery*, vol. 98, no. 9, pp. 1210–1224, 2011.
- [100] S. Clasen, A. Boss, D. Schmidt, J. Fritz, C. Schraml, C. Claussen, and P. Pereira, “Magnetic resonance imaging for hepatic radiofrequency ablation,” *European Journal of Radiology*, vol. 59, no. 2, pp. 140 – 148, 2006.
- [101] S.-Y. Chiou, J.-B. Liu, and L. Needleman, “Current Status of Sonographically Guided Radiofrequency Ablation Techniques,” *Journal of Ultrasound in Medicine*, vol. 26, no. 4, pp. 487–499, 2007.

## BIBLIOGRAPHY

---

- [102] P. Foroughi, J. Burgner, M. A. Choti, R. J. Webster III, G. D. Hager, and E. M. Boctor, “Towards Intra-operative Monitoring of Ablation Using Tracked 3D Ultrasound Elastography and Internal Palpation,” in *Proc. of SPIE Vol.*, vol. 8320, 2012, pp. 83 200T–1.
- [103] T. Wu, J. P. Felmlee, J. F. Greenleaf, S. J. Riederer, and R. L. Ehman, “Assessment of thermal tissue ablation with MR elastography,” *Magnetic Resonance in Medicine*, vol. 45, no. 1, pp. 80–87, 2001.
- [104] J. Ophir, I. Cespedes, H. Ponnekanti, Y. Yazdi, and X. Li, “Elastography: a quantitative method for imaging the elasticity of biological tissues,” *Ultrasonic Imaging*, vol. 13, no. 2, pp. 111–134, Apr 1991.
- [105] J. Ophir, S. Alam, B. Garra, F. Kallel, E. Konofagou, T. Krouskop, C. Merritt, R. Righetti, R. Souchon, S. Srinivasan, and T. Varghese, “Elastography: Imaging the elastic properties of soft tissues with ultrasound,” *Journal of Medical Ultrasonics*, vol. 29, no. 4, pp. 155–171, 2002.
- [106] I. Winkler and D. Adam, “Monitoring Radio-Frequency Thermal Ablation with Ultrasound by Low Frequency Acoustic Emissions In Vitro and In Vivo Study,” *Ultrasound in Medicine & Biology*, vol. 37, no. 5, pp. 755 – 767, 2011.
- [107] E. M. Boctor, G. Fichtinger, A. Yeung, M. Awad, R. H. Taylor, and M. A. Choti, “Robotic strain imaging for monitoring thermal ablation of liver,” in *Medical Image Computing and Computer-Assisted Intervention–MICCAI 2004*. Springer, 2004, pp. 81–88.
- [108] P. Foroughi, H. Rivaz, I. N. Fleming, G. D. Hager, and E. M. Boctor, “Tracked ultrasound elastography (TrUE),” in *Medical Image Computing and Computer-Assisted Intervention–MICCAI 2010*. Springer, 2010, pp. 9–16.
- [109] S. N. Goldberg, C. J. Grassi, J. F. Cardella, J. W. Charboneau, G. D. D. III, D. E. Dupuy, D. A. Gervais, A. R. Gillams, R. A. Kane, F. T. L. Jr, T. Livraghi, J. McGahan, D. A. Phillips, H. Rhim, S. G. Silverman,

- L. Solbiati, T. J. Vogl, B. J. Wood, S. Vedantham, and D. Sacks, "Image-guided Tumor Ablation: Standardization of Terminology and Reporting Criteria," *Journal of Vascular and Interventional Radiology*, vol. 20, no. 7, Supplement, pp. S377 – S390, 2009.
- [110] J. Lewin, C. Connell, J. Duerk, Y.-C. Chung, M. Clampitt, J. Spisak, G. Gazelle, and J. Haaga, "Interactive MRI-Guided Radiofrequency Interstitial Thermal Ablation of Abdominal Tumors: Clinical Trial for Evaluation of Safety and Feasibility," *The Journal of Urology*, vol. 161, no. 2, p. 733, 1999.
- [111] E. M. Merkle, J. R. Haaga, J. L. Duerk, G. H. Jacobs, H.-J. Brambs, and J. S. Lewin, "MR Imaging-guided Radio-frequency Thermal Ablation in the Pancreas in a Porcine Model with a Modified Clinical C-Arm System," *Radiology*, vol. 213, no. 2, pp. 461–467, 1999.
- [112] T. L. Boaz, J. S. Lewin, Y.-C. Chung, J. L. Duerk, M. E. Clampitt, and J. R. Haaga, "MR monitoring of MR-guided radiofrequency thermal ablation of normal liver in an animal model," *Journal of Magnetic Resonance Imaging*, vol. 8, no. 1, pp. 64–69, 1998.
- [113] A. Henderson, *The ParaView Guide: A Parallel Visualization Application*. Kitware, 2004.
- [114] A. U. Hines-Peralta, N. Pirani, P. Clegg, N. Cronin, T. P. Ryan, Z. Liu, and S. N. Goldberg, "Microwave ablation: results with a 2.45-GHz applicator in ex vivo bovine and in vivo porcine liver," *Radiology*, vol. 239, no. 1, pp. 94–102, Apr 2006.
- [115] M. S. Breen, T. L. Lancaster, R. S. Lazebnik, S. G. Nour, J. S. Lewin, and D. L. Wilson, "Three-dimensional method for comparing in vivo interventional MR images of thermally ablated tissue with tissue response," *J Magn Reson Imaging*, vol. 18, no. 1, pp. 90–102, Jul 2003.

## BIBLIOGRAPHY

---

- [116] S. S. Raman, D. S. Lu, D. J. Vodopich, J. Sayre, and C. Lassman, "Creation of Radiofrequency Lesions in a Porcine Model Correlation with Sonography, CT, and Histopathology," *American Journal of Roentgenology*, vol. 175, no. 5, pp. 1253–1258, 2000.